Faculteit Wetenschappen
Departement Fysica

Proefschrift voorgelegd tot het behalen van de graad van doctor in de Wetenschappen aan de Universiteit Antwerpen te verdedigen

door

Andrey Kapra

Controlling the flux dynamics in superconductors by nanostructured magnetic arrays

---

Manipulatie van de flux dynamica in supergeleiders door nanogestructureerde magnetische roosters

Promoter: Dr. V. R. Misko
Co-promoter: Prof. Dr. F. M. Peeters

Antwerpen

2013

Jury members

Prof. Dr. S. Bals (Voorzitter), UA

Prof. Dr. D. Lamoen (Lid van doctoraatscommissie), UA

Dr. V. R. Misko (Promotor, Lid van doctoraatscommissie), UA

Prof. Dr. F. M. Peeters (Co-promotor), UA

Prof. Dr. A. V. Silhanek, Université de Liège

Prof. Dr. J. Van de Vondel, KU Leuven

Contact Information

Andrey Kapra
Departement Fysica
Universiteit Antwerpen (CGB)
Groenenborgerlaan 171
B-2020 Antwerpen
Belgium
Andrey.Kapra@ua.ac.be

Acknowledgements

Foremost, I would like to express my sincere thanks to: my promoter and adviser-sensei V. R. Misko for his truly enormous patience, guidance and help during the complete study period; co-promoter F. M. Peeters for letting me to carry my research in the CMT group and the main collaborator D. Y. Vodolazov, whose programming skills and sense of humor still makes me admire, for the fruitful discussions given during his short and scarce research stays at UA.

Numerous colleagues (former and present) at CMT and EMAT were a source of information, ongoing support, and encouragement during these years. Individual thanks for the colleague of mine Chen Yajang, who introduced GNU Linux to me and shared his wisdom of Bash scripting.

Many others contributed greatly, helping me to reach this defense day. Among them there are people from secretary office (i.e., Hilde and Gert), IT-team (Kwinten, Coen, Nikolas) and Photolab (André and Freddy). Special appreciation goes to Jaques Tempère for his excellently given lectures on "Superconductivity and Superfluidity".

Thanks for all my friends (especially D. A. Kirilenko and Y. M. Bidasyuk), whom I have had honor to meet and to talk in Antwerpen. At last but not least, I would like to thank my family for their permanent encouragement and timely inspiration during my scientific research.

Andrey
May, 2013

Table of Contents

Chapter 1

Introduction

There are several issues of superconductivity (beside obviously cumbersome cryogenic refrigerators) which prevents its rapid integration into daily technology and becoming broadly used. Among many reasons leading to overheating of the superconducting circuits and energy dissipation, the flux-motion stands aside. One of the keys to solve this problem is stabilizing vortices or trapping them completely through the pinning. Magnetic dots, acting as efficient pinning centers for external flux lines, lead to an increase of critical current, j_c, and critical magnetic field, H_{c2}. Although vortex-pinning approach improved stability of superconducting devices and extended range of their applicability, the phenomena standing behind the flux pinning are not investigated in all details. The possibility of manipulating vortex matter by using various artificial pinning arrays is of significant importance for possible applications in fluxonics nano- and micro-devices.

In all nano-engineered superconducting devices, the performance is strongly dependent on the behavior of the magnetic flux inside the devices, especially on the mesoscopic scale. Mesoscopic superconducting samples have sizes comparable to one of the two characteristic length scales: the coherence length ξ or the magnetic penetration depth λ. While in bulk superconductors penetrating vortices form a triangular Abrikosov lattice due to the vortex-vortex repulsion and the critical parameters and the properties are determined by the material, in mesoscopic superconductors the situation is more complicated. In mesoscopic superconductors there is a competition between the triangular configuration of the vortex lattice and the boundary which tries to impose its geometry on the vortex lattice.

The vortex states in a square pinning array have attracted considerable attention mainly because it can produce a large increase in the critical current at certain values of the magnetic field, which corresponds to the matching between the number of vortices and the number of pinning sites in the system. Motivated by significant experimental achievements and recent theoretical developments, in this thesis we concentrate on the key question: *How superconducting properties (i.e., critical current j_c) are affected by the geometrical flux confinement in mesoscopic films and bridges?* In this thesis we study the dynamics of vortices in two-dimensional (2D) mesoscopic superconducting systems in presence of arrays of magnetic nanostructures. For this purpose we employ numerical solving of the time-dependent Ginzburg-Landau equations. It allows us to study the vortex-antivortex dynamics

including processes of vortex-antivortex annihilation in a great detail. We focus our research on hybrid structures consisting of a finite size superconductor with magnetic bar on top, which generate vortex-antivortex pairs in the presence of an external current, superconducting films with periodic arrays of magnetic bars, and narrow patterned superconducting channels surrounded by a bank superconductor with lower-T_c superconductor.

In this thesis we investigate theoretically **how the critical current j_c of nano-engineered mesoscopic superconducting film can be improved and how one can control the dynamics of the magnetic flux, e.g., the transition from flux-pinned to flux-flow regime, using arrays of magnetic nanostructures**. In particularly we investigate:

- Vortex transport phenomena in superconductors with deposited ferromagnetic structures on top, and the influence of the sample geometry on the critical parameters and on the vortex configurations. Changing geometry of the magnetic bars and magnetization of the bars will affect the critical current j_c of the superconducting film. Such nanostructured ferromagnets strongly alter the vortex structure in its neighborhood. The influence of geometry, position and magnetization of the ferromagnet (single bar or regular lattice of the bars) on the critical parameters of the superconductor is investigated.

- Effect of flux confinement in narrow superconducting channels with zigzag-shaped banks: the flux motion is confined in the transverse (perpendicular) direction of a diamond-cell-shape channel. The matching effect for the magnetic flux is found in the system relevantless of boundary condition. We discuss the dynamics of vortices in the samples and vortex pattern formation in the channel. We show how the inclusion of higher-T_c superconductor into the sample can lead to enhanced properties of the system. By adding an external driving force, we study the vortex dynamics. The different dynamic regimes are discussed. They allowed an effective control of magnetic flux in superconductors.

The present thesis is organized as follows:

Chapter 1 introduces a brief historical survey of superconductivity and a short introduction with outlines of the phenomenological London, and Ginzburg-Landau theories and the microscopic theory. The London and Ginzburg-Landau equations are derived in frameworks of their phenomenological theories. We give a brief introduction to the magnetic properties of type I and type II superconductors. Two last paragraphs are devoted to the experimental observation of vortices, control over their motion, and industrial/commercial applications of superconductors.

Chapter 2 shows the numerical approach for solving the time-dependent Ginzburg-Landau equations, including introduction of dimensionless units, and link-variables. Separate paragraphs are devoted to the Neuman and periodic boundary conditions, gauge invariance of the equations. The detailed mathematics describes Fourier transformations and Cyclic reduction methods. This chapter

is primarily intended for PhD students in physics or mathematics, who are involved in scientific numerical simulations. The author tried to show explicitly the mathematical formalism behind the code programming.

In **Chapter 3** of this thesis, we describe effects of modification of the transport properties of a superconductor by depositing ferromagnetic structures (magnetic bars) on top. The vortex-antivortex dynamics is analyzed for different arrangements and magnetic moments of the dipoles, as a function of angle α between the direction of the magnetic dipole and that of the Lorentz force produced by the applied current. The interplay of the attractive interaction between a vortex-antivortex pair and the Lorentz force leads either to the separation of (anti)vortices and their motion in opposite directions or to their annihilation. We found a critical angle α_c, below which vortices and antivortices are repelled, while for larger angles they annihilate. In case of a single (few) magnetic dipole(s), this magnetic-dipole-induced vortex-antivortex guidance is influenced by the self-interaction of the vortex-antivortex pairs with their images in a finite-size sample, while for a periodic array of dipoles the guidance is determined by the interaction of a vortex-antivortex pair with other dipoles and vortex-antivortex pairs created by them. This effect is tunable through the external current and the magnetization and size of the magnetic dipoles.

In **Chapter 4**, we investigate an array of magnetic bars deposited on top of a superconducting film. Different pinning regimes, depending on the direction of the in-plane magnetization of the bars, are shown. Changing the sign of their magnetization results in changes in the induced magnetic pinning potentials. By numerically solving the time-dependent Ginzburg-Landau equations in a superconducting film with periodic arrays of zigzag-arranged magnetic bars, we revealed various flux dynamics regimes. In particular, we demonstrate flux pinning and flux flow, depending on the direction of the magnetization of the magnetic bars. Remarkably, the revealed different flux-motion regimes are associated with different mechanisms of vortex-antivortex dynamics. For example, we found that for "antiparallel" configuration of magnetic bars this dynamics involves a repeating vortex-antivortex generation and annihilation. We show that the depinning transition and the onset of flux-flow can be manipulated by the magnetization of the bars and the geometry of the array. This provides an effective control of the depinning critical current j_c that can be useful for possible fluxonics applications.

In **Chapter 5**, we investigate the vortex transport phenomena in a diamond-cell channel. By numerically solving the time-dependent Ginzburg-Landau equations in a type-II superconducting film with a channel formed by overlapping rhombuses (diamond-like channel) made of another type-II superconductor characterized by a higher critical temperature, T_{c2}, than the film, we investigate the influence of the channel properties (i.e., the width of the neck (gap) connecting the cells, the cell geometry, the ratio between the coherence length of the main film and the channel) on the vortex motion. The matching effect for the magnetic flux was observed in the diamond-like channel. We found that, in finite samples peaks in the critical current, $j_c(H_{ex})$, correspond to the entry of a vortex in the channel, while in an infinite sample the revealed peak is due to commensurability between the number of cells in the channel and the number of the flux quanta.

1.1 Historical overview

In 1911, at Leiden University in the Netherlands, Professor Heike Kamerlingh Onnes was cooling down mercury with the newly discovered cryogenic liquid helium and measuring its resistance. When the temperature reached $4.2K$ $[-269°C]$ the electrical resistance suddenly dropped to zero 1.1. The sudden drop corresponded to a new resistant free state which has never been found before. Although scientific community considered the reported phenomena very sceptically, research interest in this direction was initiated. After a lot of checking, this result was found to be correct. The effect was called later as *superconductivity*. It was dawn of the new found quantum phenomena [1].

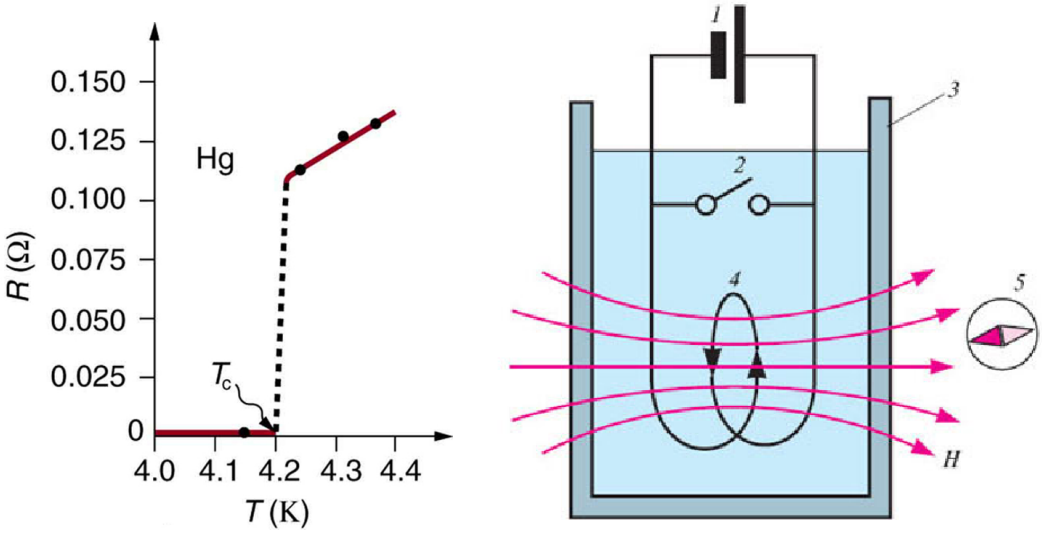

Figure 1.1: (a) Drop of the electrical resistance of mercury at $T_c = 4.2K$ shows transition from normal to superconducting state. (b) Principial scheme of Onnes experiment: 1 - current source; 2 - switch; 3 - liquid helium; 4 - superconducting ring inducing magnetic field; 5 - test-magnet (probe-magnet).

Soon, other materials were found to be superconductors as well (Pb, Nb, Sn), however there was an open question still: was a superconductor an ideal conductor or not? In 1933 W. Meissner and R. Ochsenfeld found that superconductor expels an external magnetic field from its inside, when cooled through the critical temperature [2]. It meant that superconductor is not just a perfect conductor of electricity, but a diamagnetic as well:

$$\cancel{SC : \rho = 0} \qquad\qquad SC : \rho = 0 \quad and \quad \mathbf{B} = 0.$$

Although a superconductor expels weak magnetic field, superconducting state can be destroyed when the external magnetic field exceeds a certain value H_{c2}, which is called the critical magnetic field. Meissner effect is described as perfect diamagnetism that appears inside superconductor material. This effect appears because there is a surface current induced in superconductor that generates additional magnetic field that cancels the external magnetic field inside the superconductor.

When the current is set up it persists forever, due to absence of resistivity in superconductors. The non-dissipative current is called *supercurrent*.

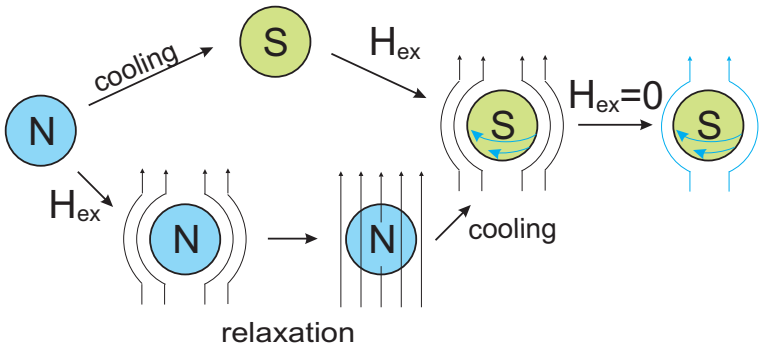

Figure 1.2: Superconducting state achieved with two different ways. Zero-Field-Cooled (ZFC) is at the top. ZFC regime corresponds to cooling of a specimen firstly and then, turn on the magnetic field. Field-Cooled (FC) is at the bottom. It corresponds to cooling of the specimen when magnetic field was on. Blue arrows show the induced supercurrent and magnetic field of the current.

Only after more than twenty years after the report of the superconductivity, the first satisfying theory with mathematical background was developed by brothers London in 1935 [3]. Using Maxwell equations and hypothesis of the supercurrent they came up with zero-resistivity and expelling the external magnetic field. It introduced the concept of magnetic field penetration depth, λ. Brief derivation of the equations and conclusions are given in paragraph 1.1.1. London theory describes very well the behavior of some (extreme type-II) superconductors.

Much later (in 1950), F. London predicted fluxoid quantization [4]. The magnetic flux through a superconductor can obtain only integer multiples of a quantity called the *flux quantum*. It took a whole decade before the experiments of Doll and Näbauer [5] confirmed it. Studying those showed existence of *vortices*, whirls of superconducting electrons. They are the carriers of the flux quanta.

Year 1950 was eminent with introducing a new theory of superconductivity, which was proposed by L. Landau and V. Ginzburg (see paragraph 1.1.2 and Ref. [6]). They noticed that the superconducting state is a new thermodynamical state and the transition (FC and ZFC) from the normal state to the superconducting state can be treated as a phase transition. Using the early developed mathematical theory of phase transitions, they successfully applied it for superconductors.

It was a phenomenological theory which did not shed the light on the mechanism of the superconductivity, but was just an attempt to give a theoretical explanation of the observed phenomena. This description did not explain where the condensate comes from, but it described the way it behaved when the temperature of the material was changed. In this "phenomenological" approach, Landau assumed that the condensate did exist and that he could describe it with a quantum wave function, characterized by an amplitude and a phase. Landau proposed that a superconductor is a more "orderly" environment than a non superconduct-

ing environment, and that the wave function could describe this new order. Since this model does not explain why the condensate exists but only assumes it does, it can be used to explain the properties of superconductors even though the origin of this type of superconductivity is not well known.

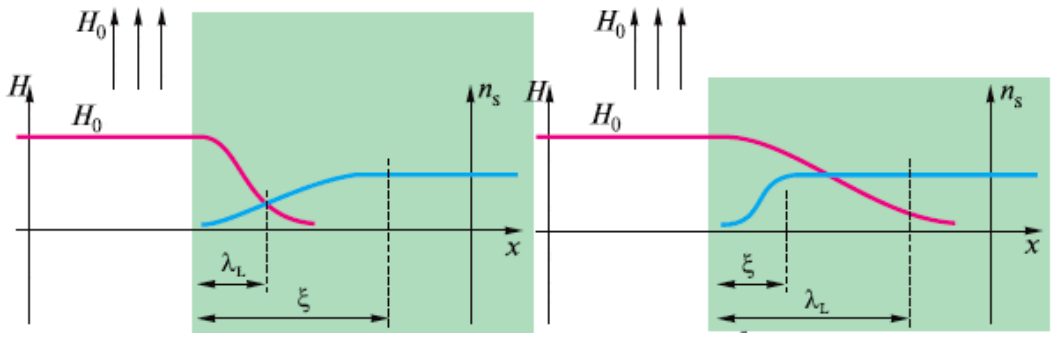

Figure 1.3: Two characteristic lengths, the coherence length, ξ, and magnetic field penetration depth, λ, in type-I and type-II superconductors.

First breakthrough in understanding of the mechanism responsible for superconductivity was made in 1957 by J. Bardeen, L. Cooper. and J. Schrieffer [7]. They showed that even incredibly small attractive interaction is capable to bring system into a state with unified wave function. The long-awaited microscopic theory finally shed the light on the origin of superconductivity. The BCS theory works fine for phonon-mediated superconductors (*conventional superconductors*), such as pure metals. It does not explain the phenomena in iron-based superconductors.

The isotope effect (1950) is described by two independent groups of scientists as a proportionality of transition temperature T_c to the isotope nucleus mass and this dependence gave clue that superconductivity was related to lattice vibration. The choice of isotope ordinarily has little effect on the electrical properties of a material, but does affect the frequency of lattice vibrations, this effect suggested that superconductivity is related to vibrations of the lattice. This is incorporated into the BCS theory, where lattice vibrations yield the binding energy of electrons in a Cooper pair.

BCS theory stated that superconductivity appears from pairing of electrons with opposite spin and wave number under influence of lattice vibration or phonons. Electron moving through conductor attracts positive charge nucleus in lattice, resulting lattice displacement which also attracts another electron with different spin and wave number so that these two electrons are correlated. In superconductor a lot of electron pair appear, they are strongly overlapped and formed Bose-Einstein condensate and lose electrical resistance.

Shortly after (1958), L. Gor'kov showed that the BCS theory can be derived in terms of Green functions [8]. His work linked phenomenological parameters (λ and ξ, see Chapter 1.3) with parameters from microscopical theory. His elegant mathematical approach is still in use.

Meanwhile (1957), A. Abrikosov explained abnormal behavior of some superconductors in magnetic field [9], when studied GL equation in the limit $\lambda > \xi$. It

led to the split of superconductor family in two types: first one, which shows a complete Meissner effect and another (type-II superconductors, see Chapter 1.2) — which does not. Abrikosov predicted the existence of vortex array in the mixed state of type II superconductors. Although his calculations were corrupted and he predicted a square lattice instead of a triangular one, the last one carries his name, *Abrikosov lattice*.

In 1962 B. Josephson published his work, where predicted very interesting phenomena [10]. He analyzed the transfer of superconducting carriers through a tunnel junction. He concluded the following. Firstly, there is a current of superconducting electrons through a thin insulating layer. Second, this contact can generate a high-frequency electromagnetic waves when a certain voltage is applied: 483 597.9 GHz corresponds to 1 V. These phenomena relate to weak superconductivity. His theoretical work provided appearance of Superconducting Quantum Interference device (SQUID), which is used in high precision measurement of extremely weak magnetic fields.

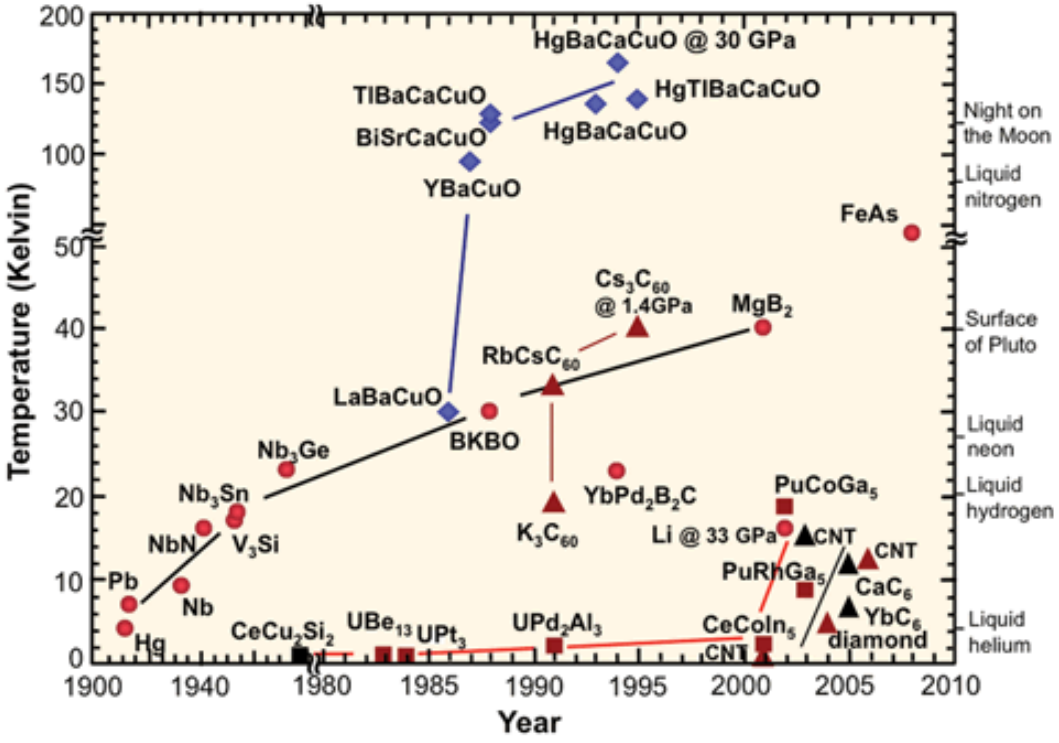

Figure 1.4: Progress in T_c history upon the time.

Year 1986 is remarkable through a significant achievement in High Temperature Superconductivity (HTS or high-T_c). K. Alex Muller and J. Georg Bednorz of IBM Zurich reported about ceramic material turning to a superconductor at liquid Nitrogen temperature [11]. It was found later that properties of the ceramic belong to a wide class of materials, *cuprates*. These materials become superconducting at the highest temperatures: $-135°C$ or 138 K for $HgBa_2Ca_2Cu_3O_{8+x}$ - above the temperature of liquid nitrogen. Their composition and structure is quite simple: they are composed of piled up atom layers. In all cuprates, we find copper

and oxygen layers with a square structure. The number of electrons in these layers can be modified by doping (i.e., oxidizing) the material or modifying its chemical composition. At a low temperature, the same compound is both insulating and magnetically orderly, but when the number of electrons is changed by a few percents, it becomes the best superconductor! Although the chemical structure of cuprates is well studied, their high-T_c cannot be described within framework of the BCS theory.

Since then, many chemical compounds were tested for superconducting properties. Recently found, nonconventional superconductors refer to a wide variety of materials (i.e., dopped fullerenes, cuprates, pnictides, heavy fermion compounds, ferrites, graphine [12]). These alternative superconductors are synthesized artificially in laboratory. They are interesting for origin of their superconductivity, which does not obey the standard BCS model.

Fullerene molecules C_{60} can form a solid with a cubic structure, where the fullerenes occupy each corner and each face center of the cube. Research activities on fullerene alkaline compounds have started their revival very recently: transition from an insulator to a metal (Mott transition) reminds of what happens in cuprates. The most surprising part is that the space between C_{60} is so big that the electrons are pinned to the balls and prevent them from relocating. At atmospheric pressure, the Cs_3C_{60} compound is hence both insulating and magnetic. However, under a stronger pressure, the compound becomes a superconducting metal with a maximum T_c of 35 K ($-238°C$).

A genuine interest causes iron-based superconductors ($BaFe_2As_2$, $LiFeAs$, $BaCo_2As_2$, $CeFeAsO$, etc.). For the time being it was believed that ferromagnetism and superconductivity cannot coexist, however, recent experiments revealed a class of materials where both these phenomena exist peacefully. Moreover, superconductivity cannot survive in these materials without Ferromagnetism [13]. As far as applications are concerned, pnictides are promising: they have good mechanical properties and their superconductivity can resist strong magnetic fields and electric currents.

The interest for a well-known superconducting MgB_2 ($T_c = 39K$) was revived recently. First report of superconducting properties of MgB_2 appeared in 2001 [14]. It was found later that electron-electron interaction in the material is phonon-mediated and it contains two energy bands. They provide the mixed properties of type-I and type-II superconductors.

For the passed century superconducting materials have widely grown in variety and number. To represent current achievements in the discovered superconductors we included Fig. 1.4. Superconductivity has started another century since its discovery, but still keeps some mystery.

1.1.1 London theory

First successful attempt to give a mathematical background of the phenomena was given by brothers Fritz and Heinz London in 1935 [3]. They assumed that there are two sets of free electrons in the superconductor: the normal one and the superconducting one with densities n_n and n_s correspondingly. The superconduct-

ing component reaches its maximum at $T = 0K$ and has a minimum at $T = T_c$. The component n_n behaves opposite such way that the equality $n_{tot} = n_n + n_s$ is satisfied, where n_{tot} denotes the total density of the electrons in the superconductor. They also considered that the electric and magnetic fields are weak, and the supercurrent is homogeneous.

According to the Newton's $2nd$ law, we may write for the superconducting electrons:

$$n_s m \frac{d\overrightarrow{v_s}}{dt} = n_s e \overrightarrow{E}, \tag{1.1}$$

where m, e — the mass and the charge the "superelectron" correspondingly, $\overrightarrow{v_s}$ — the velocity of the supercurrent. Taking into account the equation for the supercurrent density $\overrightarrow{j_s} = n_s e \overrightarrow{v_s}$, they obtained:

$$\overrightarrow{E} = \frac{d}{dt}\left(\frac{m}{n_s e^2}\overrightarrow{j_s}\right). \tag{1.2}$$

This is the first London equation. It denotes the perfect conductivity: when $\frac{d\overrightarrow{j_s}}{dt} = 0$ the electric field inside the superconductor is absent. Using the Maxwell equation ($rot\overrightarrow{E} = -\frac{1}{c}\frac{\partial \overrightarrow{B}}{\partial t}$), one can obtain

$$rot\overrightarrow{j_s} + \frac{n_s e^2}{mc}\overrightarrow{B} = 0. \tag{1.3}$$

Applying curl-operator to the both sides and using another Maxwell equation ($rot\overrightarrow{H} = \frac{4\pi}{c}\mu\overrightarrow{j_s}$), we obtain:

$$\nabla^2\overrightarrow{B} - \frac{1}{\lambda^2}\overrightarrow{B} = 0, \tag{1.4}$$

where coefficient $\lambda = \sqrt{\frac{\mu mc^2}{4\pi n_s e^2}}$ is the material-dependent characteristic and is called *London penetration depth*. (Note that in superconductivity it is common to use H (for instance, H_c for the critical field) rather than B — see: C. Kittel, *Introduction to Solid State Physics*. In the following chapters, we will often use H to denote magnetic field in a superconductor.)

Considering a semi-planar superconductor in external homogeneous magnetic field B_0 applied parallel to its surface with boundary condition $B(0) = B_0$ at the surface of the superconductor, the exact solution of the equation is $B = B_0 exp(-x/\lambda)$. This solution gives the physical meaning of λ, which is the characteristic length over which the external magnetic field decays, penetrating into the bulk superconductor.

Despite London equations do not describe the spatial distribution of the density of the supercurrent, they give such valuable parameter as the magnetic field penetration depth λ and give a mathematical background for the experimentally observed Meissner effect.

1.1.2 Ginzburg-Landau theory

The Ginzburg-Landau (GL) theory contains two equations which are obtained by minimizing the free energy expanded in terms of the order parameter with respect to a spatially varying complex order parameter Ψ and the vector potential $\overrightarrow{A}$ [15, 16]. $\Psi(\overrightarrow{r})$ is a complex order parameter which is nonzero at $T < T_c$ and vanishes at $T \geqslant T_c$ through a second order phase transition. Another name of the order parameter is a wavefunction of superconducting electrons and is normalized as follows: $|\Psi(\overrightarrow{r})|^2 = \frac{n_s}{2}$.

The superconducting state is more ordered than the normal state, and in the presence of a magnetic field all the transitions from the superconducting state to the normal state are first-order phase transitions, while without a magnetic field the transition at the critical temperature is a second-order phase transition [15].

In absence of magnetic field *order parameter* Ψ obtains homogeneous distribution. Gibbs free energy density of a superconductor without external magnetic field is given by

$$G_s = G_n + \alpha|\Psi|^2 + \frac{\beta}{2}|\Psi|^4, \tag{1.5}$$

where $|\Psi|^2$ is the density of Cooper pairs, G_s is the free energy density of the superconductor in the magnetic field. G_n is the free energy density of the normal state, α and β are phenomenological expansion coefficients depending on the superconducting material. Minimization of the free energy with respect to $|\Psi|^2$, leads to $|\Psi_0|^2 = -\alpha/\beta$. The temperature dependence of α is $\alpha \sim (T - T_c)$, while β is positive and temperature independent.

Near T_c Ψ is small and varies slowly in space. Then Gibbs free energy density in magnetic field can be expressed in power of Ψ as

$$G_s = G_n + \alpha|\Psi|^2 + \frac{\beta}{2}|\Psi|^4 + \frac{1}{2m_s}\left|\left(\frac{\hbar}{i}\nabla - \frac{e_s}{c}\overrightarrow{A}\right)\Psi\right|^2 - \frac{(\overrightarrow{B} - \mu\overrightarrow{H_0})^2}{4\pi\mu}. \tag{1.6}$$

Two last terms in the equation represent the kinetic energy of Cooper pairs and the magnetic energy of the magnetic field generated by supercurrents (the difference between the applied magnetic field and the local one). $m_s = 2m_e$ denotes the mass of the Cooper pair, which is two times the electron mass and its electrical charge $e_s = 2e^-$.

The total energy of the superconducting system can be obtained from the volume integration of Eq. 1.6, and the equilibrium state is reached when the variations of this total energy with respect to Ψ^* and $\overrightarrow{A}$ become zero. The former $\delta_{\Psi^*}G_s$ can be written as

$$\int\left[\alpha\Psi\delta\Psi^* + \beta|\Psi|^2\Psi\delta\Psi^* + \frac{1}{2m_s}\left(\frac{\hbar}{i}\nabla - \frac{e_s}{c}\overrightarrow{A}\right)\Psi\left(\frac{\hbar}{i}\nabla - \frac{e_s}{c}\overrightarrow{A}\right)\delta\Psi^*\right]dV_s = 0, \tag{1.7}$$

where V_s is volume of the superconductor. The variation of Eq. 1.6 $\delta_{\overrightarrow{A}} G_s$ with respect to the vector potential $\overrightarrow{A}$ is

$$\frac{1}{2m_s}\int\left[(-\frac{e_s}{c}\Psi^*\delta\overrightarrow{A})\left(\frac{\hbar}{i}\nabla\Psi-\frac{e_s}{c}\overrightarrow{A}\Psi\right)+\left(-\frac{\hbar}{i}\nabla\Psi^*-\frac{e_s}{c}\overrightarrow{A}\Psi^*\right)(-\frac{e_s}{c}\Psi\delta\overrightarrow{A})\right]dV + \frac{1}{4\pi\mu}\int(rot\overrightarrow{A}-\mu\overrightarrow{H_0})\cdot rot\delta\overrightarrow{A}dV=0. \quad (1.8)$$

In total, from Eqs. 1.7 and 1.8 we obtain

$$\frac{1}{2m_s}\left(\frac{\hbar}{i}\nabla-\frac{e_s}{c}\overrightarrow{A}\right)^2\Psi+|a|\Psi+b|\Psi|^2\Psi=0; \qquad \left(\frac{\hbar}{i}\nabla-\frac{e_s}{c}\overrightarrow{A}\right)\Psi|_n=0, \quad (1.9)$$

and

$$\overrightarrow{j_s}=\frac{e_s\hbar}{2im_s}(\Psi^*\nabla\Psi-\Psi\nabla\Psi^*)-\frac{e_s^2}{cm_s}|\Psi|^2\overrightarrow{A}. \quad (1.10)$$

The obtained boundary conditions are suitable for a superconductor in a dielectric medium and mean that no superconducting current passes through the superconductor-dielectric interface. In the case of a superconductor-metal interface, the boundary condition must be generalized to

$$\left(\frac{\hbar}{i}\nabla-\frac{e_s}{c}\overrightarrow{A}\right)\Psi|_n=\frac{i\hbar}{b}\Psi, \quad (1.11)$$

where $b>0$ is a real constant, to take into account the leakage of Cooper pairs from the superconductor into the metal. In analogy, $b<0$ models the interface with a superconductor with higher T_c.

The physical meaning of the order parameter was explained by the later microscopic BCS theory, however, the square of its absolute value in GL theory is regarded as the density of the superconducting electrons. Without exploring the underlying microscopic mechanism of superconductivity, this theory correctly describes some of the superconducting phenomenon and introduces both of the two characteristic lengths in superconductivity (see in Fig. 1.3): the magnetic field penetration depth λ and the coherence length ξ which characterizes the spatial variations of the order parameter. The GL theory is valid in the vicinity of T_c.

Considering the validity of the Ginzburg-Landau equations, several points need to be discussed [17]:

Firstly, Landau general theory of second order transitions assumes that the free energy can be expanded in powers of Ψ. Second, the coefficient α is assumed positive in high temperature phase, changes sign at the transition and becomes negative under the critical temperature ($\alpha\sim(T-T_{c0})$), while β is a positive constant, independent on temperature. None of these assumptions are generally applicable, but Gor'kov showed theoretically that the Landau expansion is valid in the case of superconductors.

Ψ must be a slowly varying function over distances of the order of ξ_0. A necessary condition for the validity of the theory is, therefore, $\xi(T) >> \xi_0$. From the temperature dependence of the coherence length (see previous paragraph) follows the condition

$$\frac{T - T_{c0}}{T_{c0}} << 1, \tag{1.12}$$

meaning that this condition is fulfilled only for temperatures close to T_{c0}, the critical temperature in zero field.

The local relation between the current and the vector potential, yielded by the Ginzburg-Landau equations, will be valid only if $\overrightarrow{H}$ and $\overrightarrow{A}$ are slowly varying functions over distances of the order of ξ_0. In order for this to be true, it is necessary that $\lambda(T) >> \xi_0$, leading to the relation

$$\frac{T - T_{c0}}{T_{c0}} << \left(\frac{\lambda_L(0)}{\xi_0}\right)^2, \tag{1.13}$$

which sets us back to the condition of temperatures close to T_{c0}.

Despite the above criteria, and ensured applicability only close to the superconducting/normal transition, it turns out that the validity range of the Ginzburg-Landau theory is much larger. In particular, in mesoscopic superconductors the Ginzburg-Landau theory has been successfully used deep into the superconducting phase. De Gennes demonstrated that the GL model is valid for any temperatures in strong magnetic fields. Comparison of the critical current measurements in thin Al stripes with the theoretical predictions of BCS and GL formalisms showed that two theories agree with each other up to very low temperatures (below $0.1T_c$). Substantiated by the experimental findings, it appears that due to the small mean-path-length in the samples, the GL theory is more relevant in this case. Actually, most of the mesoscopic superconductors are in the so-called "dirty" limit, and that is the main reason of the phenomenologically proven applicability of the GL formalism far away from the S/N boundary.

1.1.3 Microscopic theory

The formalism of the microscopic theory was not used in the research, therefore, is not included in this thesis. So, we limit the discussion of the BCS theory to the basics.

The foundation of the BCS theory is that electrons in the Debye window around the Fermi level with opposite momenta and spins are bounded into Cooper pairs due to the attractive electron-electron interaction mediated by phonons. Such binding will occur in the presence of an attractive potential, no matter how weak. In conventional superconductors, an attraction is generally attributed to an electron-lattice interaction. The BCS theory, however, requires only that the potential be attractive, regardless of its origin. The wave function of such a pair is symmetric under renumbering of the electrons and thus essentially represents a boson. Since bosons do not have to obey the Pauli-principle they can all occupy

the same lowest energy state. In other words, the theory describes superconductivity as a microscopic effect caused by a "condensation" of pairs of electrons into a boson-like state at sufficiently low temperature. This way a coherent sea of superconducting electrons is formed.

In many superconductors, the attractive interaction between electrons is brought about indirectly by the interaction between the electrons and the vibrating crystal lattice (*the phonons*). Roughly speaking the picture is the following:

An electron moving through a conductor will attract nearby positive charges in the lattice. This deformation of the lattice causes another electron, with opposite "spin", to move into the region of higher positive charge density. The two electrons then become correlated. There are a lot of such electron pairs in a superconductor, so that they overlap very strongly, forming a highly collective "condensate". Breaking of one pair results in changing of energies of remained macroscopic number of pairs. If the required energy is higher than the energy provided by kicks from oscillating atoms in the conductor (which is true at low temperatures), then the electrons will stay paired and resist all kicks, thus not experiencing resistance. When a current is generated in a superconductor, the Cooper pairs move collectively and unperturbed through the crystal lattice since they cannot absorb energies smaller than the Cooper pair binding energy.

BCS theory starts from the assumption that there is some attraction between electrons, which can overcome the Coulomb repulsion. In most materials (in low temperature superconductors), this attraction is brought about indirectly by the coupling of electrons to the crystal lattice (as explained above). However, the results of BCS theory do not depend on the origin of the attractive interaction. The original results of BCS described an "s-wave" superconducting state, which is the rule among low-temperature superconductors but is not realized in many "unconventional superconductors", such as the "d-wave" high-temperature superconductors. Extensions of BCS theory exist to describe these other cases, although they are insufficient to completely describe the observed features of high-temperature superconductivity.

BCS derived several important theoretical predictions that are independent of the details of the interaction, since the quantitative predictions mentioned below hold for any sufficiently weak attraction between the electrons and this last condition is fulfilled for many low temperature superconductors - the so-called "weak-coupling case". These have been confirmed in numerous experiments:

* The electrons are bound into Cooper pairs, and these pairs are correlated due to the Pauli exclusion principle for the electrons, from which they are constructed. Therefore, in order to break a pair, one has to change energies of all other pairs. This means there is an "energy gap" for "single-particle excitation", unlike in the normal metal (where the state of an electron can be changed by adding an arbitrarily small amount of energy). This energy gap is highest at low temperatures but vanishes at the transition temperature when superconductivity ceases to exist. The BCS theory gives an expression that shows how the gap grows with the strength of the attractive interaction and the (normal phase) single particle density of states at the Fermi energy. Furthermore, it describes how the density of states is changed on entering

the superconducting state, where there are no electronic states any more at the Fermi energy. The energy gap is most directly observed in tunneling experiments and in reflection of microwaves from the superconductor.

* BCS theory predicts the dependence of the value of the energy gap E at temperature T on the critical temperature T_c. The ratio between the value of the energy gap at zero temperature and the value of the superconducting transition temperature (expressed in energy units) takes the universal value of 3.5, independent of material. Near the critical temperature the relation asymptotes to

$$E = 3.52 k_B T_c \sqrt{1 - T/T_c}. \tag{1.14}$$

* Due to the energy gap, the specific heat of the superconductor is suppressed strongly (exponentially) at low temperatures, there being no thermal excitations left. However, before reaching the transition temperature, the specific heat of the superconductor becomes even higher than that of the normal conductor (measured immediately above the transition) and the ratio of these two values is found to be universally given by 2.5.

* BCS theory correctly predicts the Meissner effect, i.e. the expulsion of a magnetic field from the superconductor and the variation of the penetration depth (the extent of the screening currents flowing below the metal's surface) with temperature.

* It also describes the variation of the critical magnetic field H_{c2} (above which the superconductor can no longer expel the field but becomes normal conducting) with temperature. BCS theory relates the value of the critical field at zero temperature to the value of the transition temperature and the density of states at the Fermi energy.

* In its simplest form, BCS gives the superconducting transition temperature in terms of the electron-phonon coupling potential and the Debye cutoff energy:

$$k_B T_c = 1.14 E_D, e^{-1/N(0)V}, \tag{1.15}$$

where $N(0)$ is the electronic density of states at the Fermi energy.

* The BCS theory reproduces the isotope effect, which is the experimental observation that for a given superconducting material, the critical temperature is inversely proportional to the mass of the isotope used in the material.

1.2 Type I and type II superconductors

It became understood in the 1950s that superconductors fall into two classes, depending on the sign of the surface energy of a superconducting-normal interface.

Almost all of the pure elementary superconductors studied before 1940 proved to be of type I, with a positive interface energy. Type I superconductors show a reversible first-order phase transition with a latent heat when the applied field reaches B_c; and at this particular field relatively thick normal and superconducting domains running parallel to the field can coexist, in what is known as the *intermediate state*.

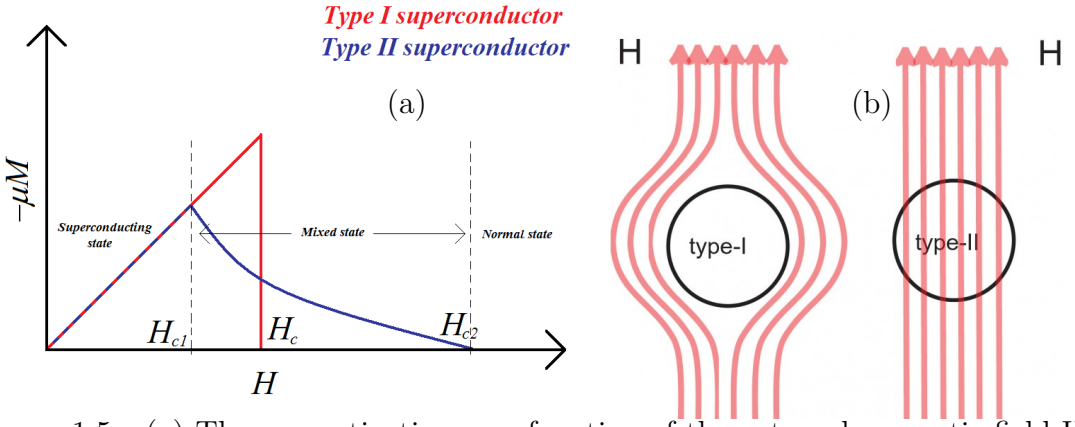

Figure 1.5: (a) The magnetization as a function of the external magnetic field H in type I and type II superconductors. (b) Penetration of magnetic field in type I and type II superconductors.

It had been known since the 1930s that superconducting alloys often contained trapped magnetic flux, showed a large magnetic hysteresis and continued to be superconducting at fields much greater than the thermodynamic critical field B_c predicted from their heat capacities. For many years this was put down to 'dirt effects' — supposed inhomogeneities, with some sort of network of highly superconducting regions threading a matrix with much weaker condensation — but in 1951 a new and important phenomenological theory proposed by Ginzburg and Landau made it possible to calculate the behavior of superconductors in which the order parameter varied strongly from point to point. It gradually became clear that alloys were simply type II superconductors, with a negative interface energy and that many of their properties were intrinsic. In such materials finally divided *quantized flux vortices* or *flux lines* entered the material over a range of applied fields below B_c, and remained stable over a range of applied fields extending far above B_c, in what became known as the *mixed state*. If these flux lines were *pinned* by lattice defects or other agencies, the type II superconductor could carry a large supercurrent, greatly exceeding the Silsbee's rule criterion, in very high magnetic fields. It was this which made possible the development during the 1960s and 1970s of useful high-field superconducting magnets.

1.3 Direct observation of vortices in superconductors by using a field-emission electron microscope

Vortices can be detected by using the phase shift of an electron wave which interacts with the magnetic fields of the vortices.

Observation Principle

The principle behind the observation of vortices is based on the use of the phase information of an electron wave transmitted through magnetic fields of vortices. The phase shift of electron waves due to electromagnetic fields can be derived using the Schrödinger equation. When the effect of electromagnetic fields on electron waves is weak, the relative phase shift ΔS between two beams starting from the same point, passing through points A and B in electromagnetic fields ($\overrightarrow{A}$, φ), and combining at another point is calculated as follows:

$$\Delta S = \frac{1}{\hbar}\oint(m\overrightarrow{v} - e\overrightarrow{A})d\overrightarrow{s} = \frac{1}{\hbar}\oint(\sqrt{2me\varphi} - e\overrightarrow{t}\cdot\overrightarrow{A})ds. \tag{1.16}$$

Here $\overrightarrow{t}$ is the unit tangent vector of the electron trajectory and the integration is carried out along a closed loop connecting the two electron trajectories. This equation shows that the phase shift in an electron beam is determined by electromagnetic potentials ($\overrightarrow{A}$, φ) rather than electromagnetic fields ($\overrightarrow{E}$, $\overrightarrow{B}$).

Aharonov and Bohm asserted that an electron beam can be affected physically (phase-shifted) by potentials even when it passes through field-free regions on both sides of an infinitely long solenoid and is therefore subjected to no forces. This Aharonov-Bohm effect was confirmed by using toroidal ferromagnets.

Observation of vortices inside superconductors

Vortices inside a superconductor can be observed when an electron beam passes through a thin-film sample. The experimental arrangement for observing vortices in a superconductor is shown in Fig. 1.7. When a superconducting thin film is tilted and a magnetic field is applied horizontally, electrons passing through vortices in the film are phase-shifted, or deflected, by the magnetic fields of the vortices. Consequently, when the phase distribution is observed as an interference micrograph, projected magnetic lines of force can be observed. However, by using this method it is not easy to observe dynamics of vortices. This can be done more easily by using Lorentz microscopy, in which vortices can be observed by simply defocusing the electron microscopic image. That is, when the intensity of electrons is observed in a out-of-focus plane, a vortex appears as a pair of bright and dark contrast features (Fig. 1.7).

Peculiar vortex pinning in an array of pinning centers

The vortex pinning behaved completely differently when the pinning centers were densely arranged. This change in behavior occurred especially for a regular array of artificial point defects produced in a Nb thin film, where vortices formed regular and rigid configurations at specific values of magnetic fields. The net pinning force increased at these specific magnetic fields, which is known as the

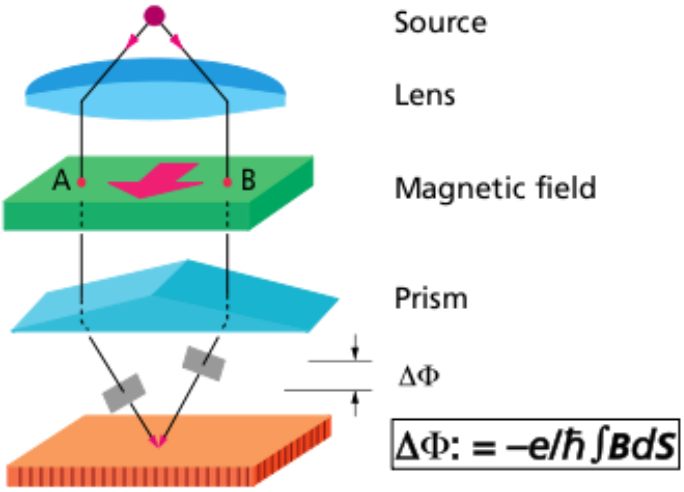

Figure 1.6: Phase shift of electron beams enclosing magnetic flux. A relative phase shift between two electron beams starting from a source point, passing through points A and B in a magnetic field, and combining at an observation point is proportional to the magnetic flux enclosed by the two beam paths.

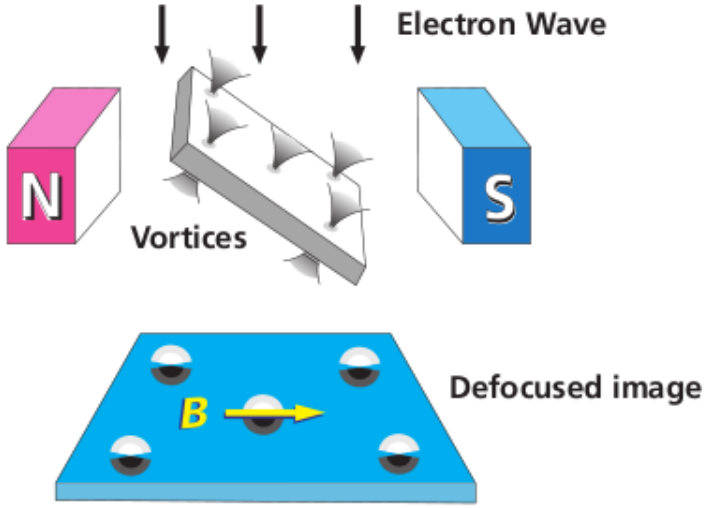

Figure 1.7: Principle behind vortex observation. An incident electron wave is phase-shifted, or deflected, by the magnetic fields of vortices. In the defocused image, a vortex appears as a spot consisting of black-and-white contrast (Lorentz microscopy).

peak effect or the matching effect of the critical current, found by macroscopic measurements. Lorentz micrographs showing the configurations of vortices relative

to defect positions are shown in Fig. 1.8. At the matching magnetic field H_1 (Fig. 1.8(b)), all the defects are occupied by vortices and the lattice formed is a rigid square one. The peak effect of the critical current observed macroscopically can be explained microscopically: when vortices form a stable and regular lattice without vacancies, even if a vortex is depinned from one pinning site due to thermal excitation, it can find no vacant site to move to. As a result, a stronger force is required to move the vortices. Regular lattices were formed not only at $H = H_1$ (matching magnetic field, see Fig. 1.8(b)) but also at $H = mH_1/n$ (n and m; integers) as in the case of $H = 4H_1$ (Fig. 1.8(a)). In this vortex configuration, defect positions forming a square lattice were first occupied by vortices. Then two vortices aligned in the vertical direction were inserted at every interstitial site, and finally an additional vortex was inserted in the middle of two adjacent defects located vertically. Figure 1.8(c) shows the case at $H = 1/4H_1$. Vortices occupy every fourth site in the horizontal direction, thus forming a centered (4×2) rectangle lattice. The reason the pinning force as a whole becomes stronger at the specific values of magnetic fields comes from the fact that vortices form rigid and regular lattices.

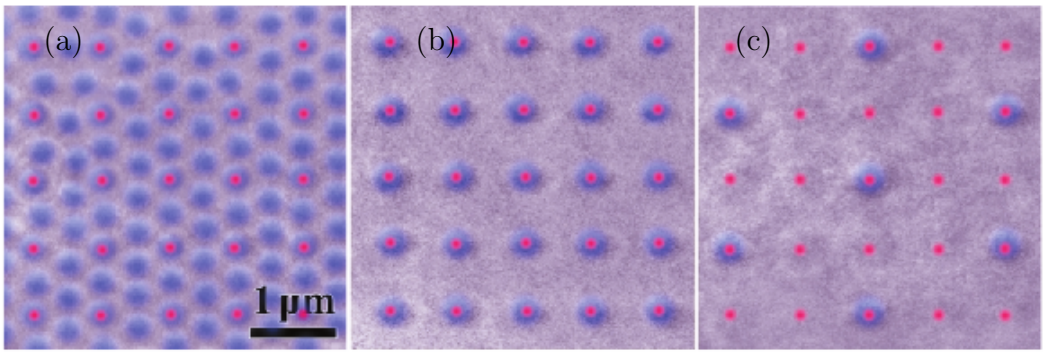

Figure 1.8: Lorentz micrographs of vortices. (a) $H = 4H_1$ (H_1: matching magnetic field); (b) $H = H_1$; (c) $H = 1/4H_1$. Purple vortices form a regular and rigid lattice at these specific magnetic fields. If one of these vortices is thermally depinned from its red site by any chance, it cannot find a stable vacant site to hop to, thus producing a strong pinning effect.

1.3.1 Other vortex visualization techniques

Bitter decoration is performed by diffusing iron clusters of a few tens of nanometer diameter produced by thermal evaporation in coolant temperature. The evaporated iron clusters are attracted by magnetic field gradient and decorated individual vortices. Decorated vortex arrangements are observed by a scanning electron microscope at room temperature. Distribution of vortices is visualized by Magneto-optical imaging (MOI) method using a garnet film with in-plane magnetization.

However, on using the Bitter pattern decoration technique in a niobium superconducting disk, Grigorieva *et al.* observed clusters of multivortex states coexisting

with giant vortices. In another work, Cren *et al.* studied the vortex states in ultrathin single nanocrystals of *Pb* with random geometries via scanning tunneling microscopy. The images were taken under several values of applied field and at very low temperature. They showed that under certain conditions of magnetic field and sample size, a giant vortex is formed and in the vicinity of the core center the order parameter evolves as $\Psi \propto r^L$ where L is the vorticity.

MOI has previously been shown to be a very useful technique for studying flux penetration into BSCCO mesostructures [18]. A schematic of the experimental setup is shown in Fig. 1.9. The technique exploits the magneto-optical Faraday effect: the rotation of the plane of polarization of light in the presence of a magnetic field. Key to the emergence of MOI as a tool for detecting stray fields on mesoscopic superconductors was the development of ferrimagnetic garnet films with in-plane anisotropy, which greatly enhance the sensitivity of the system [19]. In this instance, a Bi-doped yttrium iron garnet film was pressed into intimate contact with the sample using screws. The whole assembly was then attached to the cold head of a cryocooler for imaging experiments. Further details of the garnet and the entire measurement system can be found in the literature [20].

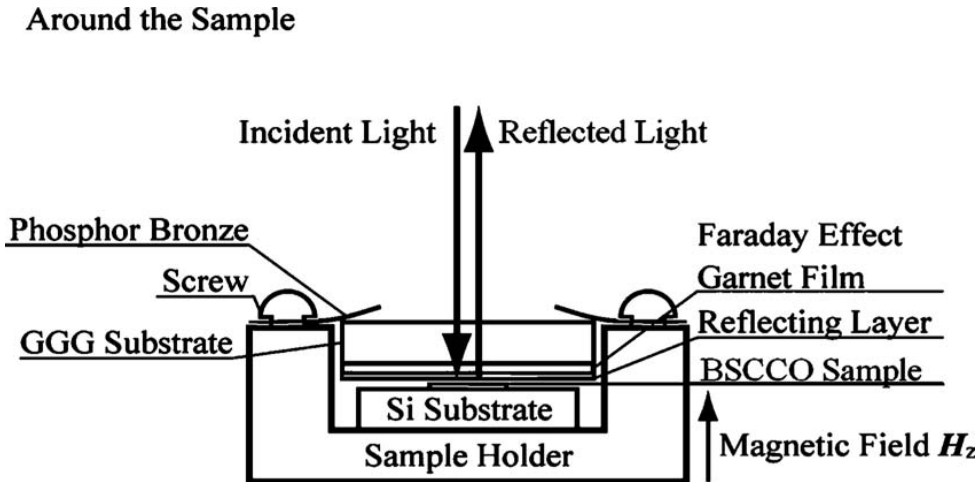

Figure 1.9: Schematic of the experimental magneto-optical imaging setup. (See Ref. [21])

1.4 Experiments on controlling magnetic flux

A net flow of particles under unbiased external fluctuations/drive due to an asymmetric potential, which is called ratchet effect, has received much attention during the last decades. The transport and dynamical properties of particles on asymmetric potential have been widely studied, e.g., in physics and biology. The random motion of particles can be rectified in such an asymmetric system, which can be used for, e.g., controlling particle motion, separating different types of particles (i.e., molecular sieves), for both underdamped and overdamped particles and for

molecular motors. Vortices in a type II superconductor often (e. g., for magnetic field close to H_{c1}) can be treated as classical overdamped "particles". Most of the experiments on vortex motion rectification used arrays of asymmetric pinning sites (e.g., nanoengineered antidots or triangular magnetic dots/impurities) to create an asymmetric potential, which rectifies the motion of vortices. The rectified vortex motion was directly observed in experiments by imaging vortices via Lorentz microscopy. Periodic arrangement of point defects of a gradual density or periodic square array of ferromagnetic dots of decreasing size, i.e., varying the density of pinning sites or the size of pinning sites, were shown to result in a ratchet potential.

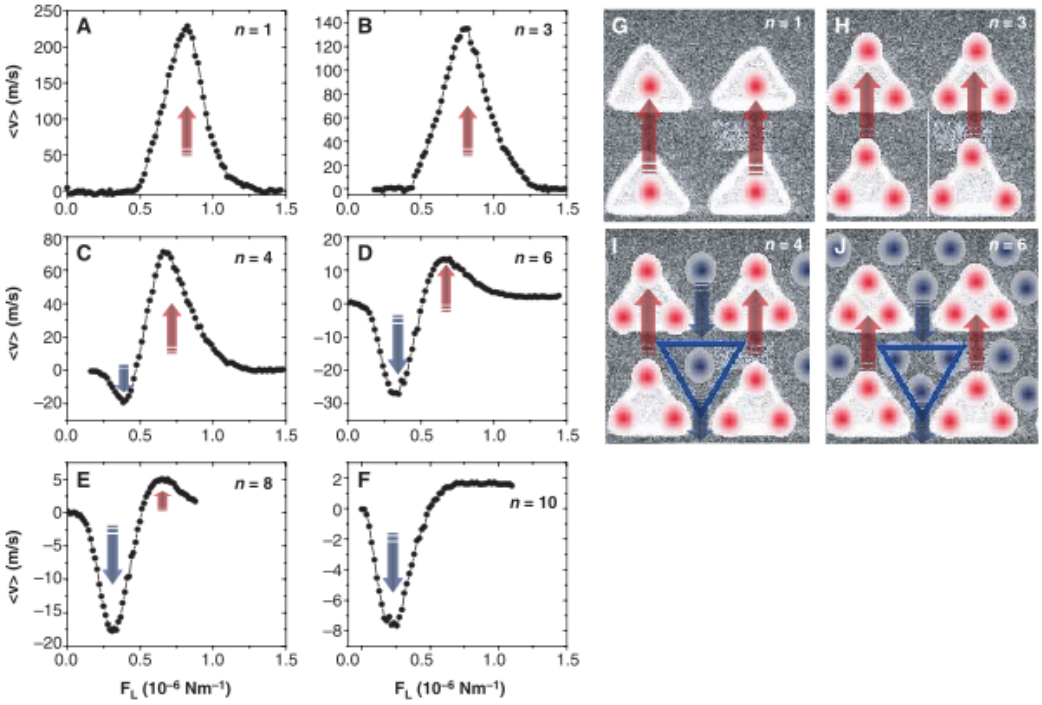

Figure 1.10: (A to F) Net velocity $\langle v \rangle$ of vortices versus the ac Lorentz force amplitude ($\omega = 10kHz$), for several matching magnetic fields at $T = 0.98T_c$; n indicates the number of vortices per unit cell of the array. Red and black arrows show the direction of the net flow of these vortices. (G to J) Sketch of the positions of the vortices for several matching fields. Vortices pinned on the triangles are shown in red and interstitial vortices in blue.

When vortices are trapped by pinning sites, the repulsive vortex-vortex interaction creates a higher energy barrier near the area with higher density of pinning sites. Therefore, an asymmetric potential can be created by the gradient of the density of pinning sites. Even without spatial asymmetry (i.e., without any asymmetric walls/boundaries or asymmetric pinning sites), the motion of vortices still can be controlled by time-asymmetric driving force. Due to the possibility of controlling their motion, the dynamical behavior of vortices in such systems has attracted considerable interest. A series of elastic and plastic vortex flow phases were found. Besides the liquid-like and solid lattice phase, vortex motion also revealed a jamming behavior. When the density of vortices is changed, the vortex

flowing direction can change to the opposite, which means vortices can drift in either the "hard" direction or the "easy" direction of the ratchet, depending on the vortex density (e.g., see Fig. 1.10). By controlling the motion of vortices, it is possible to remove vortices or reduce the vortex density by using a combination of two opposite oriented ratchet arrays. The order of vortices and commensurability between vortices and cells also play an important role in vortex dynamics. In two-dimensional $(2-D)$ ratchets, the dynamics in the transverse ratchet was first predicted theoretically and then further studied in theory and in experiments.

For studies of vortex matter in confined geometries, nanoscale channels for guiding vortices through superconducting films with a minimal influence from pinning have been developed, including experiments on melting, commensurability, mode-locking, and ratchet effect.

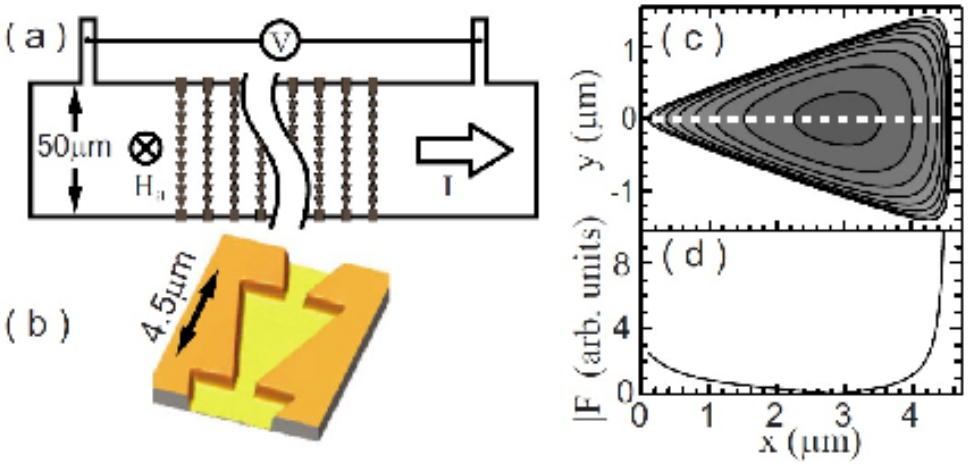

Figure 1.11: (a) Schematic of strip with ratchet channels; channel spacing is $10\mu m$. (b) AFM image of one ratchet cell; channel depth is $88nm$. (c) Contour plot of the model potential for a vortex interacting with ratchet cell walls. (d) Magnitude of the corresponding force along the center of the channel.

Such channels are fabricated from bilayer films of an extremely weak-pinning superconductor and a relatively strong pinning superconductor, (i. e., amorphous-$NbGe$ and NbN). A reactive ion etching process removes NbN from regions as narrow as $100nm$, defined with electron-beam lithography, to produce weak-pinning channels for vortices to move through easily, while vortices trapped in the NbN banks outside of the channels remain strongly pinned. E.g., in the experimental group of Plourde, they have fabricated weak-pinning channels with $200nm$ thick films of $a-NbGe$ and $50nm$ thick films of NbN on a Si substrate, and many of the channels such that the walls have an asymmetric sawtooth pattern has been designed (see Fig. 1.11). Such channels are fabricated from bilayer films of amorphous-$NbGe$, an extremely weak-pinning superconductor, and NbN, with relatively strong pinning.

In experiment of Y. Togawa *et al.*, the number of vortices in the system was altered by changing the applied magnetic field. Thus, their system in Fig. 1.12

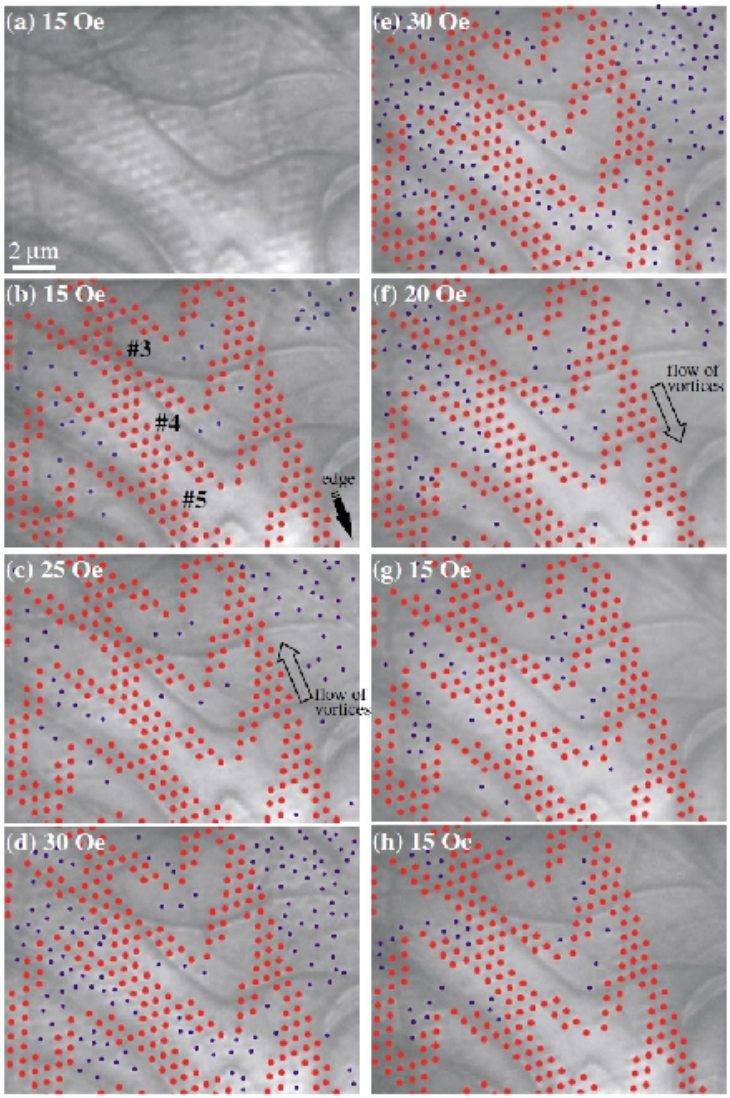

Figure 1.12: Sequence of Lorentz image snapshots of moving vortices in a period of the ac applied magnetic field at $6.9K$. Pinned and unpinned vortices are represented by red and blue circles, re- spectively, in (b)-(h). (a) and (b) are the same snapshot. (b)-(d) With increasing magnetic field H, vortices flow upward; (e)-(g) With decreasing magnetic field H, vortices flow downward. Arrows indicate the directions toward the edge of the sample, and the flow of vortices.

is an open system where the total number of vortices is a variable. To illustrate a different way to control the motion of vortices, they made a "closed loop", where the number of vortices was fixed because these cannot escape through the (red) regions with pinned vortices. The rectification of vortices in a closed system provides a novel demonstration of the ability to control the motion in $2D$ channels, where the vortex path can bend and take turns as opposed to just moving along one (or several adjacent parallel) linear $1D$ track(s). The initial state was prepared using the field-cooling process described above. Magnetic field H was periodically

oscillated between 26 and 46 Oe. The vortices inside the loop were exposed, via the long-range Pearl potential, to a time-dependent field gradient (i.e., a force) produced by the variations of $B(t)$ outside the pinned vortex area (which was located near the sample edge). This drove the inner vortices. With increasing H from 26 Oe to 46 Oe, vortices began to turn around toward another channel directed the opposite way. In this (nonoptimized) regime of parameters, the net motion of vortices in each cycle was small. Y. Togawa *et al.* observed such rectification of vortices every four cycles of changing H in three parts out of four funnels connecting straight channels and curved regions. A rough estimate (not a direct observation) indicated that after 350 cycles vortices should go through the loop.

The transport of oscillatory field-gradient-driven vortices observed in this closed loop suggests novel ways to transport vortices one by one along curved paths, including cyclic vortex "conveyor belts and pumps. Also, the energy of vortices moving in circles, as authors claim, could be extracted as a dc voltage output along a radial direction.

1.5 Applications of superconductivity

Superconducting magnets are some of the most powerful electromagnets known. They are used in MRI and NMR machines, mass spectrometers, and the beam-steering magnets used in particle accelerators such as a high magnetic field magnets for experiments (LHC at CERN, etc.). In some fields like fusion and high energy physics HEP superconductivity has enabled new science and technology that could not exist without it.

Promising future applications include high-performance smart grid, electric power transmission, transformers, bearings [22], power storage devices [23], electric motors (e.g., for vehicle propulsion, as invactrains or maglev trains), magnetic levitation devices, fault current limiters, nanoscopic materials such as buckyballs, nanotubes, composite materials and superconducting magnetic refrigeration.

High-Tc superconducting gave life to magnetically levitated (Maglev) vehicles [24]. It provides such substantial advantages like non-contact and low noise movement above a magnetic rail, see Fig. 1.13. China's locomotive jewel is the Maglev in Shanghai. A train that floats on magnets and can reach a cruising speed of around 500 Km/h pretty fast in our standards, but obviously not fast enough. Jiaotong University current have a prototype Maglev that can hit 600 Km/h and are planning a smaller 'Express' version which will hit the dizzying speed of 1000 Km/h!

Based on superconducting loops with two Josephson junctions (JJ), the direct current superconducting quantum interference device (DC SQUID, as seen in Fig. 1.8) is the most sensitive magnetometer with an accuracy as high as $5 \times 10^{-18}T$. For comparison, the earth's magnetic field is of the order of $10^{-4}T$, and some processes in animals produce magnetic fields between $10^{-9}T$ and $10^{-6}T$.

Superconductors are used to build JJ which are the building blocks of SQUIDs (superconducting quantum interference devices), the most sensitive magnetometers known. By means of Josephson junctions, voltages can be reproduced with relative uncertainties of less than one part in ten billion ($1 : 10^{10}$, i.e. $1\ nV$ at $10\ V$). The

Figure 1.13: Shanghai Maglev train floats on magnets and can reach a cruising speed of around 500Km/h, Shanghai. (See Ref. [25])

Josephson effect is therefore world-wide used as a basis for constant reference voltages in metrological national institutes and in calibration laboratories of industry. As the Josephson constant is not known with the needed accuracy, the same agreed value is used everywhere for these purposes. Large series arrays are fabricated consisting of several ten thousand Josephson junctions which are connected so that voltages up to 10 V can be generated. These series arrays are the main components of modern Josephson voltage standards.

Another promissing implementation of superconductors are fast and low-power-consumption computers [26]. The superconducting computation electronics is based on magnetic flux transfer, rather than the electric charge as in semiconductor devices. Rapid single flux quantum (RSFQ) logic is operating with the flux quantum inside the device: logical states (0/1) in this architecture are represented by the presence or the absence of the magnetic flux. Surprisingly, power consumption of such devices is two orders of magnitude smaller than conventional computers. Current superconductor technology may operate at several hundred GHz frequency, which is two order of magnitude higher than semiconductors.

Superconducting tunnel junction detectors (STJs) may become a viable replacement for CCDs (charge-coupled devices) for use in astronomy and astrophysics in a few years. These devices are effective across a wide spectrum from ultraviolet to infrared, and also in x-rays. The technology has been tried out on the William Herschel Telescope in the SCAM instrument.

Flywheel energy storage systems (FESS) are suited for the storage of electricity and have already been applied for a number of years using mechanical bearings. In 1988 flywheels of 2 kWh/150 kW from Magnet-Motor Corp., Starnberg, Germany were first applied in two communal diesel-electric buses in Munich, Germany. Further diesel-electric demonstration buses followed. In those years experience could be gained on the operation of flywheels in vehicles, their interaction with the electric propulsion system, the potential of energy saving in buses, reliability and maintenance needs. One important result was that energy savings of 30–35% can

be obtained if you regard only the energy balance of the diesel-electric propulsion system including the flywheel. In 1994/95 a small fleet of 12 trolleybuses in the Swiss city of Basel was built, equipped with flywheel units to relieve the overhead network and to recover the brake energy on-board. These buses have been in operation for more than 12 years. Most of these flywheels have operational hours of more than 50 000. They operate very reliably, provide energy savings of 20–25% and have an MTBF of about 38 000 hours, which means that a repair on a flywheel is necessary only every 8 years. The steel or composite rotors can also be stabilized by superconducting magnetic bearings (SMB). The principal benefit of SMB stems from low-drag torque and the self-centering, unlubricated, wear-free and vacuum-compatible operation.

Only few superconductor have become commercial. The notable events in this regard were the discovery of Nb_3Sn in 1954 and its wire development in 1961. There followed quickly the discovery of other A15 materials and $NbTi$, the currently most-used material. Niobium-titanium ($NbTi$) is a workhorse in commercial power applications. The large-scale use of superconductivity continues to be dominated by applications for which there is generally a conventional technical option. However, superconductivity is sensitive to moving magnetic fields so applications that use alternating current (e.g., transformers) is more difficult to develop than those that rely upon direct current.

Chapter 2

Numerical solution of the time-dependent Ginzburg-Landau equations for rectangular superconducting stripe with magnetic dots on top: Periodic and Neumann boundary conditions

The superconducting state is described by the complex order parameter $\Psi(\overrightarrow{r})$. The quantity $|\Psi|^2$ represents the density of Cooper pairs. In the regions where $|\Psi|^2$ is small, superconductivity is suppressed. At the center of the vortex $|\Psi|^2 = 0$, whereas the local magnetic field $\overrightarrow{H}$ is maximum. The order parameter and the local magnetic field can be determined by the time-dependent Ginzburg-Landau (TDGL) equations. In this chapter, we describe the algorithm for numerical solution of the TDGL. In this thesis, the methodology was modified, namely: (i) periodic boundary conditions for the appropriate variables were introduced, and (ii) magnetic field distributions produced by out-of-plane and in-plane dipoles were implemented. The results of the Chapter does not represent an original development of the methodology. This methodology was earlier used in Ref. [64] (see thesis, please) and in other works.

2.1 Dimensional units

In this section we introduce the following dimensional units:

$[\sigma] = \sigma_n$ - normal state conductivity

$[t] = \frac{4\pi\lambda^2\sigma_n}{c^2} = \tau$ - GL time

$[x] = [y] = \xi$ - unit length

$[\Psi] = \sqrt{\frac{|a|}{b}}$ - order parameter (OP)

$[A] = \frac{\hbar c}{e_s \xi} = \frac{\Phi_0}{2\pi\xi}$ - magnetic field vector-potential, where $\Phi_0 = \frac{2\pi\hbar c}{e_s}$ is quantum of the magnetic flux

$[\varphi] = \frac{c\Phi_0}{8\pi^2\lambda^2\sigma_n}$ - electric potential

$[j_s] = \frac{c\Phi_0}{8\pi^2\lambda^2\xi}$ - density of superconducting current

$[E] = \frac{c\Phi_0}{8\pi^2\lambda\sigma_n\xi}$ - electric field

$[\theta] = \frac{\Phi_0}{2\pi c}$ - phase of the order parameter

$[T] = T_c$ - temperature.

Parameters related to the superconductor (material parameters):

$\lambda = \sqrt{\frac{m_s c^2}{4\pi\Psi_0^2 e_s^2}}$ - magnetic field penetration depth

$\xi = \sqrt{\frac{\hbar^2}{2m_s|a|}}$ - coherence length

$\kappa = \lambda/\xi$ - GL parameter

$a(T) = N(0)\frac{T-T_c}{T_c}$ - phenomenological parameter a

$b(T) = 0.098\frac{N(0)}{(k_b T_c)^2}$ - phenomenological parameter b.

Time scaling:

$$\frac{\partial}{\partial t} = \frac{\partial t'}{\partial t} \cdot \frac{\partial}{\partial t'} = \frac{1}{\tau} \cdot \frac{\partial}{\partial t'}. \tag{2.1}$$

Where the t is old variable and the t' is the new one. The scaling coefficient (or time unit) is τ.

Length scaling:

$$\nabla = \frac{1}{\xi}\nabla' <=> \nabla^2 = \frac{1}{\xi}\nabla'(\frac{1}{\xi}\nabla') = \frac{1}{\xi^2}\nabla'^2. \tag{2.2}$$

Where the x is old variable and the x' is the new one. The scaling coefficient (or length unit) is ξ.

$$\nabla = \overrightarrow{i}\frac{\partial}{\partial x} + \overrightarrow{j}\frac{\partial}{\partial y} + \overrightarrow{k}\frac{\partial}{\partial z} = \wr x = \xi x' \wr = \frac{1}{\xi}(\overrightarrow{i}\frac{\partial}{\partial x'} + \overrightarrow{j}\frac{\partial}{\partial y'} + \overrightarrow{k}\frac{\partial}{\partial z'}) = \frac{1}{\xi}\nabla'. \tag{2.3}$$

2.2 Derivation of dimensionless equations

The TDGL equations are very often written in a form which introduces only dimensionless quantities. The first equation for the order parameter coupled with the magnetic vector-potential (see Ref. [27]) is:

$$\frac{u\hbar^2}{2m_s D}\left(\frac{\partial}{\partial t} + \frac{ie_s}{\hbar}\varphi\right)\Psi + \frac{1}{2m_s}\left(\frac{\hbar}{i}\nabla - \frac{e_s}{c}\overrightarrow{A}\right)^2\Psi - \left(|a|\Psi - b|\Psi|^2\Psi\right) = 0. \tag{2.4}$$

Here, Ψ is the (complex-valued) order parameter, $\overrightarrow{A}$ the vector potential, and φ the electric potential. The constant D is a phenomenological diffusion coefficient. e_s is the "effective charge" of a Cooper pair, and m_s its "effective mass". The quantities a and b are phenomenological parameters; they are functions of external parameters, such as the temperature T, the concentration of impurities, etc.; $b > 0$ for all T, and a changes sign at T_c ($a < 0$ for $T < T_c$, $a > 0$ for $T > T_c$). Parameter u governs the time change of $|\Psi|$ and the length of penetration of the electric field into a superconductor. Since we are interested mainly in the dynamics of (anti-)vortex motion but not in the time evolution of the v-av nucleation and annihilation, for our problem the actual value of u does *not* play an essential role, and we choose $u = 5.79$ (note that this value depends on the specific superconductor).

Applying the transformations 2.1, one can obtain:

$$u\left(\frac{\partial}{\partial t} + i\varphi\right)\Psi = \left(\nabla - i\overrightarrow{A}\right)^2\Psi + \Psi\left(1 - |\Psi|^2\right). \tag{2.5}$$

The second equation for the superconducting current coupled with the magnetic vector-potential (see Ref. [27]) is:

$$rotrot\overrightarrow{A} = -\frac{4\pi\sigma}{c}\left(\frac{1}{c}\cdot\frac{\partial\overrightarrow{A}}{\partial t} + \nabla\varphi\right) + \frac{4\pi}{c}\overrightarrow{j_s}. \tag{2.6}$$

This equation is Ampere's law, $\nabla\times\overrightarrow{B} = \frac{4\pi}{c}\overrightarrow{j}$; see [[28], Chap. 5]. The superscript "*" denotes complex conjugation. After simplification:

$$k^2\cdot\nabla\times\nabla\times\overrightarrow{A} = -\sigma\left(\frac{\partial\overrightarrow{A}}{\partial t} + \nabla\varphi\right) + \overrightarrow{j_s}. \tag{2.7}$$

Here $\overrightarrow{j_s}$ is:

$$\overrightarrow{j_s} = \frac{e_s\hbar}{2im_s}\left(\Psi^*\nabla\Psi - \Psi\nabla\Psi^*\right) - \frac{e_s^2}{cm_s}|\Psi|^2\overrightarrow{A}. \tag{2.8}$$

Or, in dimensionless units:

$$\overrightarrow{j_s} = \frac{1}{2i}(\Psi^*\nabla\Psi - \Psi\nabla\Psi^*) - |\Psi|^2\overrightarrow{A}, \text{ where } \overrightarrow{j_s} = \overrightarrow{j_{tot}} - \sigma\overrightarrow{E}. \tag{2.9}$$

$\overrightarrow{j_{tot}}$ is viewed as the sum of a "normal" current, which satisfies Ohm's law, and the supercurrent $\overrightarrow{j_s}$, σ is interpreted as the "coefficient of normal conductivity".

At a free surface of the system one must satisfy the boundary condition that no current flows out of the superconductor into the vacuum:

$$\left(\nabla - i\overrightarrow{A}\right)\Psi\Big|_n = 0. \tag{2.10}$$

The obtained boundary condition is suitable for a superconductor in a dielectric medium (or vacuum) and means that no superconducting current passes through the superconductor-dielectric interface.

2.3 Gauge invariance and zero electric potential gauge

In this section we demonstrate the gauge invariance for the equations under the transformations: $\varphi' = \varphi - \frac{\partial \chi}{\partial t}$, $\Psi' = \Psi e^{i\chi}$, $\overrightarrow{A'} = \overrightarrow{A} + \nabla\chi$, where χ is any scalar function. Values with a prime "′" denote the new gauge and values without the old gauge. These substitutions allow us to simplify the TDGL equations.

$$u\left(\frac{\partial}{\partial t} + i\varphi'\right)\Psi e^{i\chi} = \left(\nabla - i\overrightarrow{A'}\right)^2 \Psi' + \Psi e^{i\chi}(1 - |\Psi|^2), \tag{2.11}$$

$$u\frac{\partial \Psi}{\partial t}e^{i\chi} + \cancel{iu\Psi e^{i\chi}\frac{\partial \chi}{\partial t}} + iu\varphi\Psi e^{i\chi} - \cancel{iu\Psi e^{i\chi}\frac{\partial \chi}{\partial t}} =$$
$$e^{i\chi}\left(\nabla - i\overrightarrow{A}\right)^2 \Psi + \Psi e^{i\chi}\left(1 - |\Psi|^2\right) \quad \Big| : e^{i\chi}, \tag{2.12}$$

$$u(\frac{\partial \Psi}{\partial t} + i\varphi\Psi) = (\nabla - i\overrightarrow{A})^2\Psi + \Psi(1 - |\Psi|^2). \tag{2.13}$$

Therefore, the first TDGL equation is invariant under the gauge transformations. According to the transformations, we are free to choose function χ. Then, let $\chi = \int_0^t \varphi dt$. This is so-called "Zero electric potential gauge" (see [29]). It gives us the new electric potential $\varphi' = 0$ and removes the term φ' from the first TDGL equation:

$$u\frac{\partial \Psi}{\partial t} = \left(\nabla - i\overrightarrow{A}\right)^2 \Psi + \Psi\left(1 - |\Psi|^2\right). \tag{2.14}$$

The gauge invariant transformations for the second equation give:

$$k^2 \cdot \nabla \times \nabla \times \overrightarrow{A'} = -\sigma\left(\frac{\partial \overrightarrow{A'}}{\partial t} + \nabla\varphi'\right) + \frac{1}{2i}(\Psi'^*\nabla\Psi' - \Psi'\nabla\Psi'^*) - |\Psi'|^2\overrightarrow{A'}, \tag{2.15}$$

$$k^2 \cdot \nabla \times \nabla \times (\overrightarrow{A} + \nabla\chi) = -\sigma\left(\frac{\partial \overrightarrow{A}}{\partial t} + \frac{\partial}{\partial t}(\nabla\chi) + \nabla(\varphi - \frac{\partial \chi}{\partial t})\right) +$$
$$\frac{1}{2i}\left(\Psi^* e^{-i\chi}(\nabla\Psi e^{i\chi} + ie^{i\chi}\Psi\nabla\chi) - \Psi e^{i\chi}(\nabla\Psi^* e^{-i\chi} - ie^{-i\chi}\Psi^*\nabla\chi)\right) - |\Psi|^2(\overrightarrow{A} + \nabla\chi), \tag{2.16}$$

$$k^2 \cdot \nabla \times ([\nabla, \overrightarrow{A}] + \underbrace{[\nabla, \nabla\chi]}_{0}) = -\sigma\left(\frac{\partial \overrightarrow{A}}{\partial t} + \cancel{\nabla\frac{\partial \chi}{\partial t}} + \nabla\varphi - \cancel{\nabla\frac{\partial \chi}{\partial t}}\right) +$$
$$\frac{1}{2i}\left(\Psi^*\nabla\Psi + \underline{i|\Psi|^2\nabla\chi} - \Psi\nabla\Psi^* + \underline{i|\Psi|^2\nabla\chi}\right) - |\Psi|^2\overrightarrow{A} - |\Psi|^2\nabla\chi, \tag{2.17}$$

$$k^2 \cdot \nabla \times \nabla \times \overrightarrow{A} = -\sigma \left(\frac{\partial \overrightarrow{A}}{\partial t} + \nabla\varphi \right) + \frac{1}{2i}(\Psi^* \nabla\Psi - \Psi \nabla\Psi^*) + \cancel{|\Psi|^2 \nabla\chi} - |\Psi|^2 \overrightarrow{A} - \cancel{|\Psi|^2 \nabla\chi}, \quad (2.18)$$

$$k^2 \cdot \nabla \times \nabla \times \overrightarrow{A} = -\sigma \left(\frac{\partial \overrightarrow{A}}{\partial t} + \nabla\varphi \right) + \frac{1}{2i}(\Psi^* \nabla\Psi - \Psi \nabla\Psi^*) - |\Psi|^2 \overrightarrow{A}. \quad (2.19)$$

Using the "Zero electric potential gauge", the equation becomes as follows:

$$\overrightarrow{j_s} = \frac{1}{2i}(\Psi^* \nabla\Psi - \Psi \nabla\Psi^*) - |\Psi|^2 \overrightarrow{A}. \quad (2.20)$$

2.4 Link-variables

Link-variable method is used in order to provide fast convergence at high magnetic field [30]. Link-variables are as follows:

$$\begin{cases} U_x(x,y,z) = e^{-i\int_{x_0}^{x} A_x(\xi',y,z)d\xi'} \\ U_y(x,y,z) = e^{-i\int_{y_0}^{y} A_y(x,\xi',z)d\xi'} \end{cases} \text{ also } \begin{cases} U_x^*(x,y,z) = e^{i\int_{x_0}^{x} A_x(\xi',y,z)d\xi'} \\ U_y^*(x,y,z) = e^{i\int_{y_0}^{y} A_y(x,\xi',z)d\xi'}. \end{cases} \quad (2.21)$$

Their introduction at this point facilitates the preservation of gauge invariance under discretization. Their properties are as follows:

$$U_x U_x^* = 1; \begin{cases} \frac{\partial U_x}{\partial x} = -iA_x U_x \Big| \cdot U_x^* \\ + \\ \frac{\partial U_x^*}{\partial x} = iA_x U_x^* \Big| \cdot U_x \end{cases} <=> \begin{cases} A_x = \frac{1}{2i}(U_x \frac{\partial U_x^*}{\partial x} - U_x^* \frac{\partial U_x}{\partial x}) \\ or \\ iA_x = U_x \frac{\partial U_x^*}{\partial x} = -U_x^* \frac{\partial U_x}{\partial x}. \end{cases} \quad (2.22)$$

2.4.1 Link-variables in the first TDGL equation

Let us start with the term $(\nabla - i\overrightarrow{A})^2\Psi$. In terms of the link-variables it becomes as follows:

$$(\nabla - i\overrightarrow{A})^2\Psi = \nabla^2\Psi - i\nabla(\overrightarrow{A},\Psi) - i(\overrightarrow{A},\nabla\Psi) + (iA)^2\Psi = \wr \text{ projection on } \overrightarrow{e_x} \wr =$$
$$\frac{\partial^2\Psi}{\partial x^2}U_xU_x^* - i(\frac{\partial A_x}{\partial x}\Psi + \frac{\partial\Psi}{\partial x}A_x) - iA_x\frac{\partial\Psi}{\partial x} + (iA_x)^2\Psi =$$
$$\frac{\partial^2\Psi}{\partial x^2}U_xU_x^* - 2iA_x\frac{\partial\Psi}{\partial x} + \left((iA_x)^2\Psi - i\Psi\frac{\partial A_x}{\partial x}\right)U_xU_x^* =$$
$$U_x^*\left(U_x\frac{\partial^2\Psi}{\partial x^2} + 2\frac{\partial\Psi}{\partial x}\frac{\partial U_x}{\partial x} + \Psi((iA_x)^2 - i\frac{\partial A_x}{\partial x})U_x\right) =$$
$$U_x^*(U_x\frac{\partial^2\Psi}{\partial x^2} + 2\frac{\partial\Psi}{\partial x}\frac{\partial U_x}{\partial x} + \Psi\frac{\partial^2U_x^*}{\partial x^2}) = U_x^*\frac{\partial}{\partial x}(\frac{\partial\Psi}{\partial x}U_x + \frac{\partial U_x}{\partial x}\Psi) = U_x^*\frac{\partial^2(U_x\Psi)}{\partial x^2} =$$
$$\wr\ total \wr = \sum_{\mu=x,y} U_\mu^*\frac{\partial^2(U_\mu\Psi)}{\partial\mu^2} = U_x^*\frac{\partial^2(U_x\Psi)}{\partial x^2} + U_y^*\frac{\partial^2(U_y\Psi)}{\partial y^2}. \quad (2.23)$$

Then, the first TDGL equation becomes:

$$u\frac{\partial\Psi}{\partial t} = U_x^*\frac{\partial^2(U_x\Psi)}{\partial x^2} + U_y^*\frac{\partial^2(U_y\Psi)}{\partial y^2} + \Psi(1 - |\Psi|^2). \quad (2.24)$$

2.4.2 Link-variables in the superconducting current

The superconducting current is:

$$\overrightarrow{j_s} = \frac{1}{2i}(\Psi^*\nabla\Psi - \Psi\nabla\Psi^*) - |\Psi|^2\overrightarrow{A}. \quad (2.25)$$

It can be rewritten as follows:

$$\overrightarrow{j_s} = Im[\Psi^*(\nabla - i\overrightarrow{A})\Psi]. \quad (2.26)$$

or, using link-variables, its projection on the x-direction is:

$$j_{sx} = Im[\Psi^*(\frac{\partial\Psi}{\partial x} - iA_x\Psi)] = Im\left[\Psi^*U_x^*(U_x\frac{\partial\Psi}{\partial x} + \frac{\partial U_x}{\partial x}\Psi)\right] = Im\left[\Psi^*U_x^*\frac{\partial(U_x\Psi)}{\partial x}\right]. \quad (2.27)$$

Projection of $\overrightarrow{j_s}$ on $\overrightarrow{e_y}$ is:

$$j_{sy} = Im[\Psi^*(\frac{\partial\Psi}{\partial y} - iA_y\Psi)] = Im\left[\Psi^*U_y^*(U_y\frac{\partial\Psi}{\partial y} + \frac{\partial U_y}{\partial y}\Psi)\right] = Im\left[\Psi^*U_y^*\frac{\partial(U_y\Psi)}{\partial y}\right]. \quad (2.28)$$

2.5 Discrete model of the system and the algorithm of the calculation

For a superconductor with thickness $d < \lambda, \xi$ the distribution of the current and the corresponding vector potential can be assumed to be uniform in the z-direction. Then from the first GL equation, the same behavior follows for the order parameter, and, as far as the order parameter is concerned, the $3D$ problem is reduced to a 2-dimensional. We use this property of thin superconductors and average the Ginzburg-Landau equations over thickness of the superconductor [31].

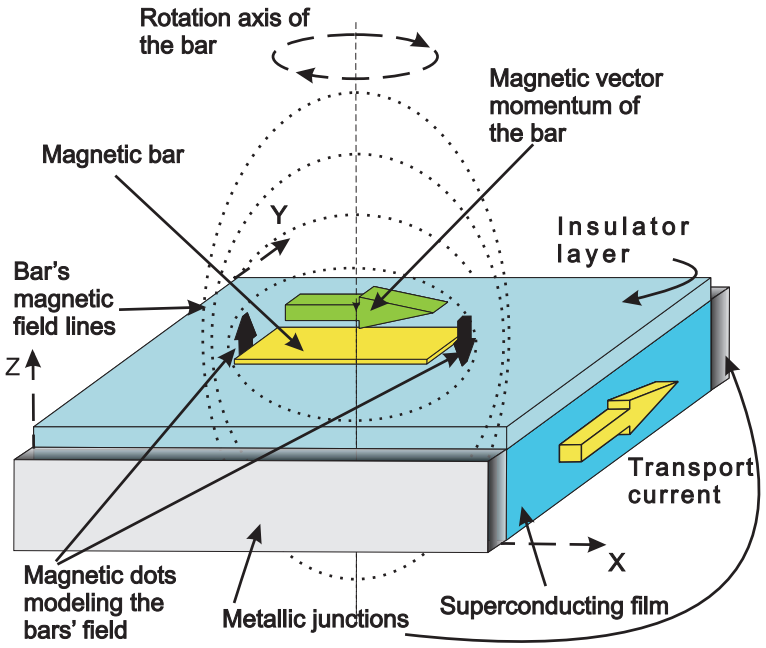

Figure 2.1: Model system. Thin-film rectangular-shaped superconductor with a magnetic bar on top, which is electrically isolated from the superconductor. The transport current is injected through the leads of a normal metal. Other two faces are surrounded by vacuum.

We simulate two-dimensional rectangular configurations (see Fig. 2.1) with $N+1$ ($i = \overline{0, N}$) grid points in the x-direction and $M+1$ ($j = \overline{0, M}$) grid points in the y-direction. Indexes i, j stand for running variables along the x- and y-direction, correspondingly. We choose equally spaced points ($\Delta x = \Delta y$) in space and time Δt. A finite-difference representation of the order parameter is chosen to be 0.5ξ. On average, the step in Δt is $\sim 10^{-3}\tau$, depending on the used grid as well as on a specific distribution of the order parameter. This value is aimed at minimization of the number of steps in Δt and, at the same time, keeps the procedure stable. Superconducting material occupying whole simulation region, except the bottom and the top boundary, is surrounded by a normal metal and Ψ is set to zero. Two other boundaries are surrounded by vacuum (or provide the periodic boundary condition, see Chapter 2.9).

The overview of the calculation scheme is shown in Fig. 2.2. Vertical dashed

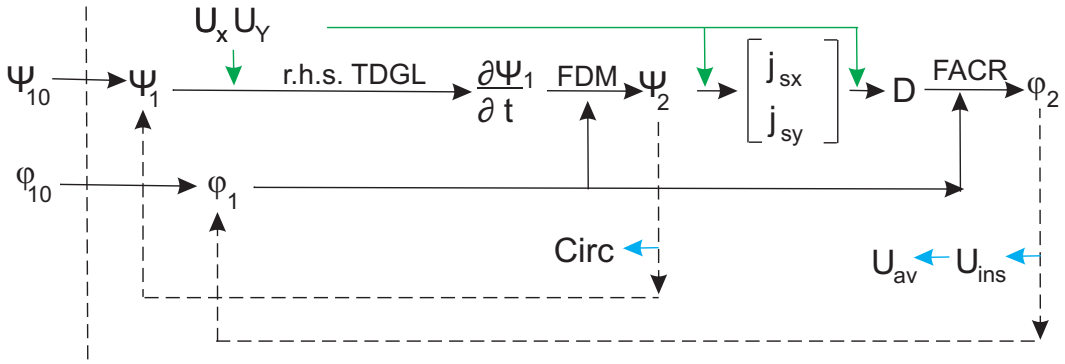

Figure 2.2: Algorithm of the numerical simulation. Ψ_{10}, φ_{10} - initial condition of the OP and electric potential correspondingly. Ψ_1, φ - instant values of the OP and the electric potential. U_x, U_y - link-variables. R.h.s. TDGL stands for right-hand-side of the first TDGL equation. FDM - finite difference method. Ψ_2 - instant value of the OP at the next time step. j_{sx} and j_{sy} - supercurrent along the x- and the y-axis respectively. D - divergence of the supercurrent. Dashed arrows symbolizes the recursive step of the simulation. FACR - Fourier analysis and Cyclic reduction methods. $Circ$ - subroutine for calculating the circulation of the OP phase over a contour. U_{ins} - instant value of the voltage between the leads. U_{av} - voltage between the leads averaged over the simulation time.

line separates the initial conditions of the OP, Ψ_{10}, and the electric potential, φ_{10}. Through the values of the Ψ_{10} and magnetic field we can initiate various initial conditions for the simulation, which correspond to zero-field-cooled (ZFC) or field-cooled (FC) regime. The magnetic field is assumed constant and converted to the link-variable arrays, U_x, U_y. These quantities allow us to obtain the value of the time derivative $\frac{\partial \Psi_1}{\partial t}$ at any point (i, j). In turn, it gives us the value of the OP, Ψ_2, which will be used during next iteration as Ψ_1. These values of Ψ we use to calculate the current densities j_{sx} and j_{sy} in every grid point. The link-variables and the new value of OP are used to find the distribution of the supercurrent in the system. The supercurrent, according to the Poisson equation, gives us the distribution of the electric potential φ_2. This is the last quantity, which is necessary to finalize the self-consistent calculation loop. This electric potential φ_2 is substituted back in the first TDGL equation as φ_1 and the whole procedure described above is repeated until we reach the end of the time period. The array of the $\Psi_{i,j}$ at each time iteration represents the solution of the TDGL equations.

For high-κ superconducting materials, or the thin films sample (smaller and comparable to the penetration depth λ, the demagnetization effect may be omitted from the simulation of the equilibrium superconducting state in an applied magnetic field. In other words, the contribution of the superconducting current to the total magnetic vector potential can be neglected.

Thus, we solve self-consistently two coupled GL equations for fixed magnetic field. Once a solution is obtained at a given magnetic field, the field is increased

(or decreased) and this solution is used as the initial value in the new calculation. In order to avoid a metastable state, we can follow the evolution of the Gibbs free energy of the system, which is $F(t) \sim \int |\Psi|^4 d\overrightarrow{r}$. If an obtained solution of TDGL corresponds to a local minimum on $F(t)$, then we omit the current one and search for another one. One of the possible solutions is to perform the same calculation for each magnetic field value, but without using the previously found state as input for the iteration scheme. For example, one can start from different initial conditions for the order parameter by setting $\Psi = 1$ or $\Psi \sim 0$ in every grid point. It corresponds ZFC or FC regime, respectively.

Through manipulation of the simulation time, transport current, magnetic field, etc., we can observe the dynamics of the order parameter under variety of conditions. E.g., the developing of vortices and antivortices, their current driven transport, their annihilation, and trapping on the pinning centers. Additionally, we can receive such "macro-data" as a vortex number (through the calculation of OP phase circulation over an arbitrary contour) in the contour, instant voltage in between the probes (reflecting the experiment signals, received with precision voltmeters), averaged voltage as integral characteristic for the IV-curve.

2.5.1 Discretization of the order parameter

In order to solve the TDGL equations numerically, we need to rewrite them in a discrete form. Then, the first TDGL equation:

$$\frac{\partial \Psi}{\partial t} = \frac{1}{u}\left[U_x^* \frac{\partial^2 (U_x \Psi)}{\partial x^2} + U_y^* \frac{\partial^2 (U_y \Psi)}{\partial y^2} + \Psi(1 - |\Psi|^2)\right]. \tag{2.29}$$

From the initial conditions we can find the right hand side (r.h.s. TDGL) of the equation:

$$\left.\frac{\partial \Psi}{\partial t}\right|_{i,j} = \frac{1}{u}\Bigg[\frac{U_{x\ i,j}\Psi_{i+1,j} - 2\Psi_{i,j} + \Psi_{i-1,j}/U_{x\ i,j}}{\triangle x^2} + \frac{U_{y\ i,j}\Psi_{i,j+1} - 2\Psi_{i,j} + \Psi_{i,j-1}/U_{y\ i,j}}{\triangle y^2} + \Psi_{i,j}(1 - |\Psi_{i,j}|^2)\Bigg]. \tag{2.30}$$

We can obtain the value of the time derivative ($\frac{\partial \Psi}{\partial t}$) in grid point (i, j). In the finite-difference method (FDM) it is given by:

$$\left.\frac{\partial \Psi}{\partial t}\right|_{i,j} = \frac{\Psi_{2i,j} - \Psi_{1i,j}}{\Delta t}. \tag{2.31}$$

Then the final value of the OP is given by:

$$\Psi_{2i,j} = \left[\Psi_{1i,j} + \triangle t \cdot \frac{\partial \Psi}{\partial t}\right] \cdot e^{-i\varphi_{i,j}\triangle t}. \tag{2.32}$$

The phase shift χ (which is the electric potential φ over $\triangle t$) for the next time step appeared due to the chosen gauge ($\Psi' = \Psi e^{i\chi}$). We use FTCS representation (forward time centered space) [32]. The FTCS representation is an explicit scheme.

These values of Ψ we use to calculate the current densities j_{sx} and j_{sy} in every grid point (see Fig. 2.2).

2.5.2 Discretization of the superconducting current

Writing the link-variables explicitly, we change expression for supercurrent in discrete variables:

$$j_{sx\ i,j} = Im\left(\Psi^*_{i,j}\frac{\Psi_{i+1,j}e^{-i\int_{x_i}^{x_{i+1}}A_x(\xi',y,z)d\xi'} - \Psi_{i-1,j}e^{i\int_{x_{i-1}}^{x_i}A_x(\xi',y,z)d\xi'}}{2\triangle x}\right) =$$
$$Im\left(\Psi^*_{i,j}\frac{\Psi_{i+1,j}e^{-iA_x(x,y,z)\triangle x} - \Psi_{i-1,j}e^{iA_x(x,y,z)\triangle x}}{2\triangle x}\right) =$$
$$Im\left(\Psi^*_{i,j}\frac{\Psi_{i+1,j}U_{x\ i,j} - \Psi_{i-1,j}U^*_{x\ i,j}}{2\triangle x}\right) =$$
$$Im\left(\Psi^*_{i,j}\frac{\Psi_{i+1,j}U_{x\ i,j} - \Psi_{i-1,j}/U_{x\ i,j}}{2\triangle x}\right). \quad (2.33)$$

In the previous equation we used the trapezium method:

$$\int_{x_i}^{x_{i+1}} A_x(\xi',y,z)d\xi' = A_x(x_i,y,z)\triangle x. \quad (2.34)$$

Projection of $\overrightarrow{j_s}$ on $\overrightarrow{e_y}$ is:

$$j_{sy} = Im\left[\Psi^* U^*_y \frac{\partial(U_y\Psi)}{\partial y}\right]. \quad (2.35)$$

By analogy, in terms of discrete variables we obtain:

$$j_{sy\ i,j} = Im\left(\Psi^*_{i,j}\frac{\Psi_{i,j+1}U_{y\ i,j} - \Psi_{i,j-1}/U_{y\ i,j}}{2\triangle y}\right). \quad (2.36)$$

It gives us the opportunity to calculate the divergence of the superconducting current as we mentioned in Fig. 2.2, and the electric potential as a further result.

2.5.3 Divergence of the superconducting current

The current conservation law $\overrightarrow{j_{total}} = \overrightarrow{j_s} + \overrightarrow{j_n}$ with $div\overrightarrow{j_{total}} = 0$ give altogether:

$$div(\overrightarrow{j_s} + \overrightarrow{j_n}) = 0 <=> div\overrightarrow{j_s} + div\overrightarrow{j_n} = 0 <=> div\overrightarrow{j_s} = -div\overrightarrow{j_n}. \quad (2.37)$$

but $\overrightarrow{j_n} = -\nabla\varphi$ and we have Poisson equation for the electric potential φ:

$$\nabla^2\varphi = div\overrightarrow{j_s}, \quad (2.38)$$

where

$$\begin{cases} div\overrightarrow{j_s} = \dfrac{\partial j_{sx}}{\partial x} + \dfrac{\partial j_{sy}}{\partial y} \\ \nabla^2\varphi = \dfrac{\partial^2\varphi}{\partial x^2} + \dfrac{\partial^2\varphi}{\partial y^2} \end{cases} <=> \frac{\partial^2\varphi}{\partial x^2} + \frac{\partial^2\varphi}{\partial y^2} = \frac{\partial j_{sx}}{\partial x} + \frac{\partial j_{sy}}{\partial y}. \tag{2.39}$$

Further, we modify this equation to the discrete form. The derivatives are as follows:

$$\frac{\partial^2\varphi}{\partial x^2} = \frac{\varphi_{i+1,j} - 2\varphi_{i,j} + \varphi_{i-1,j}}{\triangle x^2}, \tag{2.40}$$

$$\frac{\partial^2\varphi}{\partial y^2} = \frac{\varphi_{i,j+1} - 2\varphi_{i,j} + \varphi_{i,j-1}}{\triangle y^2}. \tag{2.41}$$

We denote that $div\overrightarrow{j_s}$ is D_{ij} in discrete form ($\frac{\partial j_{sx}}{\partial x} + \frac{\partial j_{sy}}{\partial y} \rightarrow D_{ij}$).
The equation for the electric potential φ in the discrete space becomes:

$$\frac{\varphi_{i+1,j} - 2\varphi_{i,j} + \varphi_{i-1,j}}{\triangle x^2} + \frac{\varphi_{i,j+1} - 2\varphi_{i,j} + \varphi_{i,j-1}}{\triangle y^2} = D_{ij}, \tag{2.42}$$

In this calculation we assume that $\triangle y = \triangle x$. This changes the previous equation:

$$\frac{1}{\triangle x^2}(\varphi_{i+1,j} - 2\varphi_{i,j} + \varphi_{i-1,j} + \varphi_{i,j+1} - 2\varphi_{i,j} + \varphi_{i,j-1}) = D_{i,j}, \tag{2.43}$$

$$\varphi_{i+1,j} - 4\varphi_{i,j} + \varphi_{i-1,j} + \varphi_{i,j+1} + \varphi_{i,j-1} = D_{i,j}\triangle x^2. \tag{2.44}$$

Then, we define divergence of the superconducting current through the *finite differences* of j_{sx} and j_{sy} on their grid (Fig. 2.3). It is written as follows:
In corners of the simulating area:

$$D_{0,0}\triangle x^2 = (\frac{j_{sx1,0} - j_{sx0,0}}{\triangle x} + \frac{j_{sy0,1} - j_{sy0,0}}{\triangle y})\triangle x^2 = \frac{j_{sx1,0} - j_{sy0,1}}{\triangle x}\triangle x^2. \tag{2.45}$$

$$D_{N,0}\triangle x^2 = (\frac{j_{sxN,0} - j_{sxN-1,0}}{\triangle x} + \frac{j_{syN,1} - j_{syN,0}}{\triangle y})\triangle x^2 = (j_{sxN-1,0} - j_{sxN,1})\triangle x. \tag{2.46}$$

$$D_{0,M}\triangle x^2 = (\frac{j_{sx1,M} - j_{sx0,M}}{\triangle x} + \frac{j_{sy0,M} - j_{sy0,M-1}}{\triangle y})\triangle x^2 = (j_{sx1,M} - j_{sx0,M-1})\triangle x. \tag{2.47}$$

$$D_{N,M}\triangle x^2 = (\frac{j_{sxN,M} - j_{sxN-1,M}}{\triangle x} + \frac{j_{syN,M} - j_{syN,M-1}}{\triangle y})\triangle x^2 = (-j_{sxN-1,M} - j_{sxN,M-1})\triangle x. \tag{2.48}$$

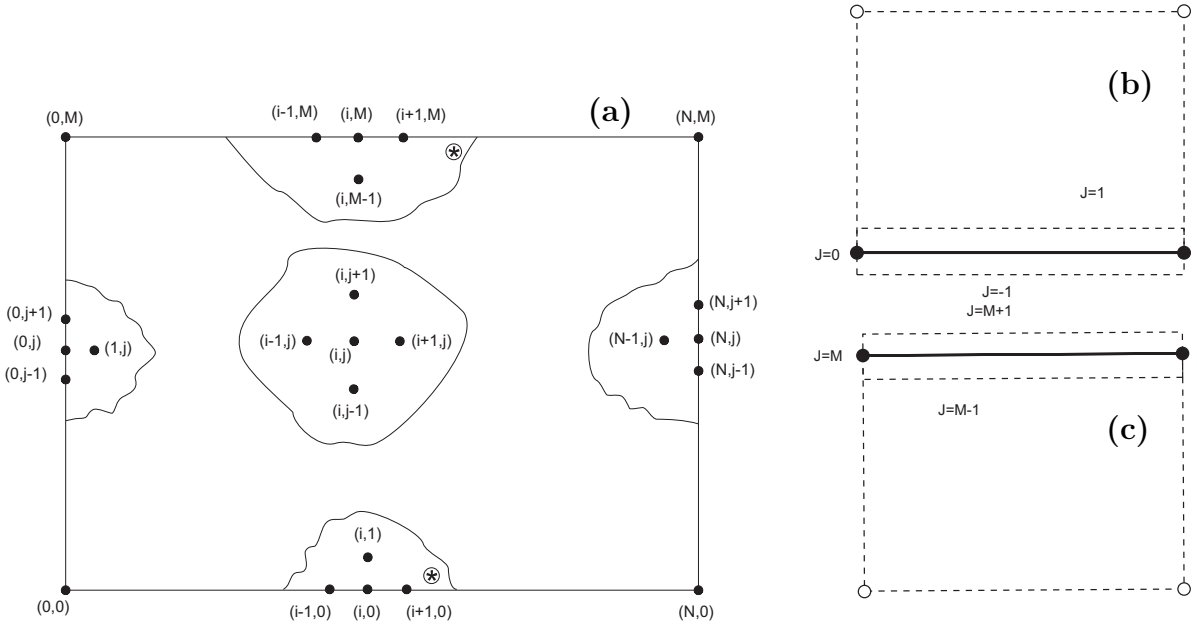

Figure 2.3: Grid points for calculation of the supercurrent divergence (a). Points with Cartesian coordinates (0,0), (0,M), (N,0), (N,M) define the corners of our rectangular system. Other points represent grid apexes/points for calculating divergence of the supercurrent within finite difference method. Areas with ⊛ sign are located near the metal lead and are subject to careful treatment (due to the introduction of the transport current). (b,c) - schematic view of the system, correspond to the bottom and the top boundary of the grid. It shows where the differential of the electric potential on the edges is substituted with the transport current multiplied over differential of the space ($\varphi_{i,1} - \varphi_{i,-1} = -j_{tr} \cdot (2\triangle x)$ and $\varphi_{i,M-1} - \varphi_{i,M+1} = j_{tr} \cdot (2\triangle x)$).

On edges of the simulating area (Fig. 2.3(a)):

$$D_{i,0}\triangle x^2 = (\frac{j_{sxi+1,0} - j_{sxi-1,0}}{2\triangle x} + \frac{j_{syi,1} - j_{syi,0}}{\triangle y})\triangle x^2 = (\frac{j_{sxi+1,0} - j_{sxi-1,0}}{2} - j_{syi,1})\triangle x. \quad (2.49)$$

$$D_{i,M}\triangle x^2 = (\frac{j_{sxi+1,M} - j_{sxi-1,M}}{2\triangle x} + \frac{j_{syi,M} - j_{syi,M-1}}{\triangle y})\triangle x^2 = (\frac{j_{sxi+1,M} - j_{sxi-1,M}}{2} - j_{syi,M-1})\triangle x. \quad (2.50)$$

$$D_{0,j}\triangle x^2 = (\frac{j_{sx1,j} - j_{sx0,j}}{\triangle x} + \frac{j_{sy0,j+1} - j_{sy0,j-1}}{2\triangle y})\triangle x^2 = (\frac{j_{sy1,j+1} - j_{sy0,j-1}}{2} + j_{sx1,j})\triangle x. \quad (2.51)$$

$$D_{N,j}\triangle x^2 = (\frac{j_{sxN,j} - j_{sxN-1,j}}{\triangle x} + \frac{j_{syN,j+1} - j_{syN,j-1}}{2\triangle y})\triangle x^2 = (\frac{j_{syN,j+1} - j_{syN,j-1}}{2} - j_{sxN-1,j})\triangle x. \quad (2.52)$$

Inside the stripe (Fig. 2.3(a)):

$$D_{i,j}\triangle x^2 = (j_{sxi+1,j} - j_{sxi-1,j} + j_{syi,j+1} - j_{syi,j-1})\frac{\triangle x}{2}. \quad (2.53)$$

Introduction of the transport current into equation for the electric potential

Consideration of the divergence near the metal leads, where the normal transport current flows, is a special topic (marked by the stars in the Fig. 2.3(a)). To clarify the idea, we show Figs. 2.3(b,c). A hypothetical $j = -1$ and $j = M + 1$ array of grid points is added. Although we do not know the electric potential on these grid points ($\varphi_{i,-1}$, $\varphi_{i,M+1}$), we need them to show that the derivative on the metal leads ($\varphi_{i,1} - \varphi_{i,-1} = -j_{tr} \cdot (2\triangle x)$ and $\varphi_{i,M-1} - \varphi_{i,M+1} = j_{tr} \cdot (2\triangle x)$) is equal to the transport current exactly.
1) $j = 0$ - the bottom edge (Fig. 2.3(c)):

$$\varphi_{i+1,j} - 4\varphi_{i,j} + \varphi_{i-1,j} + 2\varphi_{i,j+1} = D_{i,j}\triangle x^2 + (\varphi_{i,j+1} - \varphi_{i,j-1}), \quad (2.54)$$

$$\varphi_{i+1,j} - 4\varphi_{i,j} + \varphi_{i-1,j} + 2\varphi_{i,j+1} = D_{i,j}\triangle x^2 + \underbrace{\varphi'_{i,0}}_{-j_{tr}} \cdot 2\triangle x. \quad (2.55)$$

2) $j = M$ - the top edge (Fig. 2.3(b)):

$$\varphi_{i+1,j} - 4\varphi_{i,j} + \varphi_{i-1,j} + 2\varphi_{i,j+1} = D_{i,j}\triangle x^2 + (\varphi_{i,j-1} - \varphi_{i,j+1}), \quad (2.56)$$

$$\varphi_{i+1,j} - 4\varphi_{i,j} + \varphi_{i-1,j} + 2\varphi_{i,j+1} = D_{i,j}\triangle x^2 - \underbrace{\varphi'_{i,M}}_{-j_{tr}} \cdot 2\triangle x. \quad (2.57)$$

3) $0 < j < M$ - inside:

$$\varphi_{i+1,j} - 4\varphi_{i,j} + \varphi_{i-1,j} + \varphi_{i,j+1} + \varphi_{i,j-1} = D_{i,j}\triangle x^2. \quad (2.58)$$

2.6 Solving Poisson equation for the electric potential

2.6.1 Fourier analysis method (space transformation)

The idea of Fourier Analysis method is as follows. Instead of solving the equation in real space:

$$\varphi_{i+1,j} - 4\varphi_{i,j} + \varphi_{i-1,j} + \varphi_{i,j+1} + \varphi_{0,j-1} = D_{i,j} \quad (0 < i < N, 0 < j < M). \quad (2.59)$$

We transform it to the reciprocal space ($\varphi_{i,j} \longrightarrow \hat{\varphi}_{k_x,j}$):

$$[2\cos(\frac{\pi k_x}{N}) - 4]\hat{\varphi}_{k_x,j} + \hat{\varphi}_{k_x,j+1} + \hat{\varphi}_{k_x,j-1} = \hat{D}_{k_x,j} \quad (0 < k_x < N, 0 < j < M) \quad (2.60)$$

We solve it in this form and, then, transform the solution to the real space ($\hat{\varphi}_{k_x,j} \longrightarrow \varphi_{i,j}$). The Fourier method ($\varphi_{i,j} \longrightarrow \hat{\varphi}_{k_x,j}$) is used in order to improve the calculation speed (by reducing the number of variables from five to three). It is the fastest method for solving this problem.

The next step is finding the solution of the matrix equation for every k_x onward. This matrix is tridiagonal. When $k_x > 0$, we use Cycle Reduction method to diagonalize the matrix and find the solution $\hat{\varphi}_{k_x,j}$. Cycle Reduction method is another name for Gauss method (simple diagonalization of the matrix equation). When $k_x = 0$ the matrix equation does not have a solution (because two rows of the tridiagonal matrix are the same which make the matrix equation inconsistant). So, we introduce another Fourier transform for the variable y ($\hat{\varphi}_{k_x=0,j} \longrightarrow \hat{\varphi}_{0,k_y}$) and obtain its solution $\hat{\varphi}_{0,k_y}$ (2.6.3), then perform the reversal Fourier transformations for k_y ($\hat{\varphi}_{0,k_y} \longrightarrow \hat{\varphi}_{0,j}$). Then we perform the reversal Fourier transform ($\hat{\varphi}_{k_x,j} \longrightarrow \varphi_{i,j}$) and finally obtain $\varphi_{i,j}$ for real space. For more detail see [32].

Note: the phase φ is embedded in superconducting current j_s and divergence of the current, therefore, the formulas for their calculation will depend on the chosen boundary condition.
Boundary conditions can be of the following types:

- $\varphi_{i,j} = \varphi_{i+N,j}$ - periodic boundary condition (see 2.9);
- $\varphi_\Omega = 0$ - Dirihlet boundary condition;
- $\varphi'_\Omega = 0$ - Neumann boundary condition (see further).

Depending on the type of the boundary condition, the Fourier transformations for the electric potential are be different (e.g., components $cos(\frac{\pi k_x i}{N})$ or $exp(\frac{2\pi k_x i}{N})$).

Here we implement Neumann boundary conditions.

Substitutions $D_{i,j} \rightarrow \hat{D}_{k_x,j}$ and vice verse for Neumann boundary conditions are:

$$\hat{D}_{k_x,j} = \sum_{i=0}^{N}{}' D_{i,j} cos(\frac{\pi k_x i}{N}) \text{ - reciprocal space,} \tag{2.61}$$

$$D_{i,j} = \frac{2}{N} \sum_{k_x=0}^{N}{}' \hat{D}_{k_x,j} cos(\frac{\pi k_x i}{N}) \text{ - real space.} \tag{2.62}$$

The prime "′" means that the first (0) and the last (M) term are multiplied by $\frac{1}{2}$ (i.e. $\frac{D_{0,j}}{2}; \frac{D_{M,j}}{2}$).

The calculation of the electric potential ($\varphi_{i,j} \rightarrow \hat{\varphi}_{k_x,j}$):
For $j = 0$ (the bottom of the simulation area) we have:

$$\varphi_{i+1,0} - 4\varphi_{i,0} + \varphi_{i-1,0} + 2\varphi_{i,1} = D^*_{i,0}. \tag{2.63}$$

$$i = 0: \quad \varphi_{1,0} - 4\varphi_{0,0} + \varphi_{-1,0} + 2\varphi_{0,1} = D^*_{0,0} \quad \Big| \cdot \frac{1}{2}\cos(\frac{\pi k_x 0}{N}) \tag{2.64}$$

$$i = \overline{1, N-1}: \quad \varphi_{i+1,0} - 4\varphi_{i,0} + \varphi_{i-1,0} + 2\varphi_{i,1} = D^*_{i,0} \quad \Big| \cdot \cos(\frac{\pi k_x i}{N}) \tag{2.65}$$

$$i = N: \quad \varphi_{N+1,0} - 4\varphi_{N,0} + \varphi_{N-1,0} + 2\varphi_{N,1} = D^*_{N,0} \quad \Big| \cdot \frac{1}{2}\cos(\frac{\pi k_x N}{N}) \tag{2.66}$$

Adding these equations, we have:

$$\sum_{i=0}^{N}{}' \varphi_{i+1,0}\cos(\frac{\pi k_x i}{N}) + \sum_{i=0}^{N}{}' \varphi_{i-1,0}\cos(\frac{\pi k_x i}{N}) - 4\hat{\varphi}_{k_x,0} + 2\hat{\varphi}_{k_x,1} = \hat{D}^*_{k_x,0}. \tag{2.67}$$

For $j = \overline{1, M-1}$ (the internal part of the simulation area) we have::

$$\varphi_{i+1,j} - 4\varphi_{i,j} + \varphi_{i-1,j} + \varphi_{i,j+1} + \varphi_{i,j-1} = D_{i,j} \tag{2.68}$$

$$i = 0: \quad \varphi_{1,j} - 4\varphi_{0,j} + \varphi_{-1,j} + \varphi_{0,j-1} + \varphi_{0,j+1} = D_{0,j} \quad \Big| \cdot \frac{1}{2}\cos(\frac{\pi k_x 0}{N}) \tag{2.69}$$

$$i = \overline{1, N-1}: \quad \varphi_{i+1,j} - 4\varphi_{i,j} + \varphi_{i-1,j} + \varphi_{i,j+1} + \varphi_{0,j-1} = D_{i,j} \quad \Big| \cdot \cos(\frac{\pi k_x i}{N}) \tag{2.70}$$

$$i = N: \quad \varphi_{N+1,j} - 4\varphi_{N,j} + \varphi_{N-1,j} + \varphi_{N,j+1} + \varphi_{0,j-1} = D_{N,j} \quad \Big| \cdot \frac{1}{2}\cos(\frac{\pi k_x N}{N}) \quad (2.71)$$

Adding these equations, we have:

$$\sum_{i=0}^{N\,'} \varphi_{i+1,j}\cos(\frac{\pi k_x i}{N}) + \sum_{i=0}^{N\,'} \varphi_{i-1,j}\cos(\frac{\pi k_x i}{N}) - 4\hat{\varphi}_{k_x,j} + \hat{\varphi}_{k_x,j-1} + \hat{\varphi}_{k_x,j+1} = \hat{D}_{k_x,j} \quad (2.72)$$

For $j = M$ (the top of the simulation area) :

$$\varphi_{i+1,M} - 4\varphi_{i,M} + \varphi_{i-1,M} + 2\varphi_{i,M-1} = D^*_{i,M}. \quad (2.73)$$

$$i = 0: \quad \varphi_{1,M} - 4\varphi_{0,M} + \varphi_{-1,M} + 2\varphi_{0,M-1} = D^*_{0,M} \quad \Big| \cdot \frac{1}{2}\cos(\frac{\pi k_x 0}{N}) \quad (2.74)$$

$$i = \overline{1, N-1}: \quad \varphi_{i+1,M} - 4\varphi_{i,M} + \varphi_{i-1,M} + 2\varphi_{i,M-1} = D^*_{i,M} \quad \Big| \cdot \cos(\frac{\pi k_x i}{N}) \quad (2.75)$$

$$i = N: \quad \varphi_{N+1,M} - 4\varphi_{N,M} + \varphi_{N-1,M} + 2\varphi_{N,M-1} = D^*_{N,M} \quad \Big| \cdot \frac{1}{2}\cos(\frac{\pi k_x N}{N}) \quad (2.76)$$

Adding these equations altogether, we have:

$$\sum_{i=0}^{N\,'} \varphi_{i+1,M}\cos(\frac{\pi k_x i}{N}) + \sum_{i=0}^{N\,'} \varphi_{i-1,M}\cos(\frac{\pi k_x i}{N}) - 4\hat{\varphi}_{k_x,} + 2\hat{\varphi}_{k_x,M-1} = \hat{D}^*_{k_x,M} \quad (2.77)$$

The common term in the equations 2.67, 2.72 and 2.77 is: (substitute index $i \pm 1 \longrightarrow k$):

$$\sum_{i=0}^{N\,'} \varphi_{i+1,j}\cos(\frac{\pi k_x i}{N}) + \sum_{i=0}^{N\,'} \varphi_{i-1,j}\cos(\frac{\pi k_x i}{N}) = \quad (2.78)$$

$$= \hat{\varphi}_{k_x,j} + \frac{1}{2}(\varphi_{-1,j} - \varphi_{1,j}) + \frac{1}{2}\cos(\pi k_x N)(\varphi_{N+1,j} - \varphi_{N-1,j}) \quad (2.79)$$

The boundary conditions are: $\frac{\partial\varphi}{\partial x}\Big|_{x=0} = 0$ and $\frac{\partial\varphi}{\partial x}\Big|_{x=N} = 0$.

Therefore: $\varphi_{-1,j} - \varphi_{1,j} = 0$ and $\varphi_{N+1,j} - \varphi_{N-1,j} = 0$.
Then

$$\sum_{i=0}^{N\,'} \varphi_{i+1,j}\cos(\frac{\pi k_x i}{N}) + \sum_{i=0}^{N\,'} \varphi_{i-1,j}\cos(\frac{\pi k_x i}{N}) = 2\cos(\frac{\pi k_x}{N})\hat{\varphi}_{k_x,j}. \quad (2.80)$$

Equations for the electric potential in the reciprocal space become:

$$[2\cos(\frac{\pi k_x}{N}) - 4]\hat{\varphi}_{k_x,0} + 2\hat{\varphi}_{k_x,1} = \hat{D}^*_{k_x,0};\ k_y = 0 \tag{2.81}$$

$$[2\cos(\frac{\pi k_x}{N}) - 4]\hat{\varphi}_{k_x,j} + \hat{\varphi}_{k_x,j+1} + \hat{\varphi}_{k_x,j-1} = \hat{D}_{k_x,j};\ 0 < k_y < M \tag{2.82}$$

$$[2\cos(\frac{\pi k_x}{N}) - 4]\hat{\varphi}_{k_x,M} + 2\hat{\varphi}_{k_x,M-1} = \hat{D}^*_{k_x,M};\ k_y = M \tag{2.83}$$

In the matrix form:

$$\hat{C} \cdot \overrightarrow{\hat{\varphi}} = \overrightarrow{\hat{D}}, \tag{2.84}$$

$$\begin{pmatrix} 2\cos(\frac{\pi k_x}{N}) - 4 & 2 & 0 & 0 & \dots & 0 & 0 \\ 1 & 2\cos(\frac{\pi k_x}{N}) - 4 & 1 & 0 & \dots & 0 & 0 \\ 0 & 1 & 2\cos(\frac{\pi k_x}{N}) - 4 & 1 & \dots & 0 & 0 \\ \dots & \dots & \dots & \dots & \dots & \dots & \dots \\ 0 & 0 & 0 & 0 & \dots & 2 & 2\cos(\frac{\pi k_x}{N}) - 4 \end{pmatrix} \times \begin{pmatrix} \hat{\varphi}_{k_x,0} \\ \hat{\varphi}_{k_x,1} \\ \hat{\varphi}_{k_x,2} \\ \dots \\ \hat{\varphi}_{k_x,M} \end{pmatrix} = \begin{pmatrix} \hat{D}^*_{k_x,0} \\ \hat{D}_{k_x,1} \\ \hat{D}_{k_x,2} \\ \dots \\ \hat{D}^*_{k_x,M} \end{pmatrix}. \tag{2.85}$$

2.6.2 Cycle reduction method (matrix diagonalization)

Matrix $\hat{C}$ in the previous paragraph is of $M \times M$ size. Firstly, we simplify matrix equation by dividing every first row matrix element and the array element $\hat{D}_{k_x,1}$ by $2\cos(\frac{\pi k_x}{N}) - 4$. Then we subtract the second row from the first one and update the second row with new values. This procedure we repeat for every row of the matrix equation. In the end, we have this square matrix diagonalized for $1 \leq k_x \leq N$:
In this way, we diagonalized the matrix to the form:

$$\begin{pmatrix} 1 & P_0 & 0 & 0 & \dots & 0 \\ 0 & 1 & P_1 & 0 & \dots & 0 \\ 0 & 0 & 1 & P_2 & \dots & 0 \\ \dots & \dots & \dots & \dots & \dots & \dots \\ 0 & 0 & 0 & 0 & \dots & 1 \end{pmatrix} \cdot \begin{pmatrix} \hat{\varphi}_{k_x,0} \\ \hat{\varphi}_{k_x,1} \\ \hat{\varphi}_{k_x,2} \\ \dots \\ \hat{\varphi}_{k_x,M} \end{pmatrix} = \begin{pmatrix} Q_0 \\ Q_1 \\ Q_2 \\ \dots \\ Q_M \end{pmatrix}, \tag{2.86}$$

where

$$P_0 = \frac{2}{2\cos(\frac{\pi k_x}{N}) - 4} \text{ and } Q_0 = \frac{\hat{D}^*_{k_x,0}}{2\cos(\frac{\pi k_x}{N}) - 4}, \tag{2.87}$$

$$P_j = \frac{1}{2\cos(\frac{\pi k_x}{N}) - 4 - P_{j-1}} \text{ and } Q_j = \frac{\hat{D}_{k_x,j} - Q_{j-1}}{2\cos(\frac{\pi k_x}{N}) - 4 - P_{j-1}}. \tag{2.88}$$

The "reversal steps" (calculation of the $\hat{\varphi}_{k_x,j}$) are as follows:

$$\hat{\varphi}_{k_x,M} = Q_M, \tag{2.89}$$

$$\hat{\varphi}_{k_x,j} = Q_j - P_j\hat{\varphi}_{k_x,j+1} \text{ for } 0 \leq j \leq M-1. \tag{2.90}$$

We repeat this procedure for $1 \leq k_x \leq N$.

2.6.3 Special case treatment

For $k_x = 0$ it is impossible to solve the equations (division by zero) by diagonalization (Cycle Reduction) method (as two rows are unresolved). In order to find out $\hat{\varphi}_{k_x=0,j}$, one needs to use Fourier method again.

$$-2\hat{\varphi}_{0,0} + 2\hat{\varphi}_{0,1} = \hat{D}^*_{0,0};\ j = 0 \tag{2.91}$$

$$-2\hat{\varphi}_{0,j} + \hat{\varphi}_{0,j+1} + \hat{\varphi}_{0,j-1} = \hat{D}_{0,j};\ 0 < j < M \tag{2.92}$$

$$-2\hat{\varphi}_{0,M} + 2\hat{\varphi}_{0,M-1} = \hat{D}^*_{0,M};\ j = M \tag{2.93}$$

We substitute $j \to k_y$:

$$j = 0: \quad -2\hat{\varphi}_{0,0} + 2\hat{\varphi}_{0,1} = \hat{D}^*_{0,0} \quad \Big| \cdot \frac{1}{2}\cos(\frac{\pi k_y 0}{M}) \tag{2.94}$$

$$0 < j < M: \quad -2\hat{\varphi}_{0,j} + \hat{\varphi}_{0,j+1} + \hat{\varphi}_{0,j-1} = \hat{D}_{0,j} \quad \Big| \cdot \cos(\frac{\pi k_y j}{M}) \tag{2.95}$$

$$j = M: \quad -2\hat{\varphi}_{0,M} + 2\hat{\varphi}_{0,M-1} = \hat{D}^*_{0,M} \quad \Big| \cdot \frac{1}{2}\cos(\frac{\pi k_y M}{M}) \tag{2.96}$$

Adding these equations, we have:

$$\underbrace{2\frac{1}{2}\hat{\varphi}_{0,1}cos(\frac{\pi k_y 0}{M}) + \sum_{j=1}^{M-1}(\hat{\varphi}_{0,j+1} + \hat{\varphi}_{0,j-1})\cos(\frac{\pi k_y j}{M}) + 2\frac{1}{2}\hat{\varphi}_{0,M-1}\cos(\frac{\pi k_y M}{M}) -}_{2\cos(\frac{\pi k_y}{M})\hat{\varphi}_{0,k_y}}$$

$$2\hat{\varphi}_{0,k_y} = \hat{D}_{0,k_y}. \tag{2.97}$$

Using the substitutions:
$i \longrightarrow j$,
$N \longrightarrow M$,
$j \longrightarrow 0$,
$k_x \longrightarrow k_y$,

we obtain:

$$-2\hat{\varphi}_{0,k_y} + 2\cos(\frac{\pi k_y}{M})\hat{\varphi}_{0,k_y} = \hat{D}_{0,k_y}, \tag{2.98}$$

where

$$\hat{D}_{k_x=0,k_y} = \sum_{j=0}^{M}{}' \underbrace{\left[\sum_{i=0}^{N}{}' \hat{D}_{i,j}\cos(\frac{\pi 0 i}{N})\right]}_{P_0} \cos(\frac{\pi k_y j}{M}) \text{ - reversal space} \tag{2.99}$$

The equation takes the form:

$$\hat{\varphi}_{k_x=0,k_y}\left[2\cos(\frac{\pi k_y}{M}) - 2\right] = \hat{D}_{k_x=0,k_y}. \tag{2.100}$$

The solution is:

$$\hat{\varphi}_{0,k_y} = \frac{D_{0,k_y}}{2\cos(\frac{\pi k_y}{M}) - 2} \text{ for } k_y = \overline{1, M}. \tag{2.101}$$

For Neumann boundary conditions, we can define the solution with precision up to an additive constant. We assume that this constant $\hat{\varphi}_{0,0} = \frac{\hat{D_{0,0}}}{0}$ is equal to zero: $\hat{\varphi}_{0,0} = 0$.
The reversal Fourier transformation over k_y is as follows:

$$\underbrace{\hat{\varphi}_{0,j}}_{\hat{\varphi}_{k_x=0,j}} = \frac{2}{M}\sum_{k_y=0}^{M}{}' \hat{\varphi}_{0,k_y}\cos(\frac{\pi k_y j}{M}). \tag{2.102}$$

In the program it appears as:

$$\hat{\varphi}_{0,j} = \frac{2}{M}\left[\underbrace{\frac{1}{2}\hat{\varphi}_{0,0}cos(\frac{\pi 0 j}{M})}_{\hat{\varphi}_{0,0}=0} + \sum_{k_y=1}^{M-1}\hat{\varphi}_{0,k_y}cos(\frac{\pi k_y j}{M}) + \frac{1}{2}\frac{\hat{\varphi}_{0,M}}{-4}cos(\frac{\pi M j}{M})\right]. \tag{2.103}$$

The reversal Fourier transformation over k_x is:

$$\varphi_{i,j} = \frac{2}{N}\sum_{k_x=0}^{N}{}' \hat{\varphi}_{k_x,j}\cos(\frac{\pi k_x i}{N}). \tag{2.104}$$

After calculating the phase, we can calculate the order parameter at the next time-step (the recursion).

2.7 Additional quantities: Instant voltage, average voltage, normal current and vorticity

Beside the distribution of $\Psi(x, y)$, we can analyze additional quantities (see Fig. 2.2):

- instant voltage between the probes (averaged over the stripe width):

$$U_{inst} = \frac{1}{N+1}\sum_{j=0}^{N}\varphi_{i,j}. \tag{2.105}$$

This parameter corresponds to an experimentally observed characteristic.

- average voltage (averaged over evolution time):

$$U_{av} = \frac{1}{n}\sum_{t=0}^{n}U_{inst}, \tag{2.106}$$

where n is the number of the time steps in the system evolving time. This parameter corresponds to the average voltage, which is induced by the constant flux motion in the system.

- space distribution of the normal current ($\overrightarrow{j_n} = \sigma\overrightarrow{E} = -\sigma\nabla\varphi$):

$$j_{nx} = -\frac{\varphi_{i+1,j} - \varphi_{i-1,j}}{2\triangle x} \text{ - along the } x\text{-axis}, \tag{2.107}$$

$$j_{ny} = -\frac{\varphi_{i,j+1} - \varphi_{i,j-1}}{2\triangle x} \text{ - along the } y\text{-axis}. \tag{2.108}$$

It shows the conversion between the super and normal current in the intermediate region.

- phase of the OP:

This parameter corresponds to the imaginary part of the OP and is essential to define the vorticity of the vortex. To determine which minima correspond to vortices and which to antivortices it is convenient to look at the phase of the order parameter, as its gradient gives the direction of the supercurrent.

$$\theta = arctg\left(\frac{Im(\Psi)}{Re(\Psi)}\right). \tag{2.109}$$

- vorticity (circulation of the OP phase over a contour):

$$\frac{d\Psi}{dx} = \frac{d}{dx}(\Psi e^{i\theta}) = e^{i\theta}\frac{\partial\Psi}{\partial x} + i\Psi e^{i\theta}\frac{\partial\theta}{\partial x}\Bigg| \cdot \Psi^*, \tag{2.110}$$

$$Im(\Psi^*\frac{d\Psi}{dx}) = |\Psi|^2\frac{\partial\theta}{\partial x}, \tag{2.111}$$

$$\frac{\partial\theta}{\partial x} = \frac{Im(\Psi^*\frac{d\Psi}{dx})}{|\Psi|^2}. \tag{2.112}$$

Circulation of the OP phase over a contour gives us a number of vortices inside the contour. This parameter is more convenient for observing the total number of vortices in the stripe and resource-efficient for saving this data, than the phase of the order parameter.

2.8 Vector potential of homogeneous magnetic field and magnetic dipole

Vector potential of the external homogeneous magnetic field (along the z-axis) in symmetrical gauge:

$$\overrightarrow{A_B} = \frac{1}{2}[\overrightarrow{B}, \overrightarrow{r}] = \frac{1}{2}\begin{vmatrix} \overrightarrow{i} & \overrightarrow{j} & \overrightarrow{k} \\ 0 & 0 & B_z \\ x & y & z \end{vmatrix} = \underbrace{\overrightarrow{i}\,(-\frac{B_z y}{2})}_{A_x} + \underbrace{\overrightarrow{j}\,\frac{B_z x}{2}}_{A_y} + \underbrace{\overrightarrow{k}\,0}_{A_z}. \tag{2.113}$$

The Landau gauge of the vector potential:

$$\overrightarrow{A_H} = \underbrace{\overrightarrow{i}\,(-yB_z)}_{A_x} + \underbrace{\overrightarrow{j}\,0}_{A_y} + \underbrace{\overrightarrow{k}\,0}_{A_z}. \tag{2.114}$$

This gauge is suitable for periodic boundary condition for the infinite stripe in x-direction, as it conserves the values of the vector potential. For the finite stripe the type of the gauge does not play a crucial role. Another gauge of the vector potential:

$$\overrightarrow{A_H} = \underbrace{\overrightarrow{i}\,0}_{A_x} + \underbrace{\overrightarrow{j}\,xB_z}_{A_y} + \underbrace{\overrightarrow{k}\,0}_{A_z}. \tag{2.115}$$

Vector potential of the out-of-plane magnetic dipole (along the z-axis):

$$\overrightarrow{A_\mu} = \frac{[\overrightarrow{\mu_z}, \overrightarrow{r}]}{r^3} = \frac{1}{r^3}\begin{vmatrix} \overrightarrow{i} & \overrightarrow{j} & \overrightarrow{k} \\ 0 & 0 & \mu_z \\ x & y & z \end{vmatrix} = \underbrace{\overrightarrow{i}\,(-\frac{\mu_z y}{r^3})}_{A_x} + \underbrace{\overrightarrow{j}\,\frac{\mu_z x}{r^3}}_{A_y} + \underbrace{\overrightarrow{k}\,0}_{A_y}. \tag{2.116}$$

2.9 Periodic boundary conditions for the infinite stripe in the x-direction

If we assume the periodic boundary condition along the x-axis, then all the quantities should obey the following equivalences:

$$\Psi(x, y) = \Psi(x + N, y), \tag{2.117}$$

$$\varphi(x, y) = \varphi(x + N, y), \tag{2.118}$$

$$\overrightarrow{j_s}(x, y) = \overrightarrow{j_s}(x + N, y), \tag{2.119}$$

$$\overrightarrow{A}(x, y) = \overrightarrow{A}(x + N, y). \tag{2.120}$$

Although the criteria for the OP is easy to implement, the situation is more complicated with other quantities.

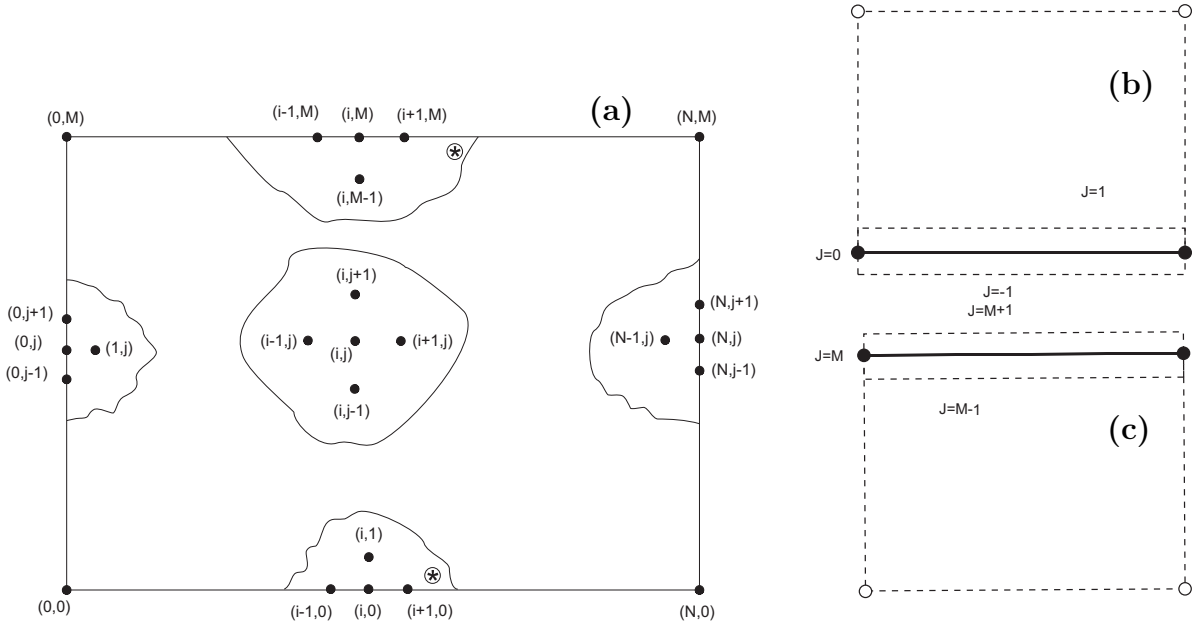

Figure 2.4: Grid points for calculation of the supercurrent divergence (a). Points with Cartesian coordinates (0,0), (0,M), (N,0), (N,M) define the corners of our rectangular system. Other points represent grid apexes/points for calculating divergence of the supercurrent within finite difference method. Areas with ⊛ sign are located near the metal lead and are subject to careful treatment (due to the introduction of the transport current). (b,c) - schematic view of the system, correspond to the bottom and the top boundary of the grid. It shows where the differential of the electric potential on the edges is substituted with the transport current multiplied over differential of the space ($\varphi_{i,1} - \varphi_{i,-1} = -j_{tr} \cdot (2\triangle x)$ and $\varphi_{i,M-1} - \varphi_{i,M+1} = j_{tr} \cdot (2\triangle x)$).

2.9.1 Divergence of the superconducting current and the electric potential

In the case of infinite superconducting films, periodic boundary conditions around the simulation region should be used. However, standard periodicity may be used only if the applied vector potential is periodic itself. In general case, periodic boundary conditions for $\overrightarrow{A}$ and Ψ have the form [43]

$$\overrightarrow{A}(\overrightarrow{\rho} + \overrightarrow{b}_i) = \overrightarrow{A}(\overrightarrow{\rho}) + \overrightarrow{\nabla}\eta_i(\overrightarrow{\rho}), \tag{2.121}$$

$$\Psi(\overrightarrow{\rho} + \overrightarrow{b}_i) = \Psi exp(2\pi\eta_i(\overrightarrow{\rho})/\Phi_0), \tag{2.122}$$

where $\overrightarrow{b_i}$, $i = x, y$ are the lattice vectors, and η_i is the gauge potential which cannot be chosen freely but must preserve the single valuedness of $\overrightarrow{A}$ and Ψ. These boundary conditions mean that $\overrightarrow{A}$, Ψ are invariant under lattice translations combined with specific gauge transformations. Other quantities, such as the magnetic field, the current and the order parameter density are periodic.

The divergence is written as follows:

$$D_{i,j} = \frac{\partial j_{sx}}{\partial x} + \frac{\partial j_{sy}}{\partial y}. \tag{2.123}$$

$$D_{0,0}\triangle x^2 = (\frac{j_{sx1,0} - j_{sxN-1,0}}{2\triangle x} + \frac{j_{sy0,1} - j_{sy0,0}}{\triangle y})\triangle x^2 = \left(\frac{j_{sx1,0} - j_{sxN-1,0}}{2} + j_{sy0,1}\right)\triangle x. \tag{2.124}$$

$$D_{N,0}\triangle x^2 = (\frac{j_{sxN+1,0} - j_{sxN-1,0}}{2\triangle x} + \frac{j_{syN,1} - j_{syN,0}}{\triangle y})\triangle x^2 = \left(\frac{j_{sx1,0} - j_{sxN-1,0}}{2} + j_{syN,1}\right)\triangle x. \tag{2.125}$$

(because of periodicity $j_{sxN+1,0} = j_{sx1,0}$)

$$D_{0,M}\triangle x^2 = (\frac{j_{sx1,M} - j_{sxN-1,M}}{2\triangle x} + \frac{j_{sy0,M} - j_{sy0,M-1}}{\triangle y})\triangle x^2 = \left(\frac{j_{sx1,M} - j_{sxN-1,M}}{2} - j_{sy0,M-1}\right)\triangle x. \tag{2.126}$$

$$D_{N,M}\triangle x^2 = (\frac{j_{sxN+1,M} - j_{sxN-1,M}}{2\triangle x} + \frac{j_{syN,M} - j_{syN,M-1}}{\triangle y})\triangle x^2 = \left(\frac{j_{sx1,M} - j_{sxN-1,M}}{2} - j_{syN,M-1}\right)\triangle x. \tag{2.127}$$

On the edges:

$$D_{0,j}\triangle x^2 = (\frac{j_{sx1,j} - j_{sxN-1,j}}{2\triangle x} + \frac{j_{sy0,j+1} - j_{sy0,j-1}}{2\triangle y})\triangle x^2 = \\ (j_{sx1,j} - j_{sxN-1,j} + j_{sy0,j+1} - j_{sy0,j-1})\,\frac{\triangle x}{2}. \quad (2.128)$$

$$D_{N,j}\triangle x^2 = (\frac{j_{sxN+1,j} - j_{sxN-1,j}}{2\triangle x} + \frac{j_{syN,j+1} - j_{syN,j-1}}{2\triangle y})\triangle x^2 = \\ (j_{sx1,j} - j_{sxN-1,j} + j_{syN,j+1} - j_{syN,j-1})\,\frac{\triangle x}{2}. \quad (2.129)$$

For the electric potential, everywhere in the 2.6.1 $i \longrightarrow k_x$ Fourier transform the argument $\frac{\pi k_x i}{N}$ is to be substituted for $\frac{2\pi\tilde{i}k_x i}{N}$.

$$\hat{D}_{k_x,j} = \sum_{i=0}^{N-1} D_{i,j} e^{\frac{2\pi\tilde{i}k_x i}{N}} \text{ - real space;} \quad (2.130)$$

$$D_{i,j} = \frac{1}{N}\sum_{k_x=0}^{N-1} \hat{D}_{k_x,j} e^{\frac{2\pi\tilde{i}k_x i}{N}} \text{ - reversal space,} \quad (2.131)$$

where $\tilde{i} = \sqrt{-1}$.

Following the procedure have been described above, one can obtain the solution for $\varphi_{i,j}$ within periodic boundary condition.

Chapter 3

The guidance of vortex-antivortex pairs by in-plane magnetic dipoles in a superconducting finite-size film

The possibility of manipulating vortex matter by using various artificial pinning arrays is of significant importance for possible applications in fluxonics nano- and micro-devices. By numerically solving the time-dependent Ginzburg-Landau equations, we study the vortex-antivortex (v-av) dynamics in a hybrid structure consisting of a finite size superconductor with magnetic dipoles on top which generate v-av pairs in the presence of an external current. The v-av dynamics is analyzed for different arrangements and magnetic moments of the dipoles, as a function of angle α between the direction of the magnetic dipole and that of the Lorentz force produced by the applied current. The interplay of the attractive interaction between a v-av pair and the Lorentz force leads either to the separation of (anti)vortices and their motion in opposite directions or to their annihilation. We found a critical angle α_c, below which vortices and antivortices are repelled, while for larger angles they annihilate. In case of a single (few) magnetic dipole(s), this magnetic-dipole-induced v-av guidance is influenced by the self-interaction of the v-av pairs with their images in a finite-size sample, while for a periodic array of dipoles the guidance is determined by the interaction of a v-av pair with other dipoles and v-av pairs created by them. This effect is tunable through the external current and the magnetization and size of the magnetic dipoles.

The results presented in this chapter have been published in Ref. [33].

3.1 Introduction

It is well known that in "dirty" superconductors Abrikosov vortices move in the direction perpendicular to the direction of the local current $\mathbf{j}$ under the action of the Lorentz force produced by the external current $\mathbf{F}_L = \frac{\Phi_0}{c}[\mathbf{j} \times \overrightarrow{e_B}]$ [16, 34], where $\overrightarrow{e_B}$ indicates the direction of the magnetic field of the vortex. In a homogenous superconductor in the presence of a homogenous external magnetic field the

direction of the vortex motion in the superconductor is well defined and it is perpendicular to both the external current and the applied magnetic field. In case of zero magnetic field, the vortex-antivortex (v-av) pairs will be created by the current induced magnetic field, nucleate at the edges of the sample and annihilate somewhere deep in the superconductor. In this case their trajectories will be straight lines, connecting the v-av nucleation points at the opposite edges of the sample.

The situation will change if inhomogeneities are present in the superconductor. They can be either of intrinsic nature (e.g., defects of the structure, twin boundaries, etc.) or artificially created arrays of antidots (holes) [35, 36, 37, 38, 39, 40, 41], blind holes [42, 43], or arrays of magnetic particles [44, 45, 46, 47, 48, 49, 50, 51, 52, 53, 54, 55]. In those systems the distribution of the current density in the superconductor is rather inhomogenous and vortex trajectories — which are determined by the current density distribution as well as by the interaction with the complex potential-energy landscape created by the defects and by the interaction with other vortices, — may have very complicated shape. This opens the way to manipulate the vortex motion, the so-called *vortex guidance* which was first demonstrated experimentally by Wördenweber *et al.* [39] using high-T_c $YBa_2Cu_3O_7$ films with special arrangements of antidots. Resistive Hall-type measurements revealed the presence of guided flux motion along rows of antidots.

In this paper we study flux guidance in a different system, i.e., a hybrid structure consisting of a finite-size superconducting sample with a magnetic dipole(s) on top. Our aim is to study the vortex-antivortex guidance by varying the angle between the direction of magnetization of the dipole and the external transport current. As a theoretical approach we use the time-dependent Ginzburg-Landau (TDGL) equations because they allow to study both the nucleation of the v-av pairs (see, e.g., [56]) and their dynamics self-consistently (e.g., in the London limit one needs to artificially create and annihilate v-av pairs by implying additional parameters/conditions). Within the London approach, related v-av dynamics was studied recently by Lima and de Souza Silva [57]. The nucleation of v-av pairs by a magnetic dipole and patterns formation of moving vortices was analyzed in a recent paper by Gladilin *et al.* [58]. Authors used the TDGL approach and they fixed the angle between $\mathbf{M}$ and $\mathbf{j}$ ($\mathbf{M}\perp\mathbf{j}$). Below we show that by varying the angle α it is possible to find novel and a richer dynamics of v-av pairs and new possibilities for vortex guidance in this system with magnetic dipoles.

3.2 Model

Let us consider a thin-film rectangular-shaped superconductor sample with a magnetic bar (or array of bars) on top which is magnetized in-plane and which is electrically isolated from the superconductor (see Fig. 3.1). A set of parameters of the system that we use to study the dynamics of v-av pairs corresponds to, e.g., the following experimental conditions. As a superconductor, we choose an Al thin film of thichness $d_{Al} = 50$ nm with the zero-temperature coherence length $\xi(0) = 153$ nm, the magnetic field penetration depth $\lambda(0) = 153$ nm [59] and the effective magnetic field penetration depth $\Lambda(0) = 470$ nm. A Co bar is separated

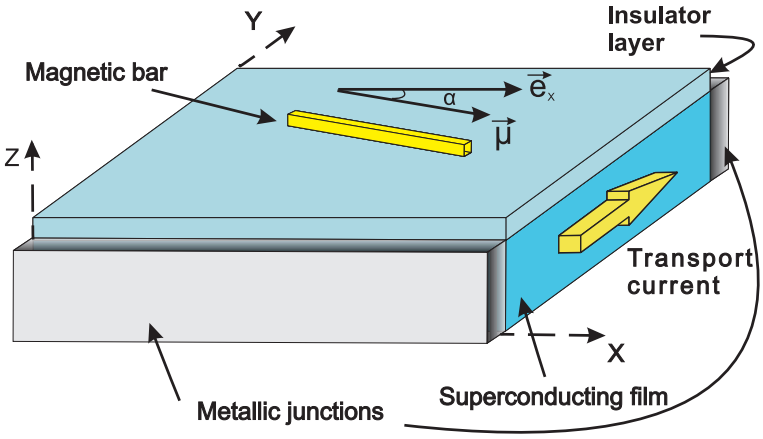

Figure 3.1: (Color online) A sketch of the envisioned experimental setup. Magnetic bar is magnetized in-plane and has magnetic moment $\vec{\mu}$. The direction of vector $\vec{\mu}$ forms angle α with the x-axis. The external current injected through the "normal metal – superconductor" boundary.

from the superconducting film by a Ge insulator layer of thichness $d_{Ge} = 139$ nm. The bar has typical dimensions 2900 nm $\times$ 76 nm $\times$ 153 nm and magnetic moment $\mu \approx 56\mu_0 = 2.24\ 10^{-19}$ A m^2, where $\mu_0 = \Phi_0\xi/2\pi = 4\ 10^{-21}$ A m^2. The magnetic moment of the dipole and thickness of the insulator are chosen in such way, to provide a single vortex under the dipole.

The bar creates a stray magnetic field which in turn can be modeled by two point-like magnetic dipoles directed perpendicular to the superconductor and positioned near the edges of the magnetic bar. In Fig. 3.2 we show that the real profile of the z-component of the magnetic field (which mainly affects the superconducting properties of the film) indeed could be modeled by a proper choice of the magnetization of two out-of-plane dipoles (see inset Fig. 3.2), the inter-dipole distance and the distance between them and the superconducting sample. Since the two-dipole model very well reproduces the "real" profile of the magnetic field (i.e., created by the bar), for convenience (especially in case of arrays of bars), we emply this model in our calculations.

Applied transport current exerts a force on the vortices/antivortices that are created by the magnetic dipole. To study the dynamics of the v-av pairs as a function of the angle between the applied current and the magnetic moment of the magnetic bar, we employ the time-dependent Ginzburg-Landau equation [60, 61],

$$u\left(\frac{\partial}{\partial t} + i\varphi\right)\psi = (\nabla - \mathrm{i}\mathbf{A})^2\psi + (1 - |\psi|^2)\psi. \tag{3.1}$$

This equation has to be solved together with the Poisson equation for the electrostatic potential,

$$\Delta\varphi \;=\; \mathrm{div}\left(\mathrm{Im}(\psi^*(\nabla - \mathrm{i}\mathbf{A})\psi)\right). \tag{3.2}$$

In Eqs. (1,2) all the physical quantities are expressed in dimensionless units: temperature in units of the critical temperature T_c, the vector potential $\mathbf{A}$ in

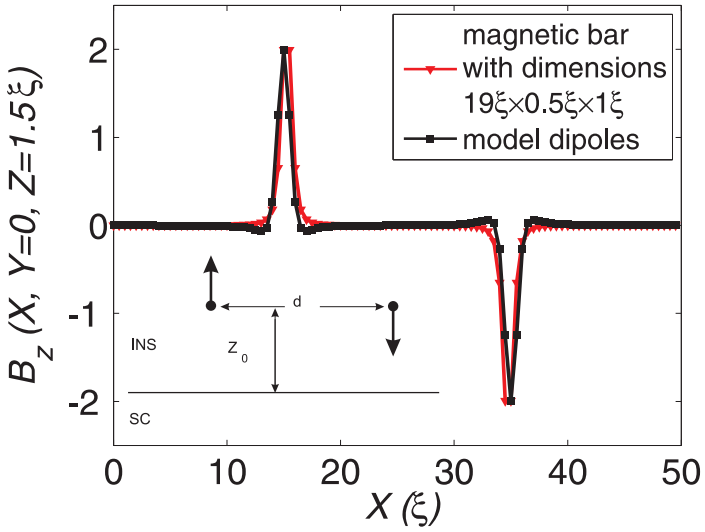

Figure 3.2: (Color online) The z-component of the magnetic field of the finite length in-plane dipole (solid red (grey) curve with triangular symbols) and of two out-of-plane point-like dipoles (solid black curve with square symbols). To fit these two curves we adjusted the distance between the two out-of-plane dipoles (i.e., took it 5% larger than the length of the in-plane bar) and the distance between the film and the out-of-plane dipoles (i.e., 1.5 times larger than for the in-plane bar). The inset shows the model with out-of-plane dipoles.

units $\Phi_0/(2\pi\xi(T))$ (where Φ_0 is the quantum of magnetic flux), the order parameter in units of $\Delta_0 = 4k_BT_cu^{1/2}/\pi(1-T/T_c)^{1/2}$, and the coordinates are in units of the coherence length $\xi(T) = (8k_BT_c/\pi\hbar D)^{-1/2}/(1-T/T_c)^{1/2}$. In these units magnetic field is scaled by $H_{c2} = \Phi_0/2\pi\xi(T)^2$ and the current density by $j_0 = \sigma_n\hbar/2e\tau_{GL}(T)\xi(T)$. Time is scaled in units of the Ginzburg-Landau relaxation time $\tau_{GL}(T) = \pi\hbar/8k_BT_cu/(1-T/T_c)$, the electrostatic potential (φ) in units of $V_0 = \hbar/2e\tau_{GL}(T)$, where σ_n is the normal-state conductivity, and D is the diffusion constant. Parameter u governs the time change of $|\psi|$ and the length of penetration of the electric field into a superconductor [62]. Since we are interested mainly in the dynamics of (anti)vortex motion but not in the time evolution of the vortex-antivortex nucleation and annihilation, for our problem the actual value of u does not play an essential role for the dynamics, and we choose the value $u = 1$ (note that depending on a specific superconductor, this value could vary, e.g., $u = 5.79$ [62]).

The vector potential in Eqs. (1,2) is the sum of the vector potentials of two point-like out-of-plane magnetic dipoles separated by a distance d and placed at a distance z_0 from the top surface of the superconducting film. We assume that the thickness of the superconducting film d_s is smaller than the effective (normal) magnetic-field penetration depth, $\Lambda = \lambda(T)^2/d_s$, where d_s is the thickness of the sample, and therefore we can neglect the influence of the screening and transport currents on $\mathbf{A}$.

In the x-direction we used the usual isolator-superconductor boundary conditions for the order parameter and the normal current density: $(\nabla - i\mathbf{A})\psi|_n = 0$, $\partial\varphi/\partial n = 0$, and in the y-direction we used the "normal metal-superconductor" boundary conditions: $\psi = 0$, $\partial\varphi/\partial n = -j_n$. The current is applied along the y-axis as shown in Fig. 3.1.

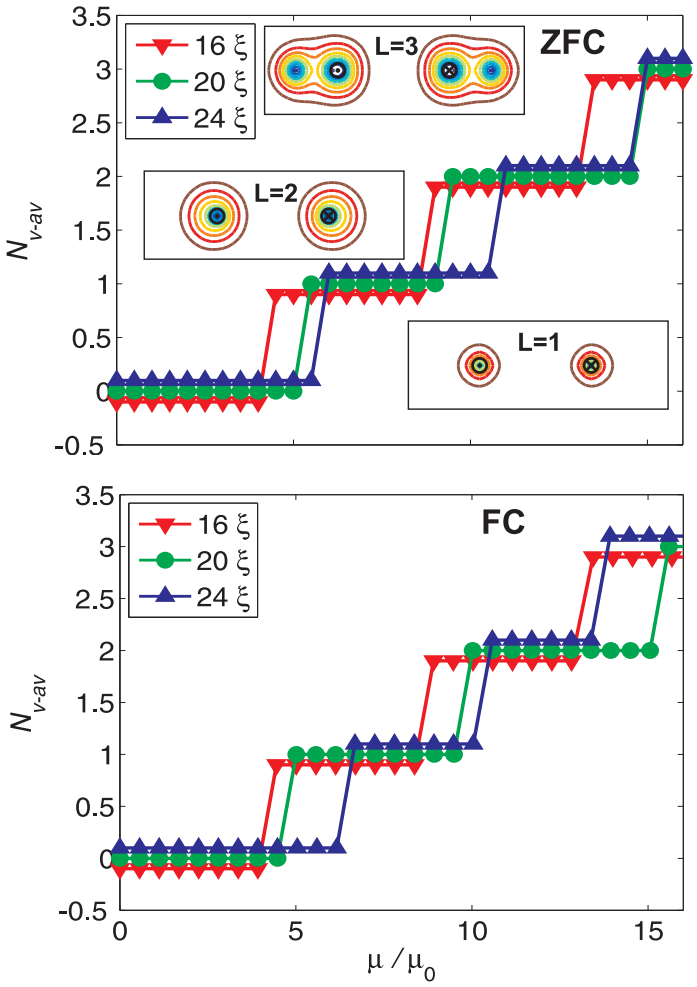

Figure 3.3: (Color online) Average number of v-av pairs as a function of magnetic moment (magnetization) of the out-of-plane dipole. In our calculations we used out-of-plane dipoles with $\mu/\mu_0 \simeq 5.6$, which generate (anti)vortices with vorticity $L = 1$. Different lines with symbols represent the dependence for different distances between the out-of-plane dipoles d (the lines are slightly shifted along the $y-axis$ in order to better distinguish them). Insets show the contour plots of the order parameter in equilibrium (v-av pair states). Note that for the used parameters, i.e., the magnetic moment μ of the dipole, d and Z_0 (see Fig. 3.2), we obtain a giant vortex for $L = 2$ "trapped" by a "hole" in the order parameter created by the field of the magnetic dipole. However, this "hole" cannot sustain giant vortex for $L = 3$. Depending on the magnetic moment of the out-of-plane dipole ($\vec{\mu}$), different number of v-av pairs are generated in the superconducting stripe. $L = 1$ is the equilibrium state for $\mu/\mu_0 = 6$, $L = 2$ for $\mu/\mu_0 = 12$, and $L = 3$ for $\mu/\mu_0 = 18$.

Numerical solution of the TDGL equations is obtained using the finite-difference method and the Fourier analysis and cyclic reduction method (FACR) [27, 63, 64].

Depending on the parameters of the out-of-plane dipoles (such as the magnetic moment, $\vec{\mu}$ and the distance between the dipoles, d), different number of v-av pairs can be generated in the superconducting sample, as shown in Fig. 3.3.

In our calculations, we chose μ such that it corresponds to the presence of a single vortex-antivortex pair created in a "field-cooled" (FC) regime and no vortices created in a "zero-field-cooled" (ZFC) regime[65]. This means that the magnetic bar is "weak" enough to create v-av pairs by its own and we apply currents which itself also do not create v-av pairs.

3.3 Guidance of v-av pairs by magnetic dipoles

3.3.1 Case of a single dipole

The orientation of an in-plane dipole with respect to the direction of the applied current significantly influences the vortex dynamics. For $\alpha = 0$ (where α is the angle between the x-direction and an in-plane magnetic dipole vector, see Fig. 3.1), the vortex and antivortex created by the in-plane dipole move in opposite directions towards the boundaries and their trajectories are straight lines (Fig. 3.4(a)). However, for $0 < \alpha < 75°$ the trajectories change qualitatively, i.e., they acquire a curvature (Fig. 3.4(b)). Also, the direction of motion of the v-av pairs no longer coincides with the direction of the Lorentz force due to the external current, i.e., we observe *v-av guidance*. Further increase of α results in a dramatic change of the v-av motion: thus at $\alpha = 75°$ the v-av attraction exceeds the repulsive component of the Lorentz force, and the v-av pair *collapses* (Fig. 3.4(c)). For even larger angles, the projection of the Lorentz force on the dipole's axis assists the v-av annihilation. In that case the v-av pair annihilates very fast. This regime holds for angles $75° < \alpha < 285°$, when no force tends to break the v-av pair and forces its components to move in the opposite directions. The angular dependence of the vortex-antivortex velocities corresponding to the system shown in Figs. 3.4(a-c) is shown in Fig. 3.5.

In a finite-size sample, the v-av motion is influenced by boundary effects. In a symmetric case, when the magnetic bar is placed at the center of the sample, and $\alpha = 0$ (see, e.g., Fig. 3.4(a)), the effects of boundaries in the y-direction cancel each other and thus produce no effect on the vortex motion. The boundary effects become more appreciable in case of non-zero α. Thus at $\alpha = 75°$ the trajectories of motion of (anti)vortices become strongly distorted by the interaction with the images, and as a result (anti)vortices deviate from the initial direction of motion and leave the sample through the boundaries in the y-direction (Fig. 3.4(b)). To reduce the effect of boundaries, we performed calculations for a larger system. The results are shown in Figs. 3.4(d-f). The trajectories of v-av motion to a lesser extent are influenced by the boundaries than in case of a smaller sample.

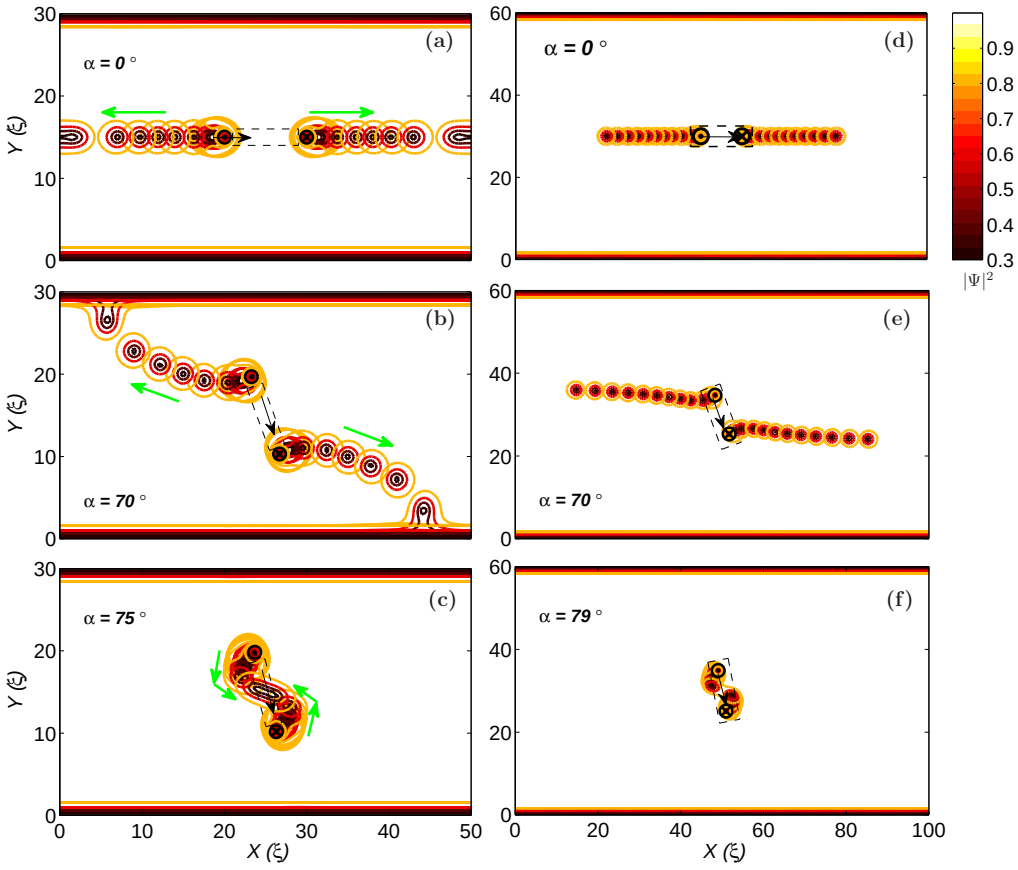

Figure 3.4: (Color online) Trajectories of the motion of v-av pairs for different orientations of the in-plane dipole with respect to the direction of the current: $\alpha = 0$ (a), $\alpha = 70°$ (b), and $\alpha = 75°$ (c), and $\alpha = 0$ (d), $\alpha = 70°$ (e), and $\alpha = 79°$ (f) (a larger samle). The bias current is equal to $j = 0.09 j_0$ (a-c), $j = 0.11 j_0$ (d-e), where $j_0(T = 0) = 0.6\ 10^6$ A/cm^2 (the same value is used in Figs. 3.6, 3.8, and 3.10). The order parameter is depleted at the upper and lower side of the sample due to the proximity of the normal metal junctions [34, 47, 66]. The trajectories are shown as sets of successive snapshots of the order parameter profile associated with v-av pairs. The direction of motion of v-av pairs (i.e., starting from the poles of the bar) is shown by green (grey) arrows. Small dashed-line rectangles with arrows inside show the magnetic bars and the direction of their magnetic moment $\vec{\mu}$.

3.3.2 Guidance by an array of dipoles

In the above case of a single magnetic dipole, (anti)vortices are attracted to the boundaries, which is a consequence of the interaction with its antivortex(vortex) images [34, 66]. Therefore, the effect of guidance is strongly influenced by finite-size effects. In order to reduce the effect of the boundaries, we consider a larger sample and place on top of it a rectangular array of magnetic dipoles (for experimental realization, see Ref. [59]). In Fig. 3.6, such an array consisting of twelve magnetic

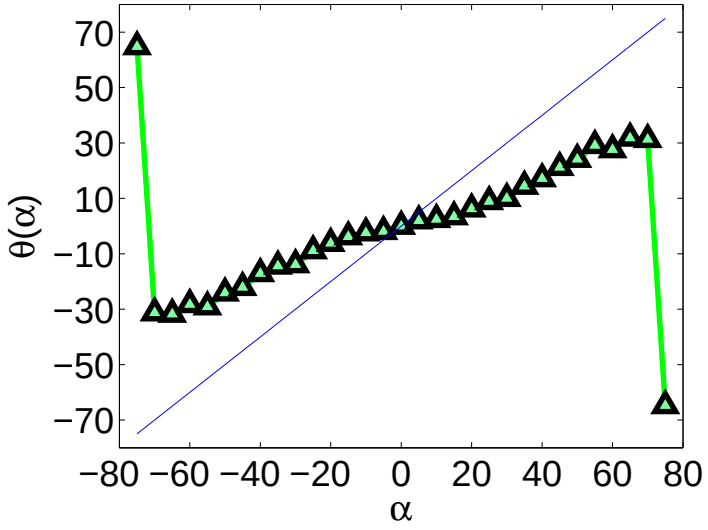

Figure 3.5: (Color online) Angular dependence of the v-av velocity (plotted triangular symbols connected by solid line) versus the angular dependence of a single vortex motion ("unguided motion") is plotted by thin straight solid line. The peak at α close to $\pm 75°$ corresponds to the critical angle α_c when the "guided-motion" regime switches to "v-av annihilation" (i.e., when a vortex annihilates with the antivortex of the same in-plane dipole).

dipoles is shown for different orientations of the dipoles with respect to the driving current.

For $\alpha = 0$ (Fig. 3.6(a)), vortex and antivortex created by each dipole move in the opposite directions (along the direction of the Lorentz force created by the external current) and annihilate with antivortex and vortex produced by adjacent dipoles. Increasing the angle α results in a v-av guidance by the array of dipoles. Being depinned and driven by the Lorentz force, v-av pair moves in a field of forces created by other dipoles (see below) and thus the direction of its motion deviates from that of the driving force (Fig. 3.6(b)). For some critical angle $\alpha_c = 58°$ ($j/j_0 = 0.09$, $d = 20\xi$) (Fig. 3.6(c)) the projection of the Lorentz force on the direction of the magnetic moment of the dipole occurs to become insufficient to break up the v-av pair, and the vortex annihilates with the antivortex of its own in-plane dipole.

The dynamics of every (anti)vortex can be described by the interplay of the following forces that act on a (anti)vortex (Fig. 3.7): (i) the Lorentz force $\vec{F}_L^{(1)}$ created by the external current, (ii) the attractive v-av force to the antivortex created by the neighbor in-plane dipole $\vec{F}_{v-av}^{(2)}$, (iii) the attractive force to the antivortex created by its own in-plane dipole $\vec{F}_{av}^{(3)}$, and (iv) the attraction to its out-of-plane dipole $\vec{F}_{v-d}^{(4)}$. For $\alpha = \alpha_c$, the force $\vec{F}_{av}^{(3)}$ overcomes the forces $\vec{F}_L^{(1)}$, $\vec{F}_{v-av}^{(2)}$ and $\vec{F}_{v-d}^{(4)}$, the vortex dynamics will be changed: a v-av created by each out-of-plane dipole will annihilate.

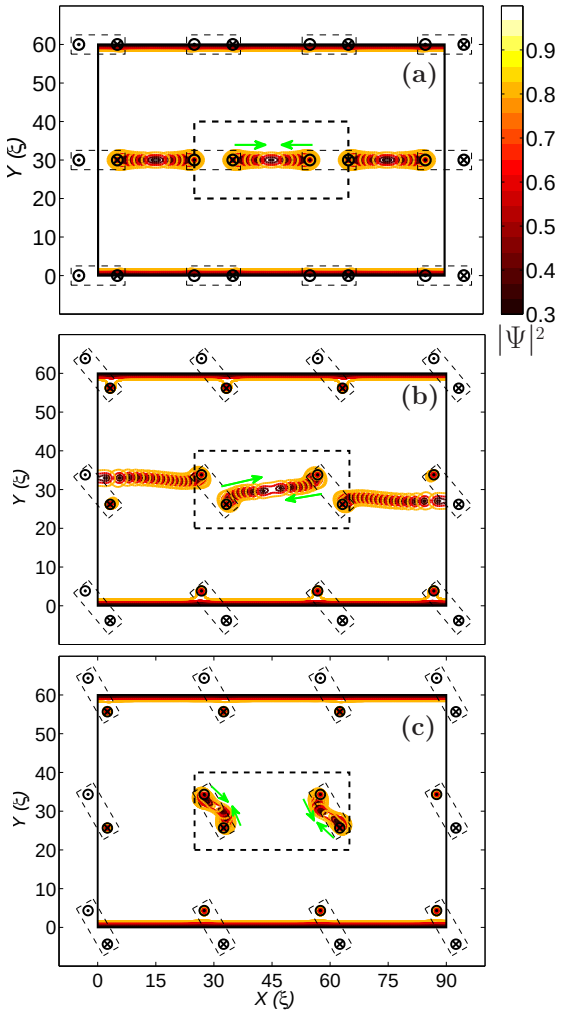

Figure 3.6: (Color online) Trajectories of motion of v-av pairs of an array of in-plane dipoles for: $\alpha = 0$ (a), $\alpha = 50°$ (b), and $\alpha = 60°$ (c). The bias current is equal to $j = 0.09 j_0$. The trajectories for the v-av pairs in the central part of the sample (shown by large dashed-line rectangle) were analyzed to construct the phase diagram shown in Fig. 8. Magnetic bars are shown by small dashed-line rectangles. Other symbols used here are the same as in Fig. 4.

3.3.3 Phase diagram

The v-av dynamics changes dramatically when the balance of forces that act in the same and the opposite direction to the Lorentz force change (see Fig. 3.7). As shown above, this can be realized by changing the angle α. On the other hand, this balance can also be changed by tuning the applied current. To reveal the influence of the driving current on the v-av dynamics, let us consider different dipole orientations.

1. *Small* α ($\alpha < \alpha_c$):

a) If the driving current is less than some critical ("depinning") value, a v-av pair

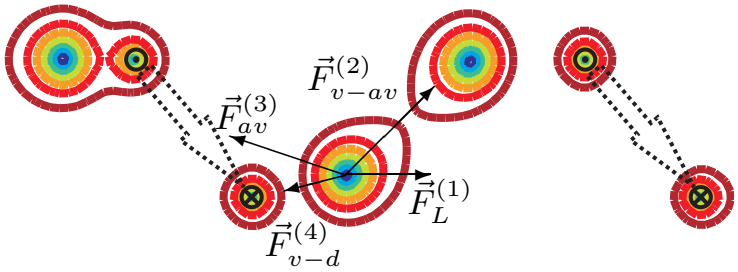

Figure 3.7: (Color online) The force balance that act on a vortex: (i) the Lorentz force $\vec{F}^{(1)}_L$ created by the external current, (ii) the attractive v-av force to the antivortex created by the adjacent magnetic bar $\vec{F}^{(2)}_{v-av}$, (iii) the attractive force to the antivortex created by its own in-plane dipole $\vec{F}^{(3)}_{av}$, and (iv) the attraction (i.e., "pinning force") to its out-of-plane dipole $\vec{F}^{(4)}_{v-d}$. Dotted arrows represent magnetic moments of magnetic bars.

remains "pinned" by the in-plane dipole. The "critical depinning current" depends on the pinning force and on the array period (i.e., the distance between neighboring dipoles): the closer the in-plane dipoles are stronger the attractive force that acts on the (anti)vortices.
b) For a current beyond the "critical" value, the driving Lorentz force overtakes the pinning threshold and the v-av will move. An interesting regime occurs when the effects of the driving force and of the dipole lattice are comparable. Then a slight imbalance in the forces gives us the opportunity to control the vortex dynamics (i.e., by slightly tuning the driving current). This regime results in a pronounced guidance effect.
c) For larger current values, the v-av motion will be determined mainly by the magnitude of the Lorentz force rather than by the influence of the lattice of the in-plane dipoles (i.e., the effect of guidance will be suppressed).
2. *Large* α ($\alpha_c < \alpha < 90°$):
Small currents cannot prevent the annihilation of a vortex with an antivortex created by an in-plane dipole. Only a very large applied current can change the dynamics: its magnitude should be large enough to break up the attractive v-av interaction.
3. $\alpha > 90°$:
The only scenario is the annihilation of a vortex with the antivortices created by the same in-plane dipole. The current does not change the direction of the resulting sum of forces $\vec{F}^{(1)}_L$, $\vec{F}^{(2)}_{v-av}$, $\vec{F}^{(3)}_{av}$, and $\vec{F}^{(4)}_{v-d}$.

Alternatively, the dynamical regime can be controlled also by the length of magnetic bar (or the distance d between the out-of-plane dipoles in our model). Thus with increasing d, the force $\vec{F}^{(3)}_{av}$ decreases while $\vec{F}^{(2)}_{v-av}$ increases. (Note that forces $\vec{F}^{(4)}_{v-d}$ and $\vec{F}^{(1)}_L$ do not depend on the lattice period, but are determined by the magnetic moment of the dipole and the transport current.) Therefore, we can expect that the critical angle α_c will be larger for a larger dipole size (and the

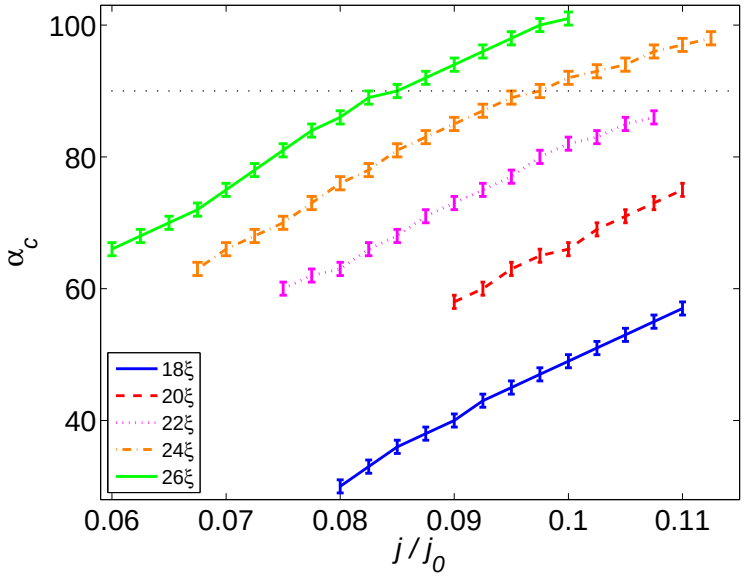

Figure 3.8: (Color online) The "critical angle α_c – current j/j_0" phase diagram for the array of dipoles shown in Fig. 3.6, for different length of the magnetic bar.

same current). This is explained by the fact that the interaction between vortex and antivortex of the same in-plane dipole becomes weaker, therefore the angle α should be increased in order to compensate the action of the driving force. This intuitive analysis is confirmed by our numerical calculations of the phase diagram "critical angle α_c – current j/j_0" shown in Fig. 3.8 for different size of the magnetic bar (i.e., the distance d between out-of-plane dipoles). In a similar way, we can explain the observed monotonous increase of α_c versus j/j_0. For a fixed distance L an increasing driving Lorentz force has to be compensated by increasing the critical angle α_c.

3.4 Critical currents and IV-curves

In this section we discuss the critical current of our structure which depends on the angle between the current and the magnetic moment of the in-plane dipole. We also study the dynamics of vortices at $J \sim J_c$ (when we are in a regime of slow vortex motion) and we show that our findings of the previous section fit with the regime when there is a permanent generation of v-av pairs and a finite voltage drop across the film. For the used parameters of the dipole the depinning current density is on average of the order of the depairing current density and it is minimal for $\alpha = 0$ and it is maximal for $\alpha = 135°$. We explain such a difference by the nonuniform current distribution around the dipole leading to a sign change of the local current induced by the magnetic dipole and (anti)vortices (see Figs. 3.9).

In Fig. 3.10 we present the current-voltage characteristics for different angles α. The maximal J_c is reached for $\alpha = 135°$ and the minimal one for $\alpha = 0$. The difference in the critical currents can be explained by the effect of the edges and different current density distribution for various α.

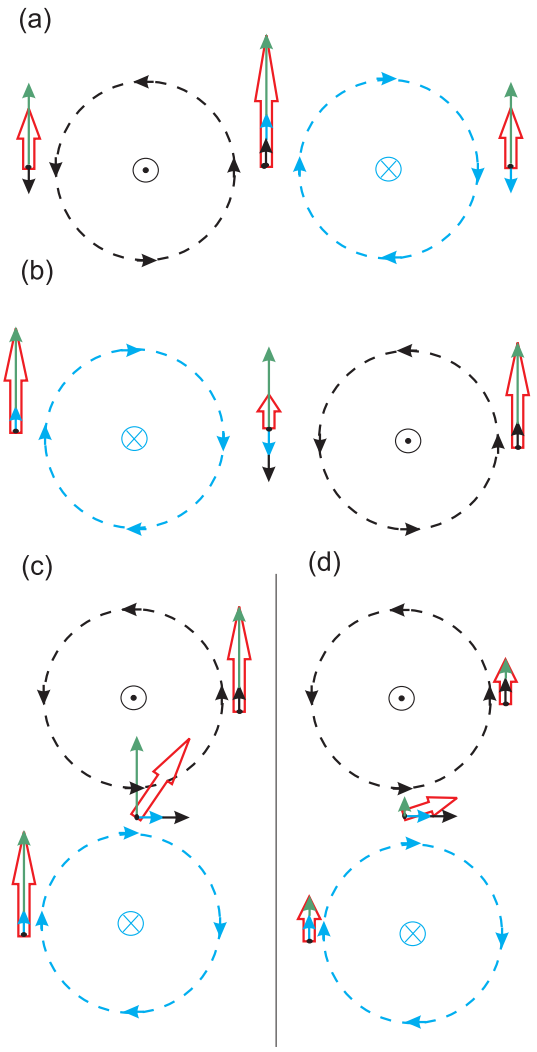

Figure 3.9: (Color online) Scheme illustrating the distribution of the total current in the sample, including: (i) the current induced by the magnetic out-of-plane dipoles of different polarity (shown by black and blue (gray) dashed lines and arrows), and (ii) the transport current (shown by green (dark gray) arrows), for differnt orientation of the magnetic bar with respect to the direction of the transport current. The total current in the different points of the sample is shown by red (dark gray) thick arrows.

Indeed when $\alpha = 0$ (see Fig. 3.9(a)) the maxima of the sum of the transport current density and the magnetic dipole induced current density is located under the magnetic bar. Depending on the lenght of the magnetic bar one (short dipole) or two (long dipole) v-av pairs will be created. For case of a long bar, one v-av pair will annihilate at the edge of the magnetic bar and another vortex/antivortex will be separated by the applied current. As a result, the v-av pair will reach the edges and exit the superconductor.

In case of $\alpha = 180°$ the maxima of the current density will be outside the in-plane dipole (see Fig. 3.9(b)). It is clear that in the latter case we need a

larger transport current to reach locally the depairing current density which is the nessesary condition for permanent generation of v-av pairs. The vortex dynamics will be similar to the case $\alpha = 0$ except for the fact that two v-av pairs will be always created.

When we gradually increase α from zero one can expect an increase of the critical current due to a finite angle between the dipole induced current density and the transport current density (in this case one needs a larger transport current to nucleate the vortex-antivortex pairs). It explains the increase of the critical current for $\alpha = 45°$ in comparison to the case $\alpha = 0$. The vortex dynamics has the same features as for $\alpha = 0$. The only difference is that the (anti)vortices do not follow straight trajectories anymore (see inset in Fig. 3.10).

To understand why J_c is larger for $\alpha = 90°$ than for $\alpha = 180°$ we need to take into account the influence of the edges of the superconductor. Qualitatively we can describe it by putting the image of the model dipoles on the opposite side of the edges of the superconducting film (actually it should be an infinite series of such dipoles because we have two edges, but for qualitative understanding of the physics of the observed effect we consider only one image). The presense of the dipole "images" leads to an enhancement of the dipole induced current density in points which are not far from the film edges. When $\alpha = 90°$, the distance between the dipole and the edges will be larger than for $\alpha = 180°$ and besides from the symmetry of the problem we can expect a vanishing effect of the boundaries. Therefore, we have an enhancement of the critical current. At $\alpha = 90°$ two vortex-antivortex pairs are nucleated near the poles of the magnetic bar. Depending on the length of the bar one pair will annihilate under the dipole (for short dipoles) and the other vortex and antivortex will move in opposite directions and exit the sample.

3.5 Conclusions

Using the time-dependent Ginzburg-Landau equations, we studied the vortex-antivortex dynamics in a hybrid system consisting of a thin-film finite-size superconducting sample with a magnetic bar (or arrays of bars) on top. Vortex-antivortex pairs are generated at the edges of the magnetic bar and they are driven by the Lorentz force produced by an external current. The vortex-antivortex dynamics is studied as a function of the angle α between the direction of the dipole(s) and that of the Lorentz force. We found that the direction of motion of (anti)vortices coincides with that of the Lorentz force only for $\alpha = 0$ while in the general case of $\alpha \neq 0$ the direction of the (anti)vortex velocity vector does not coincide with the direction of the Lorentz force. Thus we revealed the effect of guidance of the (anti)vortex motion due to the magnetic bars. In case of a single magnetic bar, the (anti)vortex motion is strongly influenced by boundary effects, i.e., by the interaction of the (anti)vortices with their images. On the other hand, in an array of magnetic bars the (anti)vortex motion is governed by the balance of the interaction forces with the array environment. Depending on the relation between the driving force and the interaction forces, we found different dynamical regimes of (anti)vortex motion. The most interesting regime is observed when the

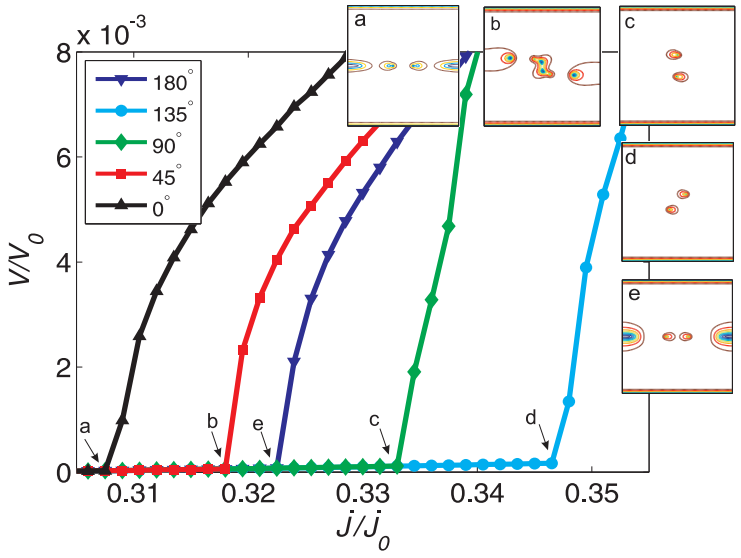

Figure 3.10: (Color online) The IV-curve for one in-plane dipole system for different angles α between the x-axis direction and that of the magnetic dipole of the in-plane magnetic bar. Insets show snapshots of the order parameter distribution in the sample corresponding to different values of the current (shown by characters (a to e) and small arrows).

parameters of the system are chosen in such a way that the driving force and the typical interaction forces of (anti)vortices with magnetic dipoles are of the same order (which can be provided by a proper choice of the size and the magnetic moment of the bars). In this case, switching between different dynamical regimes, which include either guided motion of (anti)vortices or vortex-antivortex annihilation (resulting in zero voltage), can be achieved by slightly changing the applied current. To study the effect of the external current, we calculated the phase diagram "critical angle – current", for different sizes of the magnetic bars. We found that the value of the critical angle increases with increasing the length of the bars, for the same applied current. To better understand the nature of the revealed different dynamical regimes, we analyzed in detail the IV-curves for different angles α. Our approach allows to self-consistently account for the nucleation of vortex-antivortex pairs and study their dynamics. The obtained results provide a tool for an effective manipulation of magnetic flux in nano-patterned hybrid structures and therefore could be potentially useful for applications in fluxonics devices.

Chapter 4

Controlling magnetic flux motion by arrays of zigzag-arranged magnetic bars

Recent advances in manufacturing arrays of artificial pinning sites, i.e., antidots, blind holes and magnetic dots, allowed an effective control of magnetic flux in superconductors. An array of magnetic bars deposited on top of a superconducting film was shown to display different pinning regimes depending on the direction of the in-plane magnetization of the bars. Changing the sign of their magnetization results in changes in the induced magnetic pinning potentials. By numerically solving the time-dependent Ginzburg-Landau equations in a superconducting film with periodic arrays of zigzag-arranged magnetic bars, we revealed various flux dynamics regimes. In particular, we demonstrate flux pinning and flux flow, depending on the direction of the magnetization of the magnetic bars. Remarkably, the revealed different flux-motion regimes are associated with different mechanisms of vortex-antivortex dynamics. For example, we found that for "antiparallel" configuration of magnetic bars this dynamics involves a repeating vortex-antivortex generation and annihilation. We show that the depinning transition and the onset of flux-flow can be manipulated by the magnetization of the bars and the geometry of the array. This provides an effective control of the depinning critical current that can be useful for possible fluxonics applications.

The results of this chapter have been published in Ref. [67].

4.1 Introduction

Nanoscience relies upon the modification of the properties of the same material through its nanostructuring and the optimization of the confinement potential and topology [68]. It has been shown that properties of hetero-structures significantly distinguish from those of an intrinsic superconductor (SC) [69]. Thus embedding ferromagnetic nanostructures allows to improve the properties of a SC: the critical current (see, e.g., Ref. [70]), the critical temperature [71] and the pinning potential [72]. As a result, the range of applications of hetero-structured SC is much wider than that of pure SC. The magnetic confinement permits to govern

the physical properties of the confined condensates and magnetic flux. Magnetic nanostructures are specially interesting because their magnetic moments can be easily controlled, giving rise to a high degree of tunability of their flux pinning properties. This has been demonstrated in recent experiments in which arrays of nanomagnets were shown to trap vortices quite efficiently, either by local reduction of the critical temperature via the proximity effect [47, 73] or by their magnetic flux when the dots are polarized [48, 74, 75].

Controlling the vortex motion and creating a guided vortex motion [41, 76] via nanoengineering of arrays of pinning sites [39] or channels in the superconductor, makes it possible to develop new devices like superconducting transistors, switches, pumps [77], etc. [78] This paves the way for designing new generations of devices based on the controlled behavior of fluxons. The charge and the spin of electrons form the core of electronics and spintronics, respectively. In the same way, mastering fluxon behavior in nanostructured superconductors creates exciting new possibilities to develop the basics of fluxonics. By optimizing the condensate and the flux confinement, the superconducting critical parameters can be enhanced through nanostructuring.

There are a variety of nanoscale configurations used to confine flux and the condensate in nanostructured superconductors, moving from single nanocells (loop, disc, triangle, square, etc.) via their clusters to their arrays (antidot lattices, etc.) [18, 21, 79, 80]. In addition to that, nanoscale magnetic templates, where highly inhomogeneous local magnetic fields were generated by ferromagnetic nanodots and magnetic domains, are considered in superconductor-ferromagnet hybrid nanosystems.

Examples of magnetic hetero-structures include: thin superconducting films with thin magnetic disks on top [81], ferromagnetic square microrings [82], parallel [59, 83] and orthogonal [84] periodic patterns of Co bars (see Fig. 4.1), etc. (see review paper [85]). In all these systems the intense stray field generated by a magnet deposited on top of the system depletes the superconducting order parameter. This universal behavior is observed regardless of the superconductor type. In those systems the distribution of the current density in the superconductor is rather inhomogeneous and vortex trajectories which are determined by the current density distribution as well as by the interaction with the complex potential-energy landscape created by the defects and by the interaction with other vortices, may have very complicated shape.

In this work, we investigate the vortex-antivortex dynamics in a SC film with a rectangular array of ferromagnetic bars in a zigzag configuration (see Fig. 4.2) deposited on top. This magnetic-bar configuration has been experimentally investigated in Ref. [84]. The stray field of the array of magnetic bars governs the dynamic regime of the (anti)vortex motion in an infinite SC film. It is possible to change the magnetization of the zigzag bar pattern by applying an in-plane magnetic field. Depending on the initial magnetic field orientation, one can obtain two different magnetic field profiles in the film. This profile will affect (anti)vortex motion in the SC film. We demonstrate that changing the set up of the magnetic profile, we can tune the vortex system between the flux-flow (FF) and pinned regime. The simplicity of changing the magnetic profile makes this system very attractive for

further experiments. As a theoretical approach, we rely upon the time-dependent Ginzburg-Landau (TDGL) equations which allow us to study self-consistently both the nucleation of the vortex-antivortex (v-av) pairs (see, e.g., [60]) and their dynamics. This provides an obvious advantage of the used method (as compared, e.g., to molecular-dynamics simulations of vortices) in case of arrays of magnetic dots (bars) where the vortex-antivortex dynamics is accompanied by the nucleation and annihilation of v-av pairs. For example, we revealed that the mechanism of flux motion in case of "antiparallel" configuration of magnetic bars is associated with a repeating generation and annihilation of vortex-antivortex pairs under the tips of adjacent bars.

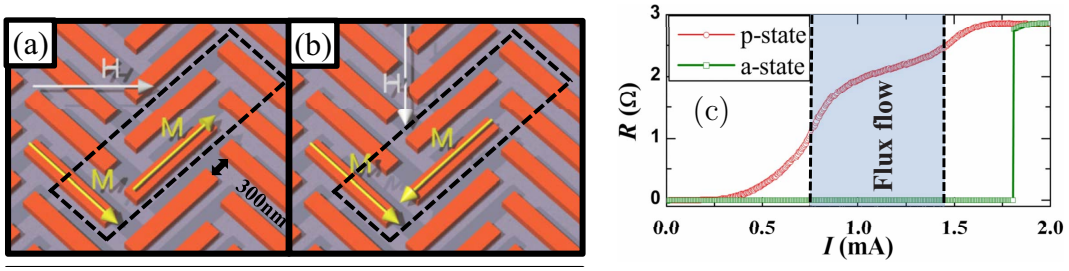

Figure 4.1: (a,b) Schematical representation of the magnetization procedure to obtain an antiparallel (a) and parallel (b) field distribution in an array of in-plane magnetic dots. (c) Resistance R vs current I curves for the a and p state at $T = 0.7K$ and $H = -0.5mT$ (after Ref. [84]).

This paper is organized as follows. In Sec. 4.2, we describe the model system. In Sec. 4.3, we demonstrate the essential role of the magnetization of the out-of-plane dipole and its position above the surface of a SC for the vortex motion. In Sec. 4.4, IV-curves of the system and various mechanisms of flux motion are analyzed. The results obtained in the present work are divided into two parts: one for a system modeled by out-of-plane dipoles and the second one — by in-plane dipoles. The results with in-plane simulations are presented in Sec. 4.5. Our main results and insights are summarized in Sec. 4.6.

4.2 Model

Our system consists of a superconducting film with an array of magnetic bars deposited on top of the superconductor. Depending on the geometry of the bars (e.g., whether they are narrow or wide) and the array, the bars are modeled either by (i) out-of-plane magnetic dipoles [33], or (ii) in-plane dipoles (the typical dimensions are $3 \times 32\xi$). The superconducting film is assumed to be of a finite length (in the direction of the leads) and of infinite width, which provides an adequate description of vortex creep in a real system. To model the infinite (in one direction) film, we use periodic boundary conditions applied to the phase and amplitude of the order SC parameter. The geometry of the system is as follows: the magnetic bars are deposited on top of a thin insulating layer (with separation z along the

z-direction) of the rectangular SC film as "ribbons" are formed under an angle of 45° with respect to the film face. Therefore, the bars in the adjacent rows form an angle of 90° with respect to each other, i.e., a "zig-zag" configuration (see Fig. 4.2). For instance, in case of a "narrow" magnetic bar, we model a Co bar with typical dimensions 2900 nm × 76 nm × 153 nm, separated from the superconducting film by a Ge insulator layer of thickness $z = 139$ nm which provides the magnetic momentum: $\mu \approx 56\mu_0 = 2.24\ 10^{-19}$ A m^2, where $\mu_0 = \Phi_0\xi/2\pi = 4\ 10^{-21}$ A m^2. This system is attractive due to the simplicity of changing the direction of magnetization by applying an in-plane magnetic field.

In our simulations, we use a film with length 30ξ and width 80ξ, where ξ is the superconducting coherence length at zero temperature T. In order to (re)magnetize the bars, an in-plane uniform magnetic field is applied either along the x- or the y-direction. As a result, the bars are magnetized either in an "anti-parallel" (AP) (Fig. 4.2(a,b)) or in a "parallel" (P) (Fig. 4.2(c,d)) configuration. It is assumed that the bars are magnetized using the field-cooled regime (FC), and after some relaxation time, the generated vortices are trapped under the tips of the bars. This results in two types of magnetic-field profiles (along the lines connecting the apices of the bars) shown in Figs. 4.3(a) and (b), corresponding to the AP and P magnetization configurations (Fig. 4.2). The two generated magnetic-field profiles are quantitatively and qualitatively different: the one corresponding to the AP magnetization configuration consists of periodic sharp peaks of opposite polarity (Fig. 4.3(a)) while the one resulting from the P magnetization configuration is a twice as dense set of sharp peaks of the same polarity (Fig. 4.3(b)). Clearly, the transition from one magnetic-field configuration to the other significantly changes the condition for (anti-)vortex motion along the magnetic-field modulated "paths" (or "channels"). Note that the height and width of the peaks are determined by the magnetization of the bars (or the dipoles in the out-of-plane dipole model) and the separation z between the dipole and the SC film (i.e., the thickness of the insulating layer).

As we showed by direct calculation of the magnetic-field profile created by an in-plane magnetized bar, the real profile of the z-component of the magnetic field (which mainly affects the superconducting properties of the film) of a narrow bar could be modeled by a proper choice of the magnetization of two out-of-plane dipoles (see inset of Fig. 2 in Ref. [33]), the inter-dipole distance and the distance between them and the superconducting sample.

After the initial configuration of the system (i.e., the magnetic field profile and the distribution of (anti)vortices) is being prepared, the current is turned on, and we investigate the v-av dynamics. To study the dynamics of the vortex-antivortex (v-av) pairs, we employ the time-dependent Ginzburg-Landau equation [60, 61]:

$$u\left(\frac{\partial}{\partial t} + i\varphi\right)\psi = (\nabla - \mathrm{i}\mathbf{A})^2\psi + (1 - |\psi|^2)\psi. \tag{4.1}$$

The equation is to be solved self-consistently with the Poisson equation for the electrostatic potential,

$$\Delta\varphi \;=\; \mathrm{div}\left(\mathrm{Im}(\psi^*(\nabla - \mathrm{i}\mathbf{A})\psi)\right). \tag{4.2}$$

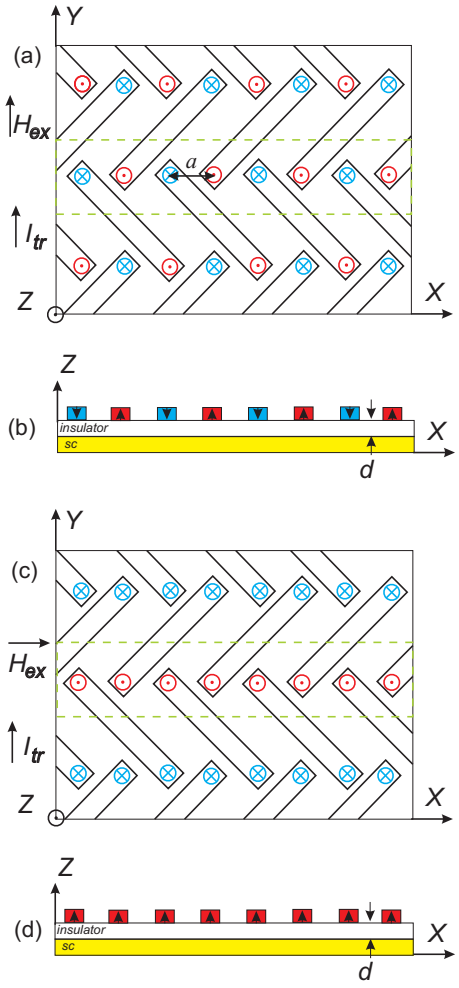

Figure 4.2: (Color online) The model system. The magnetization of the bars changes under the external magnetic field H_{ex} and modulates differently in the central area (green (gray) dashed box). The orientation of the initial magnetic field generates (a, b) antiparallel (AP) and (c,d) parallel (P) configuration. Circled dots and crosses show the location of out-of-plane dipoles whose magnetic field is approximately the same as the field of the bar. The current leads are at the bottom and the top of the SC film. I_{tr} shows the direction of the transport current flow. a denotes the distance between the neighbor bar tips (i.e., the off-plane dipoles). The meaning of the x, y, and z-axes is clear from the plot.

In Eqs. (1) and (2), all the physical quantities are expressed in dimensionless units: temperature T in units of the critical temperature T_c, the vector potential $\mathbf{A}$ in units $\Phi_0/(2\pi\xi(T))$ (where Φ_0 is the quantum of magnetic flux), the order parameter in units of $\Delta_0 = 4k_BT_cu^{1/2}/\pi(1-T/T_c)^{1/2}$, and the coordinates are in units of the coherence length $\xi(T) = (8k_BT_c/\pi\hbar D)^{-1/2}/(1-T/T_c)^{1/2}$. Using these units, the magnetic field is scaled by $H_{c2} = \Phi_0/2\pi\xi(T)^2$ and the current density by $j_0 = \sigma_n\hbar/2e\tau_{GL}(T)\xi(T)$. Time is scaled in units of the Ginzburg-Landau relaxation time $\tau_{GL}(T) = \pi\hbar/8k_BT_cu/(1-T/T_c)$, the electrostatic potential φ in

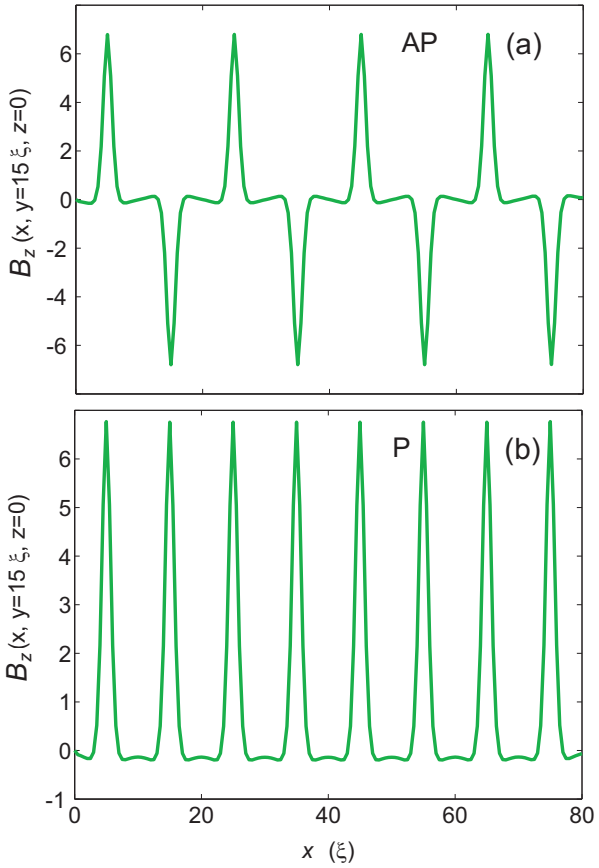

Figure 4.3: (Color online) The magnetic field profile $B_z(x, y = 15, z = 0)$ induced by the dipoles. The positions of the sharp peaks represent the location of the magnetic dipole. Magnetic momentum $\mu_z = 1\mu_0$ is strong enough to induce one v-av pair only with vorticity $L = 1$ for each H_{c2} period. The magnetic profile is created by: a) antiparallel dipoles and b) parallel dipoles.

units of $V_0 = \hbar/2e\tau_{GL}(T)$, where σ_n is the normal-state conductivity, and D is the diffusion constant. Parameter u governs the time change of $|\psi|$ and the length of penetration of the electric field into a superconductor [62]. Since we are interested mainly in the dynamics of vortex-antivortex motion but not in the time evolution of the v-av nucleation and annihilation, for our problem the actual value of u does not play an essential role, and we choose the value $u = 5.79$ (note that this value depends on the specific superconductor).

The vector potential in Eqs. (1) and (2) is the sum of the vector potentials induced by magnetic dipoles which are placed at a distance $z_0 = 2.8\xi$ from the top surface of the superconducting film. We assume that thickness of the superconducting film d_s is smaller than the Pearl penetration depth, $\Lambda = \lambda(T)^2/d_s$ [86]. Due to the fact that our system is infinite in the x-direction, there is no screening current along the y-direction. However, in a real system the influence of the screening currents on $\mathbf{A}$ may be omitted if the film width is smaller than Λ [58].

In the x-direction we use the usual periodic boundary conditions for the mag-

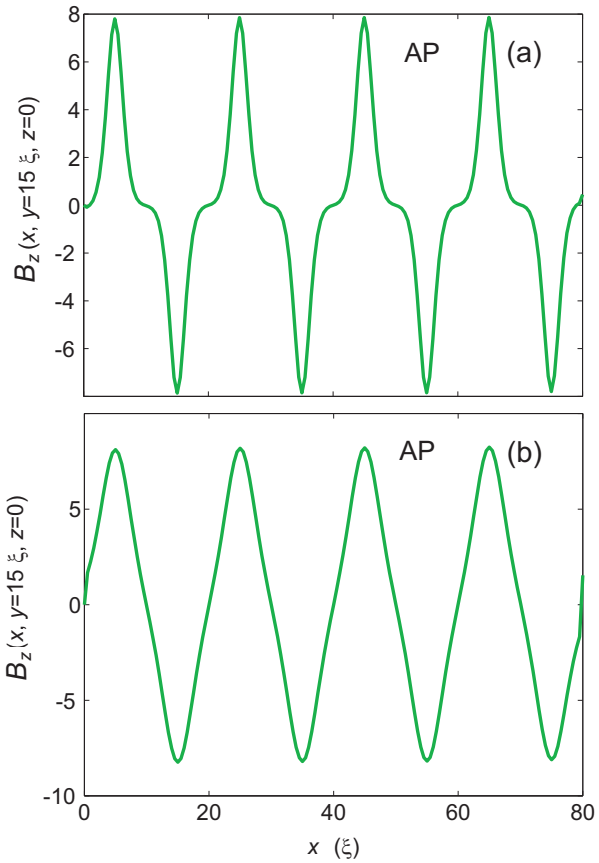

Figure 4.4: (Color online) The profiles of the magnetic field in the film, depending on the magnetic momentum and the height: a) $\mu_z = 8\mu_0$, $z = 5.6\xi$; b) $\mu_z = 64\mu_0$, $z = 11.2\xi$ (the profile of the magnetic field for $\mu_z = 1\mu_0$, $z = 2.8\xi$ is shown in Fig. 4.3(a)). Although $B_z = 2\mu_z/z^3$ is constant; the profiles are different.

nitude and phase of the order parameter: $\psi|_0 = \psi|_N$, $\varphi|_0 = \varphi|_N$, and in the y-direction we employ the "normal metal-superconductor" boundary conditions: $\psi = 0$, $\partial\varphi/\partial n = -j_n$. The current is applied along the y-axis as shown in Fig. 4.2. We define the critical "depinning" current j_c as the current resulting in non-zero vortex velocity in the dynamic regime. Typical value of the critical voltage (which corresponds to the threshold voltage to determine the critical depinning current) corresponds to $2.0 \times 10^{-4} V_0$.

Numerical solution of the TDGL equations is obtained using the finite-difference method, the Fourier analysis and the cyclic reduction method (FACR) [27, 63, 64].

4.3 Magnetic field profile of an array of out-of-plane dipoles

Let us first consider the central region of the sample limited by dashed lines in Figs. 4.2(a) and (b). This region contains one "channel" with a modulated magnetic-field profile. We assume that magnetic bars are long, narrow (∼1D) and

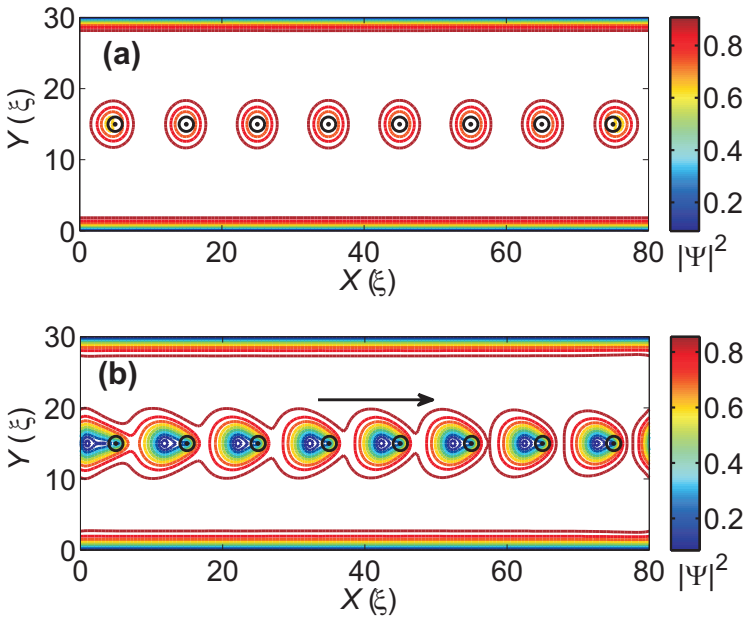

Figure 4.5: (Color online) (a) The vortex structure at the initial state (without a driving current). (b) A snapshot of moving antivortices in the film with parallel magnetic dipoles (indicated by black circles with dots in the middle). All antivortices move to one direction indicated by arrow. The magnetic dipole moment is $\mu = 1\mu_0$ and the height $z = 2.8\xi$ above the SC.

well-separated. These magnetic bars induce local and non-overlapping regions of depleted order parameter.

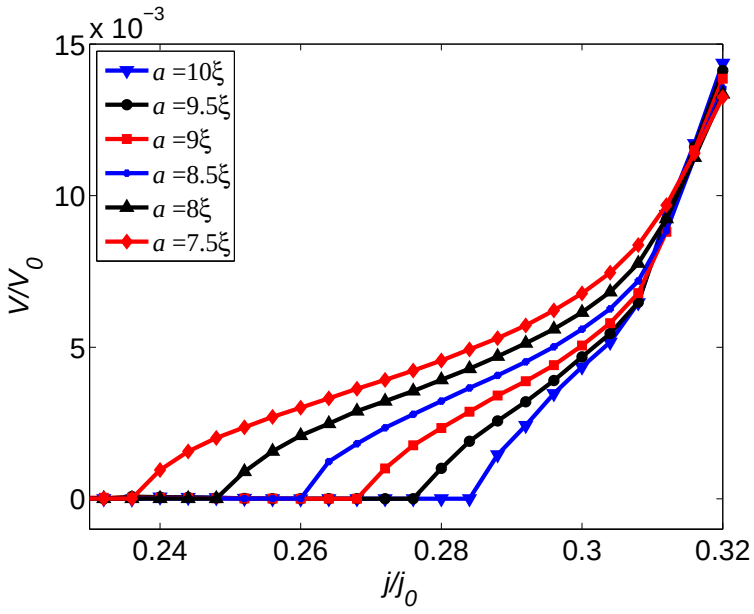

Figure 4.6: (Color online) The IV-curves for various distances a between the magnetic bars with $\mu = 1\mu_0$ and $z = 2.8\xi$.

A contour plot of the order parameter for a single chain of eight dipoles in the equilibrium state will be discussed Sec. 4.4B, see Fig. 4.7(a). In the absence of applied current, the equilibrium state is a set of pinned (anti)vortices under the magnetic tips of the bars. The stray magnetic field profile for the set of bars is represented in Fig. 4.3. The orientation of the equilibrium magnetization of the bars results in two significantly different magnetic profiles. We will show that one of them leads to the *flux-flow* vortex-motion regime and the other one results in the *pinned* regime with a larger critical current.

Let us have a closer look at the magnetic field profile of a single dipole versus the height and the magnetic moment. The vector-potential of the out-of-plane dipole magnetic field is as follows:

$$\boldsymbol{A_\mu} = \boldsymbol{e_x}\left(-\frac{\mu_z y}{r^3}\right) + \boldsymbol{e_y}\frac{\mu_z x}{r^3},$$

where μ_z denotes the magnitude of the magnetic moment in the z-direction (normal to the film surface) and scaled in units of $\mu_o = 5.6\frac{\Phi_0\xi}{8\pi}$. The corresponding magnetic field is as follows:

$$\boldsymbol{B} = \boldsymbol{e_x}\left(-\frac{\partial A_y}{\partial z}\right) + \boldsymbol{e_y}\frac{\partial A_x}{\partial z} + \boldsymbol{e_z}\left(\frac{\partial A_y}{\partial x} - \frac{\partial A_x}{\partial y}\right).$$

The out-of-plane component of the magnetic field has a larger impact on the order parameter in the SC film, and therefore we may neglect the in-plane magnetic field. The out-of-plane component is: $B_z = \mu_z(2z^2 - x^2 - y^2)/r^5$, where $r = \sqrt{x^2 + y^2 + z^2}$. Therefore, we have to take into account only the two components of the vector-potential, i.e., A_x, A_y. The maximum value of the magnetic field of the out-of-plane dipole is related to the dipole height and the magnetic moment magnitude (at $x = 0, y = 0$) as follows: $B_z = 2\mu_z/z^3$. Despite the fact that the maximum of the magnetic field is the same for any dipole orientation, the profile of the magnetic field will be significantly different. We will see that the modification of the dipole parameters changes the v-av dynamic regime in the film. Magnetic field profiles for various values of μ and z are shown in Figs. 4.3, 4.4.

As one can see from the figures, large magnetic moment and large z result in a broad profile. For a single separate dipole, the maximum of the magnetic field defines the maximum dipole *pinning force*. However, a set of equidistant dipoles might have a different pinning force due to the overlap of the magnetic field profiles of single dipoles.

4.4 Flux-flow and pinning regimes

4.4.1 Parallel array

In the parallel configuration, vortices are generated in the superconducting film right under the magnetic bar tips which are modeled by out-of-plane dipoles. The magnetic-field profile of an out-of-plane dipole may vary in magnitude and width, depending on the strength of the dipole and its separation from the sample z. If the

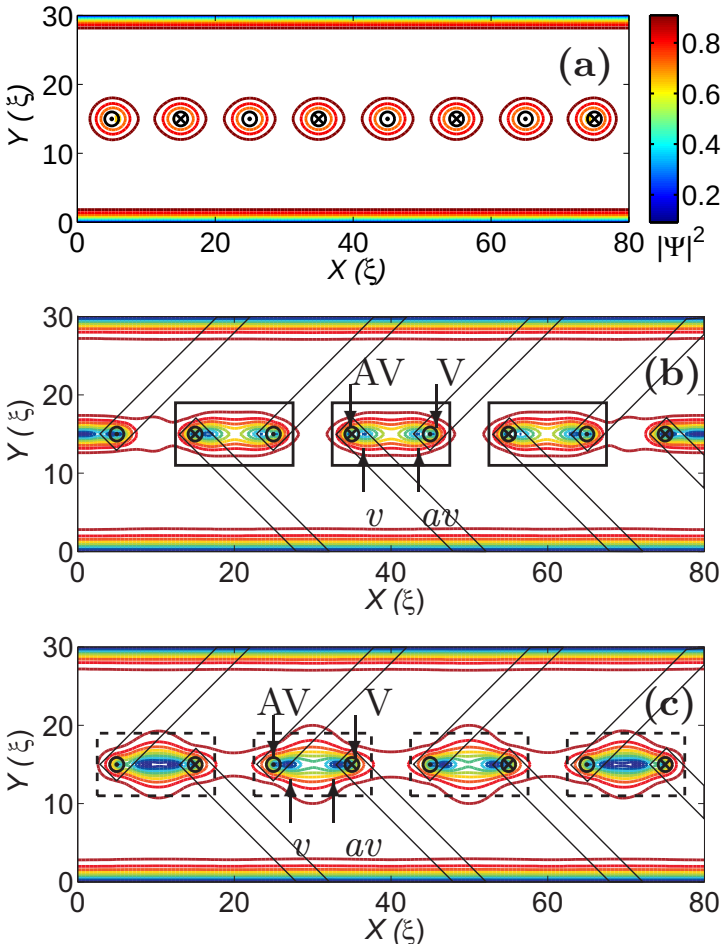

Figure 4.7: (Color online) Snapshots of the square modulus of the order parameter at 50 τ_{GL} illustrating the vortex dynamics in the film with antiparallel dipoles. The equilibrium state (a): no vortex motion. The circled dots and circled crosses show the direction of the magnetic dipoles at the bar tips. The symbols v, av show the vortices and antivortices that move and annihilate, while V, AV mark the remaining vortex/antivortex. The panels (b) and (c) show two characteristic regimes of the annihilation between neighboring out-of-plane dipoles.

produced field is larger than some critical value, the field generates (anti)vortices around the dipole (satellite vortices) and not just under its tip.

A typical value of the magnetic moment μ_z for typical distances $z = 2.8\xi$ used in this work is μ_0. This magnetic moment value does not produce satellite (anti)vortices, as shown in Fig. 4.5. Vortices are generated under the magnetic dipoles. In order to investigate vortex motion, we apply a driving current $j = 0.32j_0$, which leads to a flux creep along the dipole chain (see Fig. 4.5).

When the magnetic moment is larger than μ_0 and there are satellite vortices, the v-av dynamics becomes more complicated. Vortices and antivortices move and annihilate in between the dipoles. At the current magnitude of $0.25j_0$, the satellite vortices move slower than the vortices that hop between the pinning sites. With further increase of the transport current, e.g., for $j = 0.3j_0$, the flux-flow

occurs mainly via the "channel" with pinning sites. For the opposite polarity of the dipoles, the flow direction is reversed. This is due to the fact that vortices turn to antivortices and vice versa. The direction of the vortex (and, correspondingly, antivortex) motion will be opposite.

When we change the distance a from 7.5ξ to 10ξ between the dipoles, we observe a change in the IV curve (Fig. 4.6). Thus increasing a results in an increase of the critical current from $0.23j_0$ to $0.285j_0$. This increase of j_c can be explained as follows. The magnetic field of the dipoles depletes the order parameter under the dipoles. This local inhomogeneity of the order parameter serves as a vortex nucleation point. This suppressed order parameter region pins free vortices. Placing dipoles close to each other we create a "channel" (rather than a chain of separate localized minima) of depleted order parameter regions. Therefore, the dipoles that are closer to each other lead to an enhanced motion of the vortex from one pinning center to the other. It means that their mobility (along the row of the pinning centers) increases [39]. In the limit when the order parameter minima merge, the vortices move along the "path of the depleted order parameter". Due to the merging of the depleted order parameter regions, the critical current is smaller for closely-located dipoles and drops to zero when the "pinning sites" are close enough [39].

Therefore, the above analysis of the order parameter distribution and the IV-curves allows us to gain insight into the v-av dynamics of the system and to understand the observed dependence of the critical current j_c on the geometry of the system.

4.4.2 Antiparallel array

An antiparallel configuration of bars is shown in Fig. 4.2(a). The direction of the magnetic field near the tips of the neighbouring bars is opposite and we do not find any satellite vortices for various μ. This is explained by the fact that the antisymmteric field distribution in the vicinity of the bars mutually cancel out for any value of the magnetization μ (Fig. 4.4(b)). In the presence of the transport current, vortices move in the middle of the film.

In this regime, the flux carrying mechanism is different from the previous one and, as a result, the v-av dynamics becomes much more complicated. Under each tip of a magnetic bar, a vortex and an antivortex are generated. A vortex of one out-of-plane (up) dipole tends to annihilate with an antivortex of another out-of-plane (down) dipole. However, there are also an antivortex left under the out-of-plane (up) dipole and a vortex under another (down) dipole. They annihilate in the neighbor unit of the dipole chain. Each unit contains regions under two neighbouring tips, as shown in Fig. 4.7 by solid and dashed boxes. Vortex-antivortex annihilation occurs first in the central unit (solid box), then in two neighbor units (dashed boxes) and so on (toward the film boundary). This v-av dynamics includes two phases: the first one is the annihilation of v-av pairs in the solid boxes and the second in the dashed boxes, then the process repeats periodically. The v-av creation and annihilation dynamics can be presented as a subsequent alternation of the phases shown in Figs. 4.7(b) and 4.7(c). The (anti)vortices annihilate in

the central unit then they annihilate between neighbor dipoles of another unit (as a "chain"), then the process repeats. This v-av repeating processes result in two directed flows: vortex flow from the left to the right and antivortex flow from the right to the left.

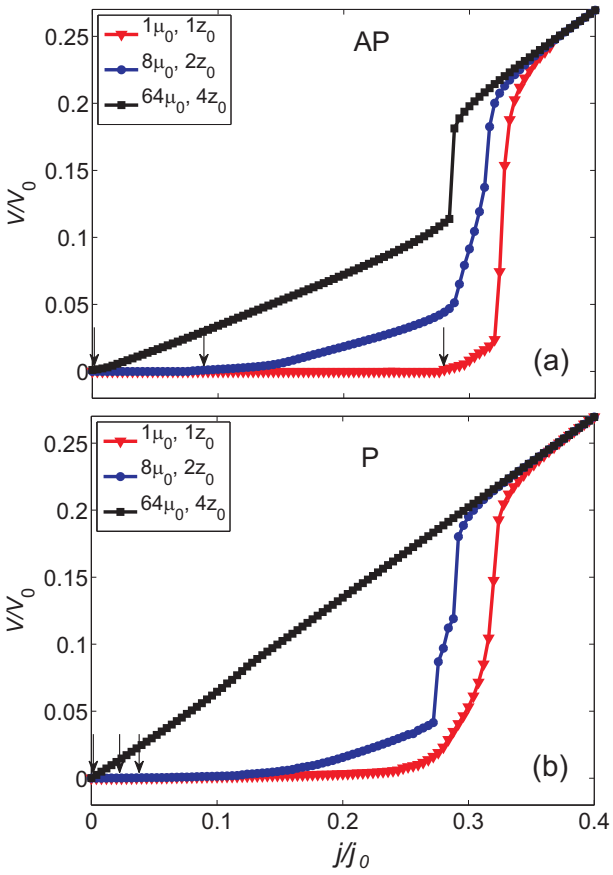

Figure 4.8: (Color online) (a) The IV-curves for an antiparallel dipole chain for: $\mu = 1\mu_0$, $z = 1z_0$; $\mu = 8\mu_0$, $z = 2z_0$; $\mu = 64\mu_0$, $z = 4z_0$. The critical currents j_c (shown by small arrows) are: $0.276j_0$, $0.077j_0$, $0.0j_0$ correspondingly. (b) The IV-curve for the parallel dipole chain. The critical currents j_c are: $0.039j_0$, $0.026j_0$, $10^{-4}j_0$ correspondingly. Here $\mu_o = 5.6\Phi_0\xi/8\pi$ and $z_0 = 2.8\xi$.

We have examined the influence of the length of the system on the critical current j_c. We found that if we change the distance between the dipoles, and keep the length of the film constant, then the critical current will be changed. The IV-curve for an antiparallel dipole chain reveals a larger critical current than that for the parallel dipole configuration. The strength of "pinning" of (anti)vortices is defined by the depth of the magnetic-field profile. This is explained by different potential profiles induced by parallel and antiparallel out-of-plane dipoles. Clearly the pinning strength is larger in case of AP dipoles and therefore, antiparallel array of dipoles trap vortices stronger. The critical current and the IV-curve depends on the profile of the dipole magnetic field. The broader the profile of the dipole magnetic field, the lower the critical current. The v-av dynamics is also strongly affected by this profile. One can see this difference in Fig. 4.8: different curves

correspond to various dipole magnetic moment and separation z. One can clearly distinguish flux-flow and pinned regimes when analyzing the IV-curves shown in Fig 4.8. The weak and low out-of-plane dipole (i.e., for small z) facilitates the pinned regime and results in larger critical current. Despite the fact that the magnetization of the dipoles is weak, their magnetic field is localized and results in narrow pinning centers. A strong dipole with a large z is characterized by a broad profile and favors the flux-flow regime: the region of depleted order parameter is large and the vortex is therefore not localized. This gives rise to a large vortex mobility which in turn results in a flux-flow regime.

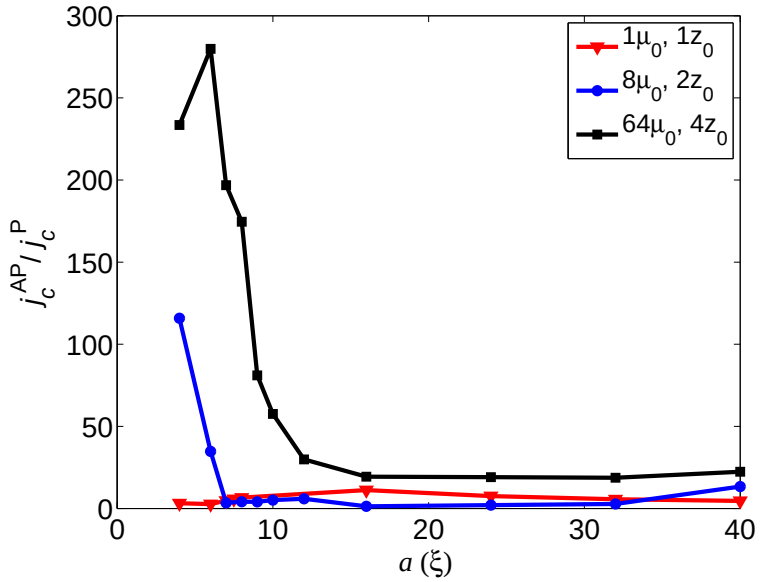

Figure 4.9: (Color online) The ratio of critical currents in the flux-flow and pinned regimes $j_c^{\mathrm{AP}}/j_c^{\mathrm{P}}$, versus the distance a between the rows of parallel magnetic bars. The legend shows the magnetization of the bars and its height above the SC, z.

We have shown that depending on the initial magnetization, the critical current varies in a broad range of j_c (see Fig. 4.8). It is interesting and desirable, from the point of view of possible applications, to optimize the critical current j_c and thus the performance of our device, i.e., the ratio between the critical current for parallel and antiparallel configurations.

Now we will focus on the selection of the system with the *highest* critical current in the flux-flow and pinned regimes. Optimization includes finding a system with the largest ratio of the critical currents. For this purpose, we introduce the "quality-factor" of the pinning array, i.e., the ratio of the critical current in the pinned regime (AP configuration), to that in the flux-flow regime (P configuration), $j_c^{\mathrm{AP}}/j_c^{\mathrm{P}}$ of the system which is plotted in Fig. 4.9 versus the distance a between the rows of parallel bar (see Fig. 4.2). The ratio between the critical current in the pinned and flux-flow regime depends on the distance between the magnetic bars a and on the magnetic field produced by the bars. The magnetic field profile of the bar depends on the ratio of the bar magnetization to the height of the bar above the SC surface. We discussed these parameters in Section 4.3. Fig. 4.9 shows that the ratio $j_c^{\mathrm{AP}}/j_c^{\mathrm{P}}$ changes with varying distance between the bars: it

reaches a maximum value for some bar magnetization ($\mu = 1\mu_0$ and $z = 2.8\xi$) or diverges (for $j_c^{\mathrm{P}} = 0$). This is due to the significant critical current drop (in the flux-flow regime) which happens for large magnetization values. However, the critical current (in the pinned regime) remains the same, but the ratio of these critical currents increases.

4.5 An array of wide magnetic bars

In this section, we consider an array of magnetic bars of finite width. The latter means that it is no longer possible to model the bars by out-of-plane dipoles, and we calculate the magnetic field profile of the in-plane bars. On the other hand, it is clear that it is the out-of-plane component of the magnetization that is responsible for the generation of (anti)vortices and their "pinning". However, in this case the regions of suppressed order parameter become rather extended, as compared to the case of narrow bars. A typical bar arrangement with separation parameters D_x, D_y is shown in Fig. 4.10. The modeled in-plane magnetized bars are shown by black and red (gray) dotted areas. Each bar is modeled by 96 elementary in-plane magnetized dipoles. This corresponds to the sizes: length $\approx 22\xi$, width $\approx 4.2\xi$.

The order parameter plots and the corresponding bar configurations are shown in the insets of Fig. 4.11 for the P and AP configurations. The magnetic field outside the SC film area is also taken into account. This magnetic field influences the (anti)vortices in the film. It turns out that there are less vortices for the AP configuration than for the P configuration in the film for the same bar configuration resulting in a smaller resistance and larger critical current.

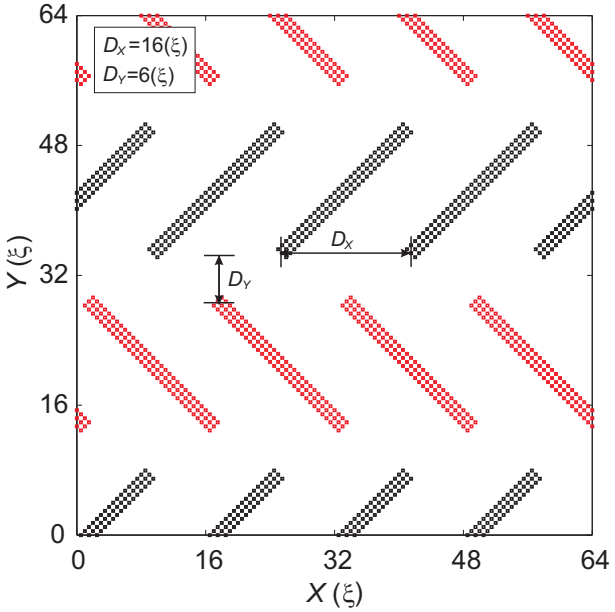

Figure 4.10: (Color online) One of the typical magnetic bar configurations. The distances between the bars in the x- and y-directions are $D_x = 16\xi$ and $D_y = 6\xi$, correspondingly. The sizes of the bars are: length $\approx 22\xi$, width $\approx 2.1\xi$.

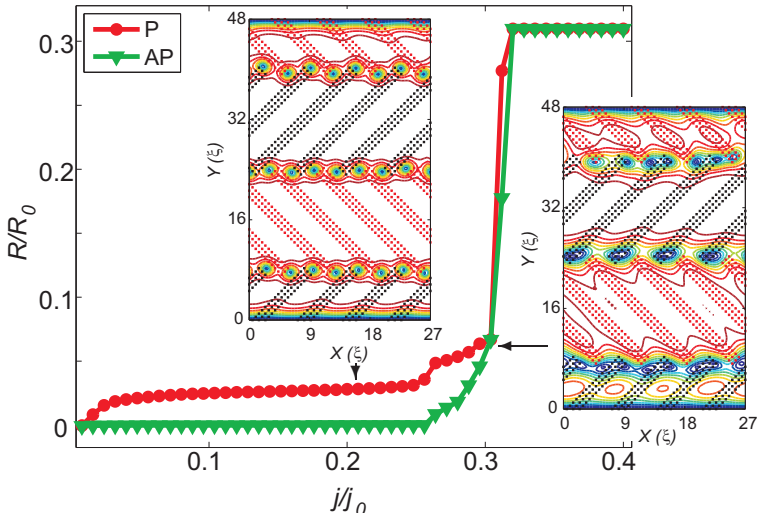

Figure 4.11: (Color online) The IV-curves for the parallel (P) and the antiparallel (AP) dipole configurations. The insets show snapshots of the order parameter in the stationary dynamic regime for AP (right bottom) and P (left top) magnetic configuration, for $j/j_0 = 0.21$ (P) and $j/j_0 = 0.31$ (AP). The modeled bars are shown by black and red (gray) dotted areas.

It was found that for relatively large distances between the magnetic bars, a vortex attached to one magnetic bar annihilates with an antivortex of the neighboring bar. There is no v-av motion present between the rows, but only inside the rows. For small spacing between the bars, the situation is more complicated: the trajectories of motion of vortices and antivortices overlap and it is difficult to distinguish vortex (antivortex) cores in order to investigate their dynamics.

In Fig. 4.12 we show a set of the IV-curves for parallel (a) and antiparallel (b) bar magnetization for varying distance D_x between the bars. The main feature of the IV-curves is that the critical current for the AP configuration is larger than that for the P configuration, for the same D_x and D_y. This result is in agreement with recent experimental results [84]. However, the ratio $j_c^{\mathrm{AP}}/j_c^{\mathrm{P}}$, which is the measure of the difference between the critical current in AP and P configurations, can be further improved through the adjustment of the distance between the bars on the film surface in the xy-plane.

4.5.1 Critical current behavior in the parallel configuration

Our calculations show that with increasing the separation between bars either in the x-direction, D_x, or in the y-direction, D_y, the critical current in the P configuration increases monotonically (see Figs. 4.12(a) and 4.13). When D_x increases (and D_y is constant), the area of unperturbed order parameter is enlarged. This can be easily understood intuitively: for smaller density of pinnig centers the order parameter in the film is less suppressed by the magnetic field, and (anti)vortices cannot easily jump from one pinning center to another one. This leads to an

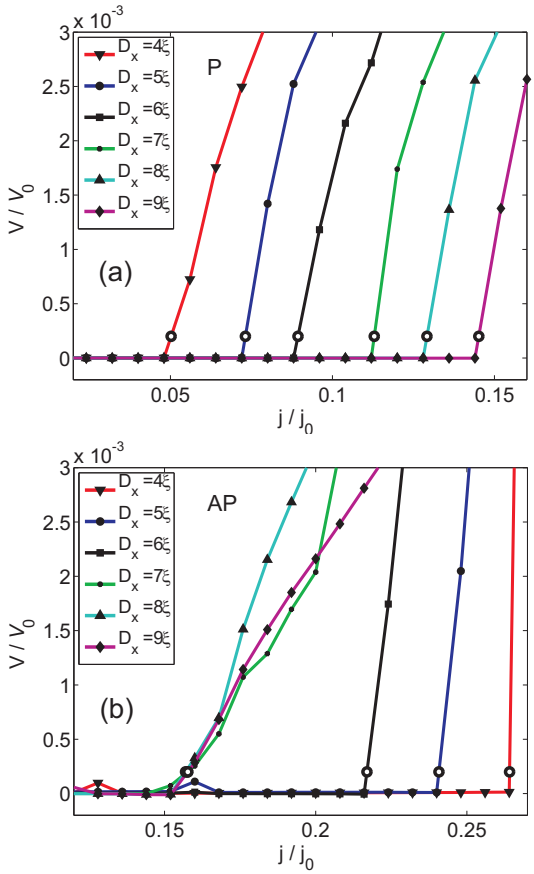

Figure 4.12: (Color online) The IV-curves for parallel (a) and antiparallel (b) configuration. The distance between the bar centers is presented in the legend and $D_y = 4\xi$.

increase in j_c.

Increasing D_y, while keeping D_x constant, also leads to increase of the critical current. However, for large enough D_y ($D_y > 10\xi$), vortices will move along two independent rows of pinning sites (separated by D_y), and further increase of D_y will not influence the v-av dynamics and j_c.

Analyzing the behavior of the critical current j_c when simultaneously changing D_x and D_y, we found that j_c can be effectively controlled in this device. Fig. 4.14 shows typical IV-curves for varying D_x and D_y. One can see from this plot that the difference in the critical currents for P and AP configurations can be controlled in a broad range, from an order of magnitude difference (Fig. 4.14(a)) to zero (Fig. 4.14(c)).

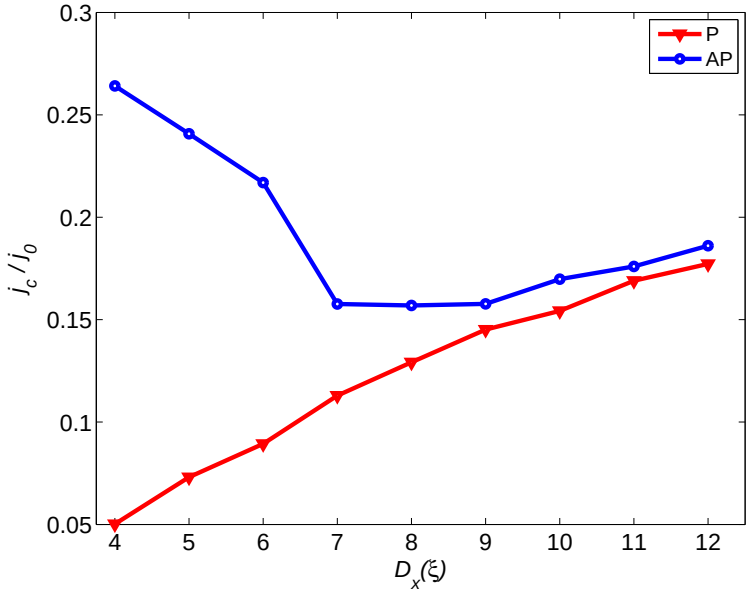

Figure 4.13: (Color online) The critical current j_c^{AP} and j_c^{P} as function of the distance between the magnetic bars D_x ($D_y = 4\xi$).

4.5.2 Critical current behavior in the antiparallel configuration

The dependence of the critical current on the distance between the bars for the AP configuration is more complex than that for the P configuration. The magnetic field of the neighbouring bars cancels each other partially for small D_x and D_y. While the critical current as a function of D_x still increases for $D_x > 7\xi$, similarly to the case of the P configuration, it shows a non-monotonic behavior for small D_x (see Fig. 4.13). The revealed increase of j_c for small D_x in the AP configuration is due to the annihilation of v-av pairs for strongly overlapping magnetic profiles of opposite polarity (see also Ref. [87]).

Increasing the separation between the pinning sites in the x-direction (D_x) leads to an increase of the depth of the magnetic-field profile, due to the decreasing overlap between the local magnetic fields of opposite polarity created by the magnetic bars. As a result, the critical current j_c as a function of D_x increases for $7\xi < D_x < 12\xi$ (see Fig. 4.13). For even larger D_x, the depth of the magnetic-field profile does not change and the function $j_c^{\mathrm{AP}}(D_x)$ saturates (see Fig. 4.13).

Using the obtained results for the critical current for the P and AP configurations we have also analyzed the ratio $j_c^{\mathrm{AP}}/j_c^{\mathrm{P}}$ in the plane ($D_x D_y$). The result is shown in Fig. 4.15. The maximal value of $j_c^{\mathrm{AP}}/j_c^{\mathrm{P}}$ is reached for closely spaced bars. For other limiting cases (small D_x and large D_y; large D_x and small D_y; large D_y and large D_x) the ratio $j_c^{\mathrm{AP}}/j_c^{\mathrm{P}}$ tends to unity.

This result ($j_c^{\mathrm{AP}}/j_c^{\mathrm{P}} \to 1$) can be understood in case of well-separated bars (e.g., $D_x > 6\xi$ and $D_y > 4.5\xi$). Due to the fact that the vortex (antivortex) paths do not overlap for large D_y (see Fig. 4.16), there are equal numbers of (anti)vortex paths in the long (in the y-direction) film with either P or AP configuration.

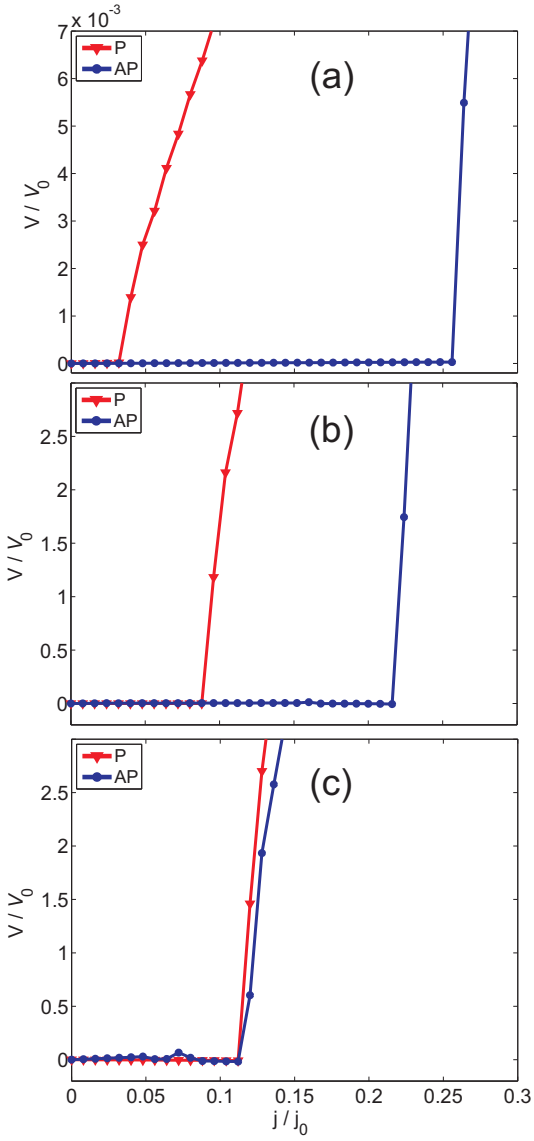

Figure 4.14: (Color online) The IV-curves for parallel (P) and antiparallel (AP) dipole configuration. The distance between the bar centers is (a) $D_x = 4\xi$, $D_y = 0\xi$; (b) $D_x = 6\xi$ and $D_y = 4\xi$; (c) $D_x = 7\xi$, $D_y = 0\xi$.

The difference in the vortex flows of the AP and P configurations is situated in the vortex and antivortex flows in the neighbouring paths: in one configuration (P) there are moving vortices in both paths and in the other configuration (AP) — vortices in one path and antivortices in another one. Therefore, in the AP configuration there are two counter-flows in neighbouring paths: one consisting of vortices and another one of antivortices. The number of moving vortices and antivortices in every path is equal. It means that the counter-flow in one path generates an equal voltage as the flow in neighbouring paths. It is clear that the critical currents of these two configurations will be the same.

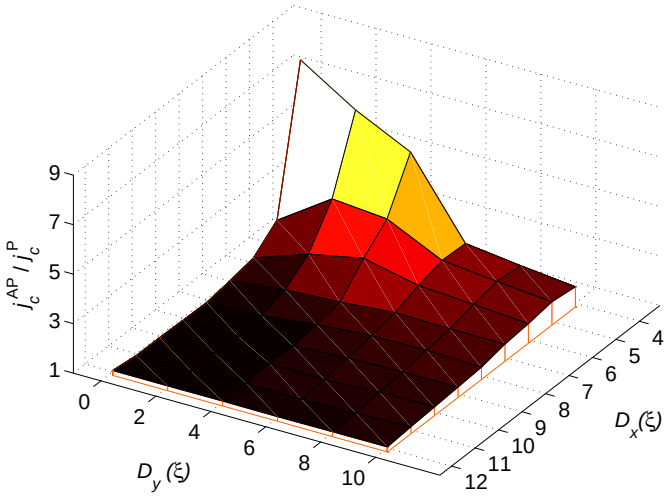

Figure 4.15: (Color online) The map of the ratio $j_c^{\mathrm{AP}}/j_c^{\mathrm{P}}$ as function of the distances between the magnetic bars.

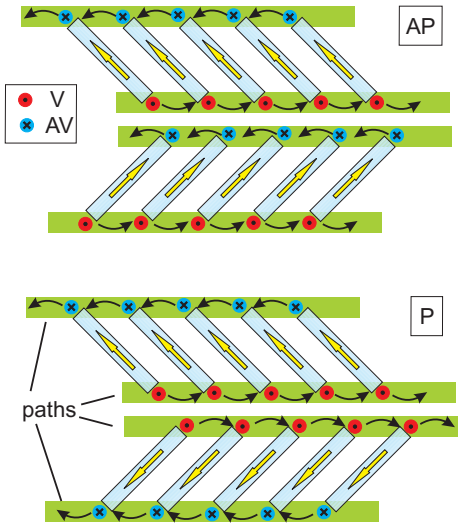

Figure 4.16: (Color online) Two nearest vortex (antivortex) paths in AP and P configuration. It illustrates the equal critical currents for the two configurations in a long (in the y-direction) film.

4.6 Conclusions

Using the time-dependent Ginzburg-Landau equations, we have investigated the vortex-antivortex dynamics in a hybrid system consisting of a superconducting film with an array of magnetic bars on top as was recently realized experimentally in Refs. [84, 59]. In the plane of the film, the magnetic bars form parallel rows of bars oriented perpendicular with respect to the bars in the adjacent row, i.e., they are arranged in a "zigzag" configuration.

The striking property of this zigzag array is that, by changing the magnetiza-

tion of the magnetic bars by applying an in-plane magnetic field, the configuration of the magnetic field can be switched from "parallel" to "anti-parallel", i.e., when the apices of the neighboring bars in the rows are magnetized either in the same or in the opposite direction. This switch of the magnetic-field configuration has a dramatic impact on the dynamics of the vortex-antivortex motion in the system and the mechanism of the flux transfer. We consequently simulated the system with out-of-plane dipoles (i.e., for narrow bars) and in-plane dipoles (for wider bars). The results are consistent with each other and lead to the same conclusions. The parallel configuration is characterized by a dense and shallow potential profile which favors the flux-flow regime having low critical currents. Contrary to that, the anti-parallel configuration is characterized by a relatively deep and less dense potential profile resulting in a flux-pinned regime with a high critical current. While this main result is easily understandable, and our results agree with recent experimental observations in Refs. [84, 59], the mechanisms behind the flux transfer and the detailed vortex-antivortex dynamics is rather complicated in this system. As we demonstrated, it involves the process of vortex-antivortex generation under the tips of the bars (or in the vicinity to the bars) and their annihilation, which is strongly affected by the system parameters such as the magnetization of the bars, the spacing between the bars in the plane of the superconductor and the spacing between the bars and the superconductor. Using the results of calculations and understanding of the different underlying mechanisms of flux transfer, one can improve the performance of this artificial device, i.e., to increase the ratio of the critical currents for the two distinct in-plane magnetizations: parallel and antiparallel, $j_c^{\mathrm{AP}}/j_c^{\mathrm{P}}$, by using the zigzag-arranged magnetic bars which can be useful for magnetic flux manipulation in fluxonics applications.

Chapter 5

Vortex transport in a diamond-cell channel

By numerically solving the time-dependent Ginzburg-Landau equations in a type-II superconductor, characterized by a critical temperature T_{c1}, with a channel formed by overlapping rhombuses (diamond-like channel) made of another type-II superconductor, characterized by a higher critical temperature, T_{c2}, we investigate the dynamics of driven vortex matter for varying parameters of the channel: the width of the neck connecting the diamond cells, the cell geometry, and the ratio between the coherence lengths in the bank and the channel. We analyzed infinite and finite-size samples, and we found that by tuning the channel parameters, one can manipulate the vortex dynamics, e.g., change the transition from flux-pinned to flux-flow regime and tune the slope of the IV-curves. In addition, we analyzed the effect of interstitial vortices on these characteristics. The critical current of this device was studied as a function of the applied magnetic field, $j_c(H)$. The function $j_c(H)$ reveals a striking commensurability peak, in agreement with recent experimental observations. The obtained results suggest that the diamond channel, that combines the properties of pinning arrays and flux-guiding channels, can be a promising candidate for potential use in devices controlling magnetic flux motion.

The results of this chapter are summarized in Ref. [88].

5.1 Introduction

According to the well-known Bean's model [89], the critical current $j_c(H)$ is the maximum current a superconductor can carry without dissipation. This dissipation is caused by vortex motion. Therefore, in order to increase the critical current, vortices should be either immobilized (i.e., pinned) or removed from the active area of a superconducting device. The former can be achieved by using various artificial pinning arrays including regular pinning arrays, e.g., square and triangular arrays of sub-μm holes (antidots) [35, 36, 37, 38, 39] or sub-μm Ni triangles on top of Si substrate [41] or more advanced blind antidots (i.e., holes which partially perforate the film to a certain depth) [42] and pinning arrays with field-dependent pinning strength [43]. Even a few individual pinning sites arranged at proper positions can be very efficient in trapping undesired vortices. For example, it was demon-

strated [90] that the low-frequency noise due to vortex motion in high-temperature superconducting quantum interference devices (SQUIDs) can be strongly reduced by a "strategic" arrangement of antidots patterned into the SQUID. Alternatively, it was recently proposed to use aperiodic pinning arrays instead of periodic arrays. Despite the fact that they are incommensurate with the (ideal) vortex lattice, these pinning arrays were proven to be even more efficient in magnetic flux pinning than regular arrays. The enhancement of the pinning strength in a broad range of magnetic fields is provided by elastic deformation of a vortex lattice, as was recently demonstrated theoretically [91, 92] and experimentally [93, 94, 95, 96] for quasiperiodic Penrose-tiling pinning arrays.

Another efficient method of the critical current control in superconducting nano- and micro-devices is to remove magnetic flux from the active area of the device. For this purpose, it was proposed to use various realizations of vortex ratchets, e.g., fluxon pumps and lenses [77] using a "funnel" channel [97, 98], voltage rectifiers [99], Josephson vortex ratchets [100]. Thus it was shown that vortex ratchets can be used for vortex removal (or significant reduce in number) from a superconductor [101, 76, 102, 103, 41, 104]. Also, the effect of the field history on the vortex dynamics in narrow ratchet channels was investigated [105]. It was shown that the edge barrier controls the critical current in a thin film of a weak-pinning superconductor [106] and in a similar system with periodic constrictions [107], see Fig. 5.1.

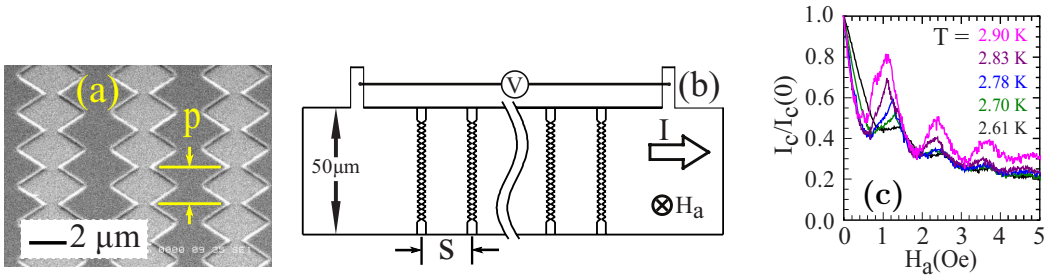

Figure 5.1: (a) Scanning electron micrograph of three channels with periodic diamond constrictions. (b) Strip layout, along with channel and magnetic field orientation. (c) Measurement of $I_c(H_a)$ for $p = 2\mu m$, $s = 20\mu m$, for different T as indicated, scaled by corresponding I_{c0} (after Ref. [107]).

In addition to vortex rectification, the motion of the magnetic flux can be controlled using vortex guidance effect [108, 39, 109, 110], which manifests itself in the flux motion along the symmetry directions of an array of pinning sites. It was shown [108] that the vortex lattice undergoes a series of locking transitions when increasing the applied driving force. As the vortex lattice passes through these phases, the transverse velocity component as a function of increasing transverse drive shows a series of plateaus which form a devil's staircase structure. Experimentally, controlled trapping and guided motion of vortices via special arrangements antidots in $YBa_2Cu_3O_7$ films was demonstrated using resistive Hall-type measurements. In contrast to conventional vortex motion due to vortex unpin-

ning at currents exceeding the critical current, this motion is present down to zero current and low temperatures and it is characterized by a linear voltage-current dependence, i.e., Ohmic behavior [39]. Magneto-optical imaging measurements of a $YBa_2Cu_3O_x$ film shaped as a long strip with perpendicular antidot arrays revealed [110] strong guidance of flux and large perturbations of the overall flux penetration and flow of current.

Recently, the effect of magnetic flux guidance in a hybrid superconductor magnetic-dot-array bilayer was theoretically analyzed, using Langevin-type molecular-dynamics simulations [57] and the time-dependent Ginzburg-Landau equations [33]. In particular, the vortex-antivortex dynamics was analyzed for different arrangements and magnetic moments of the dipoles, as a function of the angle between the direction of the magnetic dipole and that of the Lorentz force produced by the applied current. It was shown that the interplay of the attractive interaction between a vortex-antivortex pair and the Lorentz force resulted in either separation of (anti)vortices and their motion in opposite directions or to their annihilation. The guided motion effect was analyzed [33] in finite and in infinite samples. It was shown that in finite samples the magnetic dipole induced vortex-antivortex guidance is influenced by the self-interaction of the vortex-antivortex pairs with their images, while in a periodic array of dipoles the guidance is determined by the interaction of a vortex-antivortex pair with other dipoles and vortex-antivortex pairs created by them.

In this work, we investigate the vortex dynamics in a system consisting of a superconductor with a channel made of another superconductor. The channel is formed by compartments in shape of rhombuses ("diamonds") partially overlapped such that they form a continuous channel (in the limiting case, adjacent "diamonds" touch each other just at one point). Our choice of the channel geometry was motivated by the recent experiment [107] on vortex dynamics in channels with periodic constrictions. The authors measured the critical current J_c in diamond-cell channels and found reversible oscillations in J_c as a function of the applied magnetic field [107]. The goal of our study is the understanding of: (i) the dynamics of moving vortices in detail and (ii) the possibility of manipulating of this dynamics by tuning the geometric and material parameters of the channel (which is hardly accessible in experiments). We analyze the vortex dynamics in a diamond-cell channel from the point of view of pinning properties of the system and the possibility of manipulate the dynamical regimes (e.g., flux-pinned regime and flux-flow regime). As we show below, each individual compartment of the channel acts as a "soft pinning" site which is the key property of this system. The magnetic core of a vortex extends outside the channel, and by changing the degree of overlapping of the diamond cells (and thus the minimum width of the channel at the neck between neighboring compartments), one can manipulate the pinning strength. As we show in this work, this provides a flexible tool for controlling the dynamical regimes in this system. On the other hand, the diamond channel acts as a guiding "row of pinning sites" but appears to be more efficient than an array of separate pinning sites, due to the partial overlap of the pinning potentials created by each diamond cell. In this work, we investigate various dynamical regimes of vortex motion in a diamond channel, for varying material and geometric

parameters of the system. Note that a diamond channel was recently investigated experimentally in Ref. [107] which is an additional motivation to analyze the dynamics of this system in more detail.

To study the vortex dynamics, in this work we rely upon the time-dependent Ginzburg-Landau equations (TDGL) which take into account the influence of the cell confinement on the vortex motion. We investigate the equilibrium and transport properties of driven vortices. In particular, we study the flux motion in the diamond channel for different material parameters and geometries of the channel and calculate appropriate IV-curves and the critical current, $j_c(H)$, as a function of the applied magnetic field. We found that the critical current, $j_c(H)$, demonstrates striking commensurability effect, in agreement with the experimental observations [107]. Analyzing the IV-curves, we show that, by varying the material parameters (i.e., the ratio of the coherence lengths inside and outside the channel, ξ_2/ξ_1), the "gap" between the diamond cells (i.e., the minimum channel width, w) and the geometry of the cell, one can manipulate the dynamical regimes in the diamond channel, e.g., to switch between the flux-pinning and flux-flow regimes, and control the slope of the corresponding IV-curves.

The pinning properties of the system are related to the magnetic-core pinning. Despite the fact that the vortex core can be be very small (e.g., $\xi \sim 1-5$ nm in HTSC), its supercurrent spreads over a wide range ($\sim \lambda \gg \xi$). Therefore, if we construct a magnetic barrier with an opening w, such that $\lambda > w > \xi$ than the vortex interaction with the opening edges would lead to pinning. Also the opening w influences the surface barrier energy, which leads to a vortex generation for lower values of magnetic field (in finite-size samples). The diamond channel confines the vortex motion in the transverse (y-) direction. On the other hand, the modulation of the channel width introduces pinning in the x-direction. Our calculations show that by adjusting the ratio ξ_2/ξ_1 and the external magnetic field, one can maintain the necessary amount of vortices in the channel. This provides opportunities for studying the interaction between satellite (interstitial) vortices and vortices in the channel.

The paper is organized as follows. In Sec. 5.2 we introduce the model system. In Sec. 5.3, we describe the mechanism of vortex generation in the channel for two different system preparation regimes, i.e., field-cooled and zero-field-cooled regime, and we analyze equilibrium vortex states in finite and infinite systems. In Sec. 5.4, we discuss the results on the flux dynamics in the diamond channel, including the analysis of the IV-curves for varying material parameters and the channel geometry, the effect of commensurability observed in the critical current $j_c(H)$. The conclusions are presented in Sec. 5.5.

5.2 Model

Our system consists of a type-II SC film characterized by the coherence length ξ_1 with a channel formed by diamond-shape cells of another type-II SC with a larger coherence length ξ_2: $\xi_2 > \xi_1$. Our model channel is shown in Fig. 5.2. This configuration provides a vortex-flow channel with modulated width, so-called diamond-cell (or: diamond) channel. The ratio between the coherence lengths

in the channel and in the bank superconductor, ξ_2/ξ_1, is a variable parameter, typically taken as $\xi_2/\xi_1 = 6$. The bottleneck w (see Fig. 5.2) of the channel varies from 0 to 8 ξ_1. The ratio ξ_2/ξ_1 mainly controls the vortex mobility in the channel. By changing the width of the channel and the ratio ξ_2/ξ_1, we can manipulate the vortex motion inside it. An external homogeneous magnetic field generates vortices in the channel which are driven by an external transport current.

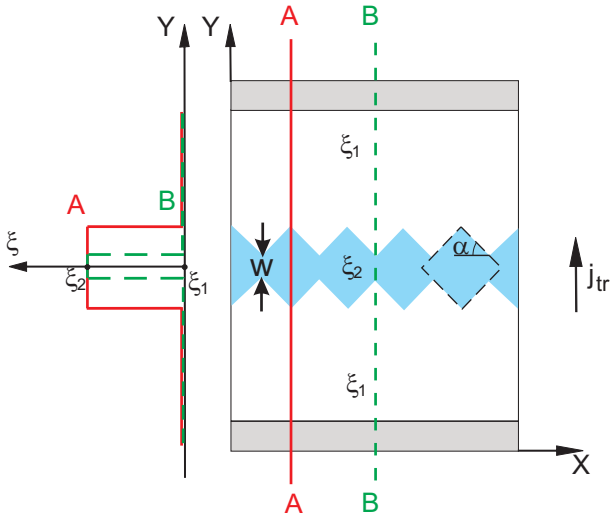

Figure 5.2: (Color online) Sketch of the model system. The "diamond channel" is filled by blue (gray). The channel is characterized by the coherence length ξ_2, while the main superconductor (bank) has ξ_1. The channel parameters (shown in the sketch) are: the ratio ξ_2/ξ_1, the minimum width of the channel, w, and the cell shape characterized by angle α.

We consider samples either finite or infinite in the x-direction. To model an infinite channel, we use periodic boundary conditions applied to the phase and the amplitude of the SC order parameter. In our simulations, we typically consider samples with dimensions $80\xi_1 \times 50\xi_1$ and $20\xi_1 \times 50\xi_1$, where ξ_1 is the superconducting coherence length at zero temperature T. We use the field-cooled regime (FC) and then (after some relaxation time) we turn the transport current on and investigate the vortex motion.

In order to avoid the influence of the metal leads on channel vortices and study the interaction of vortices in the channel with satellite vortices (i.e., out-of-channel), we set the boundaries of the film $\sim 30\xi_1$ away from the each side of the diamond channel (in the y-direction).Note that for when $\xi_2/\xi_1 = 1$ we observe the behavior typical for homogenous SC film.

After the initial vortex configuration in the system is prepared, the current is turned on, and we investigate the vortex-antivortex (v-av) dynamics. To study the dynamics of the v-av pairs, we employ the time-dependent Ginzburg-Landau equation [60, 61]:

$$u\left(\frac{\partial}{\partial t} + i\varphi\right)\psi = \xi_i(\nabla - \mathrm{i}\mathbf{A})^2\psi + (1 - |\psi|^2)\psi, \tag{5.1}$$

$$\xi_i = \begin{cases} \xi_1, & \text{in the bank SCs} \\ \xi_2, & \text{in the channel} \end{cases}$$

The default values are $\xi_2/\xi_1 = 6$ inside the diamond-channel and $\xi_2/\xi_1 = 1$ everywhere outside of it. The equation is to be solved self-consistently with the Poisson equation for the electrostatic potential,

$$\Delta\varphi \;=\; \mathrm{div}\left(\mathrm{Im}(\psi^*(\nabla - \mathrm{i}\mathbf{A})\psi)\right). \tag{5.2}$$

In Eqs. (1) and (2), all the physical quantities are expressed in dimensionless units: temperature T in units of the critical temperature T_c, the vector potential $\mathbf{A}$ in units $\Phi_0/(2\pi\xi(T))$ (where Φ_0 is the quantum of magnetic flux), the order parameter in units of $\Delta_0 = 4k_BT_cu^{1/2}/\pi(1-T/T_c)^{1/2}$, and the length in units of the coherence length $\xi(T) = (8k_BT_c/\pi\hbar D)^{-1/2}/(1-T/T_c)^{1/2}$. Using these units, the magnetic field is scaled by $H_{c2} = \Phi_0/2\pi\xi(T)^2$ and the current density by $j_0 = \sigma_n\hbar/2e\tau_{GL}(T)\xi(T)$. Time is scaled in units of the Ginzburg-Landau relaxation time $\tau_{GL}(T) = \pi\hbar/8k_BT_cu/(1-T/T_c)$, the electrostatic potential φ in units of $V_0 = \hbar/2e\tau_{GL}(T)$, where σ_n is the normal-state conductivity, and D is the diffusion constant. Parameter u governs the time change of $|\psi|$ and the length of penetration of the electric field into a superconductor [62]. Since we are interested mainly in the dynamics of (anti-)vortex motion but not in the time evolution of the v-av nucleation and annihilation, for our problem the actual value of u does not play an essential role, and we choose $u = 5.79$ (note that this value depends on the specific superconductor).

We assume that the thickness of the superconducting film d_s is smaller than the effective (normal) magnetic-field penetration depth, $\Lambda = \lambda(T)^2/d_s$, where d_s is the thickness of the sample, and therefore we can neglect the influence of the screening and transport currents on $\mathbf{A}$ [58].

For convenience, we shift the diamond channel to the left for a half of a diamond cell length in the x-direction. In this case, the first and the last cells are half-cells. This decreases the energy for vortex entry into the film and exit out in case of finite samples. It also stabilizes the vortex motion inside the channel (jamming in the last cell does not appear and does not force vortices to leave the channel). In case of infinite sample this trick does not play an essential role due to the periodic boundary condition.

In the x-direction we use periodic boundary conditions for the magnitude and phase of the order parameter: $\psi|_0 = \psi|_N$, $\varphi|_0 = \varphi|_N$, and in the y-direction we employ the "normal metal-superconductor" boundary conditions: $\psi = 0$, $\partial\varphi/\partial n = -j_n$. The current is applied along the y-axis as shown in Fig. 5.2. We define the critical "depinning" current j_c as the current resulting in non-zero vortex velocity in the dynamic regime. Typical value of the critical voltage corresponds to $1.0 \times 10^{-4}V_0$.

Numerical solution of the TDGL equations is obtained using the finite-difference method, the Fourier analysis and the cyclic reduction method (FACR) [27, 63, 64].

5.3 Equilibrium vortex states

In this section we describe the way how the initial state of the system is prepared. In our simulations, we mimic two experimental regimes for initial state preparation: field-cooled (FC) regime and zero-field-cooled (ZFC) regime [2]. In the former case, we start the simulation from the normal state and let the system to relax in the presence of a homogeneous magnetic field. The applied magnetic field generates vortices in the sample. In the latter case, the system is cooled down without field, and then the field penetrates the system through its boundary in form of vortices.

5.3.1 Finite samples

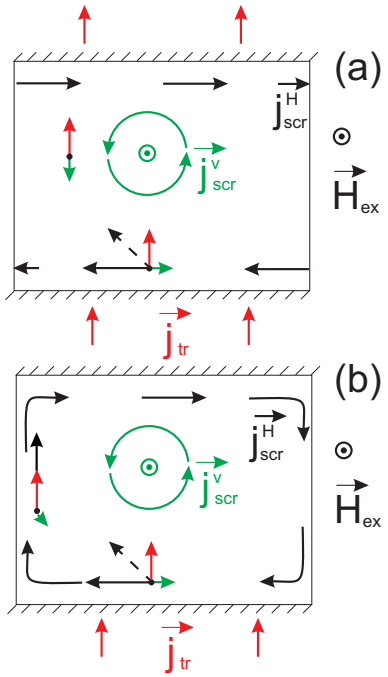

Figure 5.3: (Color online) Current distribution in an infinite (a) and finite (b) superconducting sample with a vortex inside. Solid black arrows represent the surface screening current, j^H_{scr}; solid red (dark grey) the transport current, j_c; solid green (light grey) the current of the vortex, j^v_{scr}. H shows the direcion of the external magnetic field (out-of-plane). The dashed-line vector shows the total current of the above three contributions at a point near the boundary (marked with a black dot).

Here we analyze equilibrium vortex states in finite samples obtained for various values of the external magnetic field. These states were obtained using ZFC regime. After the cooling down, vortices enter the sample through its boundaries. The mechanism of the current-assisted vortex entry is as follows. The total current (i.e., the geometric sum of the screening and the transport currents) near one of the boundaries becomes higher then depairing current (see Fig. 5.3). This lowers the surface barrier for vortex entry. An additional factor for the barrier decrease is the fact that the coherence length in the channel ξ_2 is larger than that outside

ξ_1. These two factors provide a condition for vortex entry. Each new vortex which enters the channel increases the barrier since its current lowers the total sum of the transport and the screening currents near the film edge (see Fig. 5.3(b)). Vortices will enter and occupy the channel until the vortex currents rise the barrier high enough, resulting in a balance between the flux outside and inside the sample (Fig. 5.4(a)). Due to the condition $\xi_2/\xi_1 > 1$, vortices will preferably occupy the channel rather than the bank. Therefore, the diamond channel serves as a *pinning channel*.

The excess of the flux which is not trapped by the channel, enters the bank (i.e., the superconductor with a lower coherence length $\xi_1 < \xi_2$) in form of additional (i.e., not "pinned") vortices. Figs. 5.4(b) and (c) represent equilibrium vortex states in the diamond channel for a larger external magnetic field than in case (a). Figures show that the vortices inside the channel impose the symmetry on the interstitial vortices (the situation is opposite to the one described in Ref. [107], where the interstitial vortices imposed the symmetry on the channel vortices). This is a direct consequence of the absence of the intrinsic pinning. At large magnetic field $H = 0.055H_{c2}$ (Fig. 5.4(c)), the interstitial vortices are tightly packed and the interaction among them overcomes the interaction with the channel vortices. This leads to the appearance of an Abrikosov-type lattice of interstitial vortices.

In mesoscopic SCs close to the normal state, the boundary conditions induce the order parameter to follow the symmetry imposed by the sample geometry as demonstrated, e.g., for mesoscopic disk [111, 112, 113, 114], triangles [115, 116], and stars [117]. It explains the absence of pure triangular vortex lattice outside of the diamond channel.

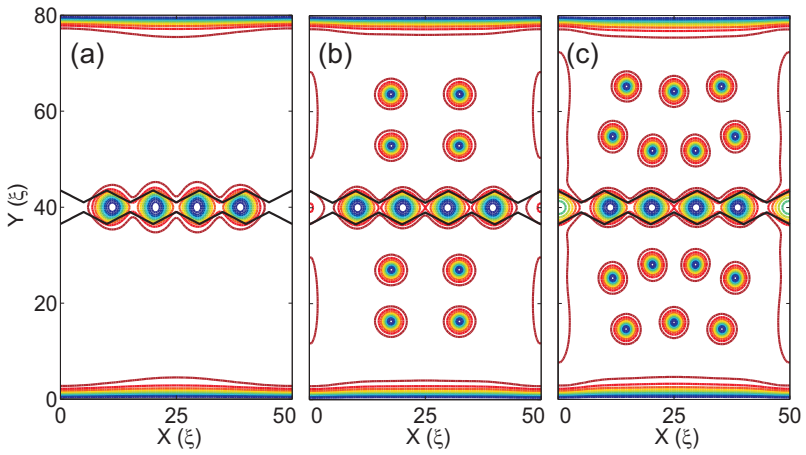

Figure 5.4: (Color online) Initial (static) vortex configurations (i.e., in absence of driving) in the sample ($w = 4\xi_1$ and $\xi_2/\xi_1 = 6$) for the external magnetic field: (a) $H = 0.022H_{c2}$; (b) $H = 0.04H_{c2}$; (c) $H = 0.055H_{c2}$.

In Fig. 5.5, we show equilibrium vortex states for varying ξ_2/ξ_1. The ratio ξ_2/ξ_1 governs the surface barrier for vortex entry into the diamond channel. The larger the ratio, the lower the barrier and the stronger the pinning inside each cell. For the same external magnetic field, a lower ξ_2/ξ_1 value (surface barrier) leads to a smaller total vortex number in the film and a weaker pinning leads to a smaller

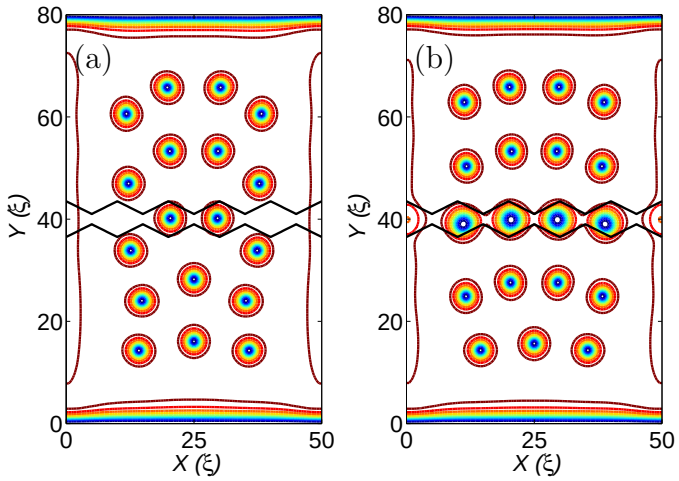

Figure 5.5: (Color online) Initial (static) vortex configurations (i.e., in absence of driving) in the sample ($w = 4\xi_1$ and $H = 0.055H_{c2}$) for the ratio of the coherence lengths: (a) $\xi_2/\xi_1 = 1$; (b) $\xi_2/\xi_1 = 3$;

vortex number in the channel itself.

These results show that, by varying ξ_2/ξ_1 one can manipulate the ratio of the vortex number in the channel and outside the channel. However, this manipulation is possible for rather high magnetic field ($H \gtrsim 0.03H_{c2}$) when the channel cannot trap all the vortices and they will penetrate outside of the channel and will vary the ratio between the channel and the interstitial vortices. For low magnetic field ($H \lesssim 0.03H_{c2}$), vortices occupy the channel until it traps them inside and no interstitial vortex appears. Analyzing the vortex dynamics in the diamond channel, we are interested in regimes when vortices are mainly trapped in the channel.

5.3.2 Infinite sample

Infinite samples are modelled by employing periodic boundary conditions in the x-direction of the simulation cell. Initial vortex configurations are prepared by simulating FC regime. Equilibrium vortex states in the diamond channel for various values of the external magnetic field are presented in Fig. 5.6. The corresponding current distribution is shown in Fig. 5.3(a). Note that the periodic boundary condition results in a more homogeneous vortex distribution in the x-direction than in finite-size samples.

In our simulations the vortex number in a stationary state does not depend on the ratio ξ_2/ξ_1 (as examined for $H = 0.01 - 0.1H_{c2}$). Despite this, ξ_2/ξ_1 becomes significant in the dynamical regime as it is included in the kinetic term of TDGL equations (5.1). Therefore, variation the ξ_2/ξ_1 governs the ratio between the vortex number in the channel and out of the channel in the dynamic regime.

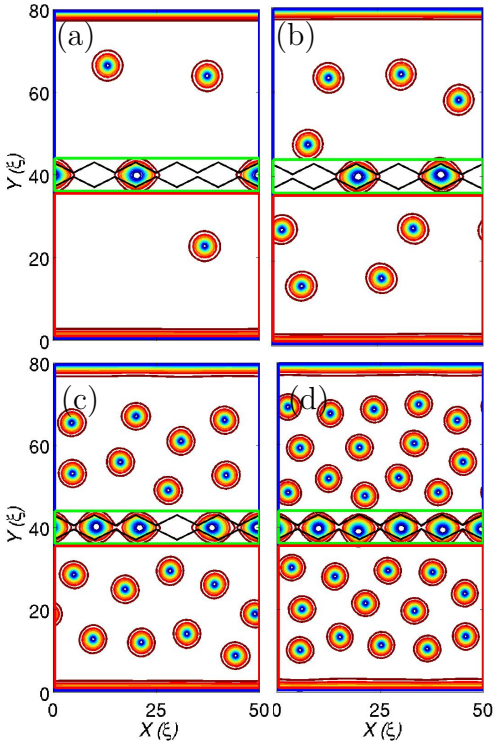

Figure 5.6: (Color online) Initial (static) vortex configurations (i.e., in absence of driving) in the sample ($w = 2\xi_1$ and $\xi_2/\xi_1 = 6$) for the external magnetic field: (a) $H = 0.01H_{c2}$; (b) $H = 0.02H_{c2}$; (c) $H = 0.04H_{c2}$; (d) $H = 0.06H_{c2}$.

5.4 Flux dynamics

In this section, we study the vortex dynamics driven by external current. As we demonstrated in the previous section, vortices can occupy either the channel area only (see Fig. 5.4(a)) or the channel and the bank area (Fig. 5.4(b,c)), depending on the applied magnetic field. Correspondingly, the dynamical behavior will differ for these two different cases.

For low magnetic fields, which correspond to the case when vortices occupy only the diamond channel, the motion of vortices occur in the form of a "single file", i.e., along a single straight-line trajectory inside the channel, following one another, without permutations. This motion can be controlled, as we show bellow, by the geometry of the channel.

For higher magnetic fields, which provide generation of vortices both in the channel and in the banks, the dynamical behavior is different. The contribution to the total vortex current will be provided by vortices moving inside the channel and interstitial vortices. Due to the difference in the material parameters, i.e., ξ_1 and ξ_2, the vortices in the channel move faster then interstitial vortices. However, the velocity of the vortices in the channel can be manipulated by changing the channel geometry which results in a variety of dynamical regimes. Examples of snapshots of moving vortices in the system, for magnetic field $H = 0.02H_{c2}$ and $\xi_2/\xi_1 = 6$, are shown in Fig. 5.7. It is interesting to note that, while in the initial state (without current) the vortex arrangement can be less ordered (Fig. 5.7(a)),

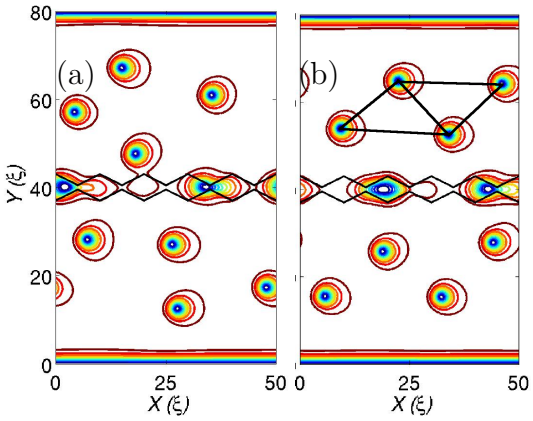

Figure 5.7: (Color online) Snapshots of driven vortex matter in a diamond channel in an infinite sample: ($\xi_2/\xi_1 = 6$, $w = 2\xi_1$) at times: (a) $t = 235\tau_{GL}$; (b) $t = 1515\tau_{GL}$. The external magnetic field is $H = 0.02H_{c2}$. The solid black lines, forming triangles, show the dynamically-ordered "lattice" of moving interstitial vortices.

the system of vortices becomes more ordered during the motion (Fig. 5.7(b)). This occurs due to the fact that channel vortices move faster than interstitial vortices, and after some time, the system adjusts itself to minimize its energy such that the interstitial vortices becomes more ordered (i.e., the dynamical ordering).

5.4.1 The IV-curves of the system

The above difference in the dynamical behavior of the system without (i.e., vortices are only in the channel) and with interstitial vortices is illustrated by the IV-curves.

In Fig. 5.8, we plot IV-curves for the channel vortices (Fig. 5.8(a); for convenience, we consider a narrow channel, i.e., with width $d_y = 20\xi$, in order to avoid appearance of interstitial vortices) and for channel and interstitial vortices (Fig. 5.8(b)).

To reveal the effect of the channel geometry on the vortex dynamics, we calculate IV-curves for varying channel gap, w (see Fig. 5.2). In case of channel vortices, they are all confined to the channel, and small gap results in vortex *pinning* by the diamond cells. The limiting case $w = 0$ corresponds, obviously, to the maximum vortex pinning. As a result, this situation is characterized by the maximum critical current and extended region of flux-pinning regime (Fig. 5.8(a)). The critical value corresponds to the "depinning" current, when a vortex overcomes the potential barrier and jumps from one diamond-cell to the adjacent cell through the "point contact".

Opening the gap allows an easier vortex transfer between the cells which in turn results in a lower critical current (see the IV-curve in Fig. 5.8(a) for $w = 4\xi$ and $w = 8\xi$). It is worth noting, however, that even for $w > \xi$ vortices remain pinned by the diamond cells, due to magnetic core pinning [106]. Indeed, the

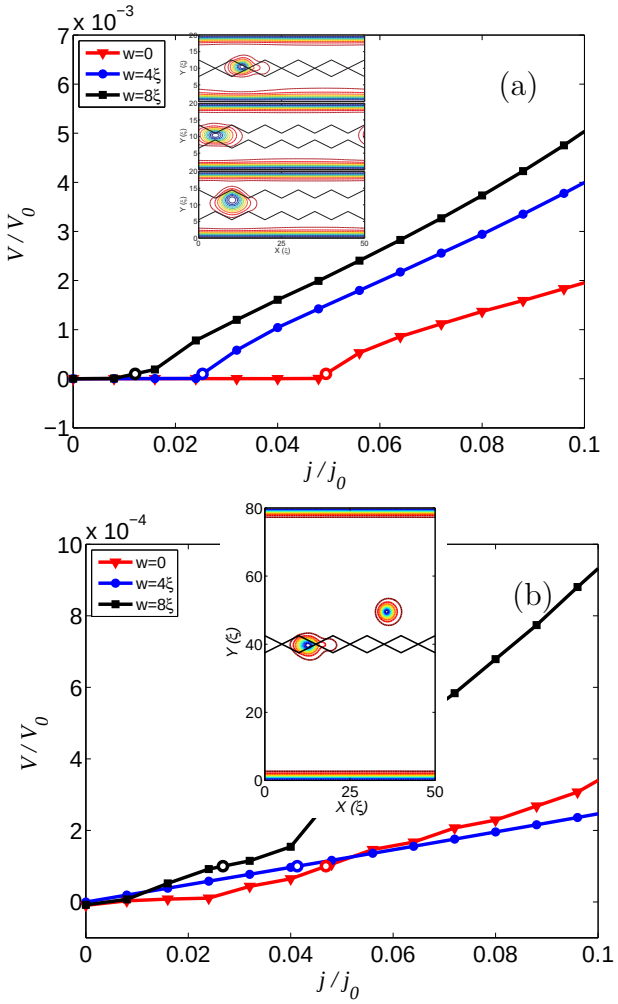

Figure 5.8: (Color online) The IV-curves of the system ($\xi_2/\xi_1 = 6$, $tg(\alpha) = 0.5$) for different sizes of the simulation cell (in an infinite sample): (a) $50\xi \times 20\xi$ with one vortex in the channel, which corresponds to external magnetic field $H = 0.035H_{c2}$ (for $w = 0$), $H = 0.025H_{c2}$ (for $w = 4\xi$), $H = 0.025H_{c2}$ (for $w = 8\xi$). The critical current is: $j_c = 0.012j_0$, $j_c = 0.025j_0$, and $j_c = 0.049j_0$, correspondingly. The insets show the distribution of the square modulus of the order parameter in the sample for the above channel configurations, $w = 0$, 4, and 8ξ. (b) $w = 50\xi \times 80\xi$ with one vortex in the channel and one interstitial vortex. The inset shows the order parameter in the cell with channel gap $w = 0$ at driving current $j = 0.048j_0$, and magnetic field $H = 0.004H_{c2}$. (A contour-plot for $w = 4\xi$ and $w = 4\xi$ is similar.) The critical current j_c (estimated using the voltage threshold criteria, $V_c = 10^{-4}V_0$) is $0.027j_0$, $0.041j_0$, and $0.047j_0$, correspondingly.

magnetic core of a vortex extends outside the channel, and the variation of the channel width determines the profile of the vortex supercurrent which is associated with a change in the energy of the vortex. This "soft-pinning" regime considerably enhances the tunability of a diamond channel "pinning array", in comparison to usual pinning array (i.e., consisting of separate pinning sites). As a result, by

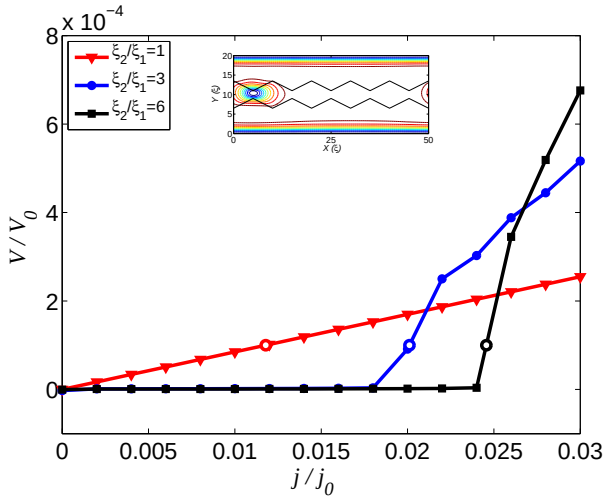

Figure 5.9: (Color online) The IV-curves of the system ($w = 4\xi$, $tg(\alpha) = 0.5$) for different ξ_2/ξ_1 ratio (in an infinite sample): The inset shows the order parameter distribution in the sample with channel for $w = 4\xi$, $\xi_2/\xi_1 = 6$, at $j = 0.032j_0$, and magnetic field $H = 0.025H_{c2}$.

changing the gap, w, we can gradually change the critical current of this system and thus manipulate the transition from flux-pinned to flux-flow regime. As shown above, for high enough fields vortices can enter the banks (i.e., the area outside the diamond channel), therefore, it is interesting to analyze the effect of interstitial vortices on the vortex dynamics in our system.

As expected, the presence of additional vortices will strongly suppress the flux-pinning regime, since interstitial vortices can flow freely for any low applied current. A non-zero critical current may appear only as a result of caging of interstitial vortices due to their interaction with pinned vortices, however, this value is much less than that for the channel vortices.

Indeed, Fig. 5.8(b) shows a smooth change of the IV-curve, with practically no flux-pinned to flux-flow threshold.

Although still we can distinguish the "critical currents" for various w, by defining a threshold voltage, e.g., $V_c = 10^{-4}V_0$. Thus in Fig. 5.8(b) the defined critical currents are $j_c = 0.027j_0$ for $w = 0$, $j_c = 0.041j_0$ for $w = 4\xi$, and $j_c = 0.047j_0$ for $w = 8\xi$. Therefore, the effect of "smooth pinning" in this case still remains, although it is much less pronounced than in the above case when all the vortices are defined by the channel. However, even in presence of interstitial vortices, changing the geometry of diamond channels allows us to control the vortex flow (see Fig. 5.8(b)).

The dynamics of the system strongly depends also on the material parameters, i.e., it is determined by the ratio of the coherence lengths in the channel and the bank, ξ_2/ξ_1. This dependence is illustrated by the IV-curves shown in Fig. 5.9 (here, we consider the situation when vortices are present only in the channel; adding interstitial vortices would smooth the IV-curves similarly to the case shown in Fig. 5.8(b)). The IV-curves are presented in Fig. 5.9 for $\xi_2/\xi_1 = 3$ and $\xi_2/\xi_1 = 6$.

As a reference, we also show the IV-curve for $\xi_2/\xi_1 = 1$, i.e., for a sample without channel. Clearly that in this case vortices are not pinned and they can freely move when driven by any value of the transport current. Therefore, the curve for $\xi_2/\xi_1 = 1$ does not contain a part corresponding to flux-pinned regime.

For ξ_2/ξ_1 values other than one, the motion of vortices occurs in the channel. Interestingly, this motion is influenced by two factors. On the one hand, due to the difference in the material parameters, vortex mobility in the channel is higher than outside the channel which favors larger velocity and thus voltage as compared to the case without channel. This trend can be seen in the flux-flow regime, i.e., for $j/j_0 > 0.025$ (see Fig. 5.9). However, on the other hand, the geometric constriction (i.e., the neck of the diamond channel) creates a pinning potential that traps a vortex resulting in non-zero critical current. Strikingly, a channel characterized by a larger value of ξ_2/ξ_1 (i.e., $\xi_2/\xi_1 = 6$) demonstrates a larger critical current than a channel with a lower ξ_2/ξ_1, in spite of the fact that vortex mobility in this channel is larger (which can bee seen in the flux-flow regime for $j/j_0 > 0.027$). This is explained by a stronger pinning effect for higher "contrast" between the material parameters in the channel and in the bank (i.e., the ratio ξ_2/ξ_1). Therefore, this indicates that the geometric constriction appears to be more important for controlling the transition from flux-pinned to flux-flow regime than the material parameters while the latter factor determines the motion for higher values of the current above the critical value.

5.4.2 Effect of commensurability

We demonstrated that the material parameters (i.e., the ratio ξ_2/ξ_1) and the geometry of the channel (i.e., the minimum channel width, w) have a profound effect on the flux dynamics in a superconductor with a diamond-like channel. In particular, we showed that by changing the ratio ξ_2/ξ_1 and the gap w, one can control the transition from flux-pinned to flux-flow regimes and the slope of the IV-curves (see Figs. 5.8 and 5.9). Further, we analyze the critical current in the system as a function of the external applied magnetic field, of $j_c(H)$. The results of simulations of $j_c(H)$ for three values of the channel width, $w = 0$, 4ξ, and 8ξ are shown in Fig. 5.10. Fig. 5.10(a) represents the case when vortices are confined in the diamond channel only. The $j_c(H)$-curves have a very peculiar view, namely, they consist of a set of plateaus. Each plateau corresponds to a fixed number of vortices in the channel, N_v^{ch}. For example, for $w = 0$, the critical current, j_c/j_0 has a constant large value ($j_c/j_0 \approx 0.28$) for a range of fields $H/H_{c2} \approx 0$ to 0.028. For this range of fields, no vortex is generated in the system, and the high value of the j_c corresponds to the depairing current (recall that the critical current is defined as a current resulting in a jump of voltage above some threshold value, e.g., $V_c/V_0 = 10^{-4}$).

For larger fields, $0.028 \lesssim H/H_{c2} \lesssim 0.04$, the value of the critical current drops almost order of magnitude. The analysis of the dynamical patterns shows that for this range of fields the system encounters one vortex per simulation cell, and the critical current corresponds to the depinning transition. Further increasing applied magnetic field up to $H/H_{c2} \approx 0.06$ results in a sequence of plateaus of decreasing

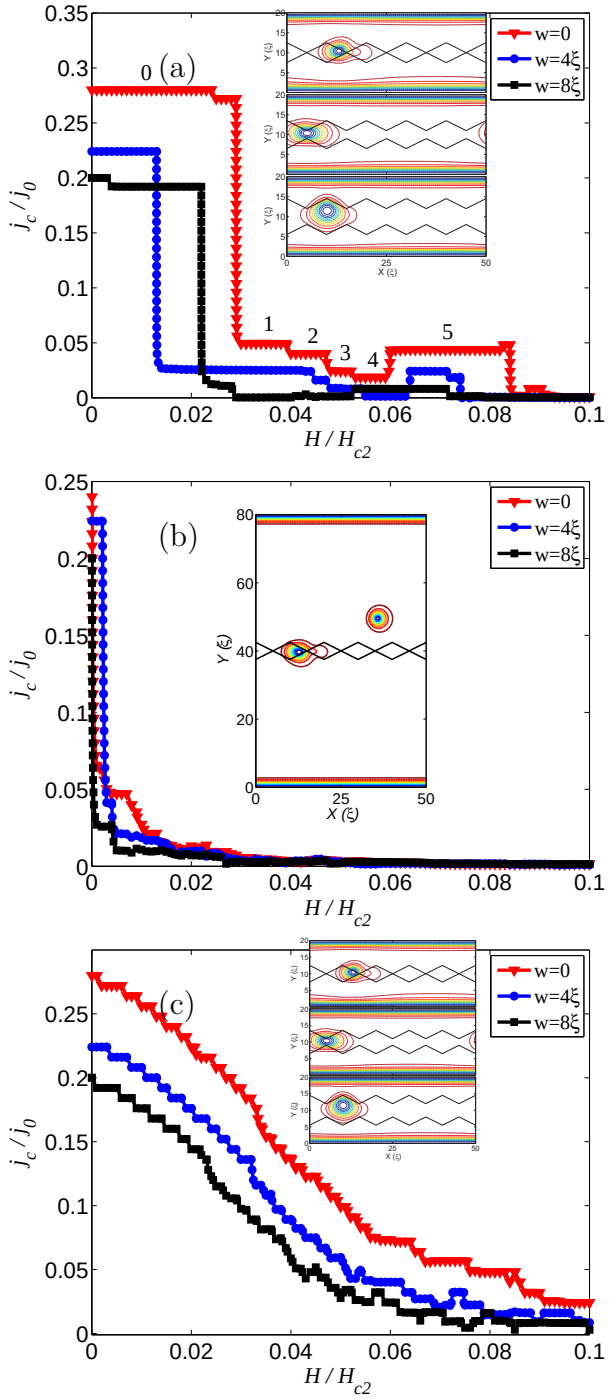

Figure 5.10: (Color online) The critical current as a function of the magnetic field, $j_c(H)$, for samples with $\xi_2/\xi_1 = 6$ and $tg(\alpha) = 0.5$, for varying channel gap. The system dimensions are: (a) $50\xi \times 20\xi$ (an infinite sample). Numbers near the plateaus in j_c show the correpsonding number of vortices in the diamond channel; (b) $50\xi \times 80\xi$ (an infinite sample). Interstitial vortices lead to a strong suppression of the critical current and disappearence of the plateaus; (c) $50\xi \times 20\xi$ (a finite-size sample). The function $j_c(H)$ shows a typical behavior for finite samples, i.e., decreasing with field.

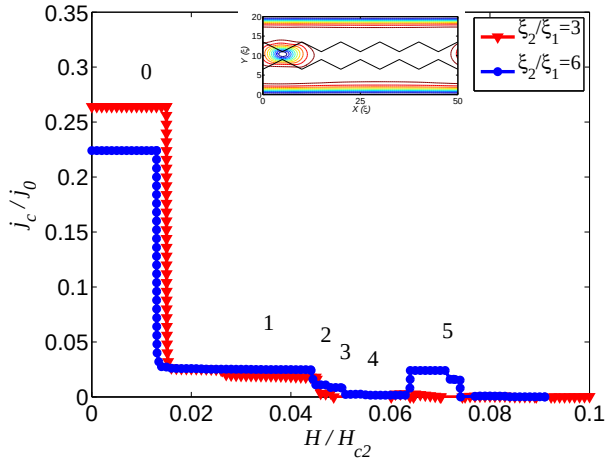

Figure 5.11: (Color online) The critical current $j_c(H)$ of the system with the cell dimensions $50\xi \times 20\xi$ (an infinite sample, $w = 4\xi$, $tg(\alpha) = 0.5$) for different ratios of the coherence lengths, ξ_2/ξ_1. Numbers near j_c-plateaus show the number of vortices in the diamond channel.

values in the function $j_c(H)$ corresponding to $N_v^{ch} = 1$, 2, 3, and 4. However, this tendency is violated for $N_v^{ch} = 5$, i.e., when the vortex number matches to the cell number in the diamond channel. The critical current increases, which is a direct consequence of a *commensurability effect*. When the number of vortices in the channel becomes larger than the cell number, the critical current rapidly decreases. A similar behavior is observed for wider channels, e.g., $w = 4\xi$ and 8ξ (see Fig. 5.10(a)), however, the overall value of the critical current is considerably lower, and the commensurability peak is much less pronounced. Interstitial vortices easily destroy the observed structure of the $j_c(H)$-curves: the critical current becomes much lower, and no commensurability features are revealed (see Fig. 5.10(b)). Note that the revealed commensurability peak (plateau) is also sensitive to the material parameters of the system. Thus, the commensurability peak found for $\xi_2/\xi_1 = 6$ disappears for a smaller value of the ratio, $\xi_2/\xi_1 = 3$ (see Fig. 5.11).

The demonstrated commensurability effect in diamond channels was also observed in the experiment [107]. Similarly, the critical current showed peaks for commensurate numbers of vortices in channels and channel cells. Note that in the experiments the $j_c(H)$-curves were smooth which can be attributed to: (i) large channels containing tens of diamond cells, and (ii) presence of multiple channels in the sample (which leads to inhomogeneous broadening, due to a dispersion of the number of vortices in different channels). The effect of smoothing of the $j_c(H)$-curves is also observed in finite samples (note that the $j_c(H)$-curves shown in Figs. 5.10(a) and (b)) were calculated for infinite channels, i.e., employing periodic boundary conditions). However, in this case the shape of $j_c(H)$-curves is dominated by the barriers at the boundaries of the channel leading to the typical decreasing $j_c(H)$ behavior [106].

The critical current can be controlled not only by the width of the channel, i.e., the gap, w, and the ratio of the coherence lengths inside and outside the channel,

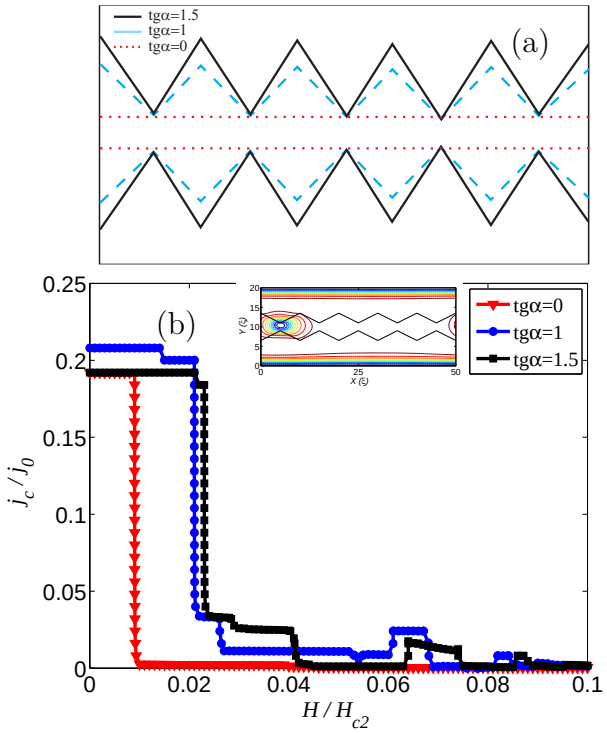

Figure 5.12: (Color online) Schematic view of the channel with different α. The critical current $j_c(H)$ of the system with the cell dimensions $50\xi \times 20\xi$ (an infinite sample, $w = 4\xi$, $\xi_2/\xi_1 = 6$) for channel shapes characterized by different$tg(\alpha)$.

ξ_2/ξ_1, but also by the shape of the diamond cells. To analyze the dependence of the critical current j_c on the shape of the channel compartments, we calculated the critical current for channels with tgα = 0, 1, and 1.5 (angle α is defined in Fig. 5.2), as shown in Fig. 5.12(a)). The corresponding function $j_c(H)$ is shown in Fig. 5.12(b). On can expect that increasing α should lead to a higher mobility of vortices in the channel, since larger α means increase in the effective width of the channel. On the other hand, increasing α means increasing steepness of the diamond cells, which prevent the motion of the vortices inside the channel. As a result, the dependence of j_c on tgα can be non-monotonous which is observed for magnetic fields in the range $0.03 < H/H_{c2} < 0.04$ and for the commensurability peak values, $H/H_{c2} \approx 0.065$ (see Fig. 5.12(b)).

Thus we demonstrated that the critical current j_c in a diamond channel can be controlled by the material parameter of the channel as well as by its geometry including the width of the channel and the shape of the diamond compartments.

5.5 Conclusions

By means of the time-dependent Ginzburg-Landau equations, we investigated the dynamics of vortices driven in a "diamond channel", i.e., a channel formed by superconducting material characterized by the critical temperature T_2 and the coherence length ξ_2 in shape of diamond-like cells inserted in another superconductor (bank) characterized by T_1 and ξ_1. We analyzed the conditions when generated

vortices occupy only the channel and then they can also be generated in the banks. Depending on this, the dynamics of driven vortices is very different: The presence of interstitial vortices results in the disappearance of flux-pinned regime and smoothing the IV-characteristics of the device. The most interesting is thus the situation when vortices are present only in the channel. In this case, the diamond channel acts as a "soft pinning" device. Unlike in a linear array of individual pinning centers, the pinning potentials created by diamond-shaped compartments overlap and create a periodically-modulated pinning channel. Thus this device is able to guide the flux and at the same time control the dynamical properties such as the transition from flux-pinned to flux-flow regime. The latter, as we show, can be reached by changing either the material parameters of the device (i.e., the ratio of the coherence lengths inside and outside the channel, ξ_2/ξ_1) or by the geometry of the channel (i.e., the degree of overlapping of the compartments defining the minimum channel width, w, and the specific shape of the diamond cells). We found that the critical current j_c of this device manifests striking commensurability features which were also observed in recent experiments [107].

Therefore, we demonstrated that a "diamond channel" can be a promising candidate for potential use in devices controlling magnetic flux motion.

Summary

Nano-patterned superconductors including hybrid systems consisting of a superconductor and an array of magnetic nano-particles of various shapes and arrangements, provide appealing opportunities for controlling the magnetic flux and thus the critical (depinning) current which is one of the goals of applied superconductivity. In this thesis, we report our results related to the study of the dynamics of magnetic flux in the following hybrid superconducting systems: (i) a superconductor with an array of magnetic bars with changing orientation on top, (ii) a superconductor with an array of zigzag arranged magnetic bars with switchable magnetization, and (iii) a superconductor with a diamond-shaped channel. We demonstrate that these hybrid systems, whose properties have been also investigated in experiments, are efficient devices for controlling magnetic flux (e.g., switching between flux-pinned and flux-flow regimes and the slopes of the voltage-current characteristics) and are promising candidates for applications.

Firstly, using the time-dependent Ginzburg-Landau equations, we studied the vortex-antivortex dynamics in a hybrid system consisting of a thin-film finite-size superconducting sample with a magnetic bar (or arrays of bars) on top. We showed that vortex-antivortex pairs are generated at the edges of the magnetic bar. These vortex-antivortex pairs are driven by the Lorentz force produced by an external current. The vortex-antivortex dynamics is studied as a function of the angle α between the direction of the dipole(s) and that of the Lorentz force. We found that the direction of motion of (anti)vortices coincides with the direction of the Lorentz force only for $\alpha = 0$ while in the general case of $\alpha \neq 0$ the direction of the (anti)vortex velocity vector does not coincide with the direction of the Lorentz force. Thus we revealed the effect of *guidance* of the (anti)vortex motion induced by the magnetic bars. In case of a single magnetic bar, the (anti)vortex motion is strongly influenced by boundary effects, i.e., by the interaction of the (anti)vortices with their images. On the other hand, in an array of magnetic bars the (anti)vortex motion is governed by the balance of the interaction forces with the array environment.

Depending on the relation between the driving force and the interaction forces, we found different dynamical regimes of (anti)vortex motion. The most interesting regime is observed when the parameters of the system are chosen in such a way that the driving force and the typical interaction forces of (anti)vortices with magnetic dipoles are of the same order (which can be provided by a proper choice of the size and the magnetic moment of the bars). In this case, switching between different dynamical regimes, which include either guided motion of (anti)vortices or vortex-antivortex annihilation (resulting in zero voltage), can be achieved by

slightly changing the applied current. In order to study the effect of the external current, we calculated the phase diagram "critical angle – current", for different sizes of the magnetic bars. We found that the value of the critical angle increases with increasing the length of the bars, for the same applied current. To better understand the nature of the revealed different dynamical regimes, we analyzed in detail the IV-curves for different angles α.

Our approach allows us to self-consistently account for the nucleation of vortex-antivortex pairs and study their dynamics. The obtained results provide a tool for an effective manipulation of magnetic flux in nano-patterned hybrid structures and therefore could be potentially useful for applications in fluxonics devices.

Secondly, we have investigated the vortex-antivortex dynamics in a hybrid system consisting of a superconducting film with an array of magnetic bars on top using the time-dependent Ginzburg-Landau equations. This system was recently realized experimentally in Refs. [84, 59]. In the plane of the film, the magnetic bars form parallel rows of bars oriented perpendicular with respect to the bars in the adjacent row, i.e., they are arranged in a "zigzag" configuration.

The striking property of this zigzag array is that, by changing the magnetization of the magnetic bars by applying an in-plane magnetic field, the configuration of the magnetic field can be switched from "parallel" to "anti-parallel", i.e., when the apices of the neighboring bars in the rows are magnetized either in the same or in the opposite direction. This switching of the magnetic-field configuration has a dramatic impact on the dynamics of the vortex-antivortex motion in the system and the mechanism of flux transfer. We consequently simulated the system with out-of-plane dipoles (i.e., for narrow bars) and in-plane dipoles (for wider bars). The results are consistent with each other and lead to the same conclusions. The parallel configuration is characterized by a dense and shallow potential profile which favors the flux-flow regime having low critical currents. Contrary to that, the anti-parallel configuration is characterized by a relatively deep and less dense potential profile resulting in a flux-pinned regime with a high critical current. While this main result is easily understandable, and our results agree with recent experimental observations in Refs. [84, 59], the mechanisms behind the flux transfer and the detailed vortex-antivortex dynamics is rather complicated in this system. As we demonstrated, it involves the process of vortex-antivortex generation under the tips of the bars (or in the vicinity to the bars) and their annihilation, which is strongly affected by the system parameters such as the magnetization of the bars, the spacing between the bars in the plane of the superconductor and the spacing between the bars and the superconductor. Using the results of our calculations and the understanding of the different underlying mechanisms of flux transfer, one can improve the performance of this artificial device, i.e., to increase the ratio of the critical currents for the two distinct in-plane magnetizations: parallel and antiparallel, $j_c^{\mathrm{AP}}/j_c^{\mathrm{P}}$, by using the zigzag-arranged magnetic bars which can be useful for magnetic flux manipulation in fluxonics applications.

Thirdly, by means of the time-dependent Ginzburg-Landau equations, we investigated the dynamics of vortices driven through a "diamond channel", i.e., a channel formed by superconducting material characterized by the critical temperature T_2 and the coherence length ξ_2 in the shape of diamond-like cells inserted in

another superconductor (bank) characterized by T_1 and ξ_1. We analyzed the conditions when generated vortices occupy only the channel and when they can also be generated in the banks. Depending on this, the dynamics of driven vortices is very different: The presence of interstitial vortices results in the disappearance of the flux-pinned regime and the smoothing of the IV-characteristics of the device.

The most interesting is the situation when vortices are present only in the channel. In this case, the diamond channel acts as a "soft pinning" device. Unlike in a linear array of individual pinning centers, the pinning potentials created by diamond-shaped compartments overlap and create a periodically-modulated pinning channel. Thus this device is able to guide the flux and at the same time control the dynamical properties such as the transition from flux-pinned to flux-flow regime. The latter, as we show, can be reached by changing either the material parameters of the device (i.e., the ratio of the coherence lengths inside and outside the channel, ξ_2/ξ_1) or by the geometry of the channel (i.e., the degree of overlapping of the compartments defining the minimum channel width, w, and the specific shape of the diamond cells). We found that the critical current j_c of this device manifests striking commensurability features which were also observed in recent experiments [107].

Therefore, we demonstrated that a "diamond channel" can be a promising candidate for potential use in devices controlling magnetic flux motion.

Samenvatting

Nano-patroon supergeleiders waaronder hybride systemen bestaande uit een supergeleider en een serie van magnetische nanodeeltjes van verschillende vormen en rangschikkingen bieden aantrekkelijke mogelijkheden voor het controleren van de magnetische flux en dus de kritische (depinning) stroom wat een van de doelstellingen is van toegepastingen van supergeleiding. In dit proefschrift rapporteren we onze resultaten met betrekking tot de studie van de dynamiek van de magnetische flux in de volgende hybride supergeleidende systemen: (i) een supergeleider met er baren op een scala van magnetische staven met veranderende oriëntatie, (ii) een supergeleider met een serie van zigzag gerangschikt magneten met schakelbare magnetisatie, en (iii) een supergeleider met een ruit kanaal. We tonen aan dat deze hybride systemen, waarvan de eigenschappen ook zijn onderzocht in experimenten, efficiënte apparaten zijn voor het regelen van de magnetische flux (bijvoorbeeld schakelen tussen gepinde flux en flux-vloei regimes en de hellingen van de spanning-stroom karakteristieken) en veelbelovende kandidaten voor toepassingen.

Ten eerste, gebruik makend van de tijdsafhankelijke Ginzburg-Landau vergelijkingen onderzochten we de vortex-antivortex dynamica in een hybride systeem bestaande uit een dunne-film met supergeleider eindige grootte met er baren op een magnetisch staafje (of reeksen staven). We toonden aan dat vortex-antivortex paren ontstaan aan de randen van de magneetstaaf. Deze vortex-antivortex paren worden gedreven door de Lorentz-kracht die geproduceerd wordt door een externe stroom. De vortex-antivortex dynamica wordt bestudeerd als functie van de hoek α tussen de richting van de magnetische dipool(s) en de Lorentz-kracht. We vonden dat wanneer de bewegingsrichting van (anti)vortices samenvalt met de richting van de Lorentz-kracht slechts $\alpha = 0$ geldt terwijl in het algemene geval van $\alpha \neq 0$ de richting van de (anti)vortex snelheids-vector niet samenvalt met de richting van de Lorentz-kracht. Aldus bleek het effect van *het richten* van de (anti)vortex beweging zoals geïnduceerd door de magnetische staven. In geval van één enkele magnetische stoof, wordt de (anti)vortex beweging sterk beïnvloed door grens-effecten, dat wil zeggen, door de interactie van de (anti)vortices met hun beelden. Anderzijds, in de aanwezigheid vaneen reeks magnetische staven wordt de (anti)vortex beweging geregeld door het evenwicht van de interactiekrachten met deze stoven.

Afhankelijk van de verhouding tussen de kracht t.g.v. de stroom en de interactiekrachten, vonden we verschillende regimes van (anti)vortex beweging. Het interessantste regime wordt waargenomen wanneer de parameters van het systeem zodanig zijn gekozen dat de stroomkracht en de typische interactiekrachten van (anti)vortices met magnetische dipolen van dezelfde orde zijn (dit kan worden gerealiseerd door een geschikte keuze van de grootte en van magnetische moment

van de staven). In dit geval schakelen tussen de verschillende regimes, zijnde van geleide beweging van (anti)vortices of vortex-antivortex vernietiging (resulterend in geen spanning), kan worden bereikt door het varieren van de aangelegde stroom. Om het effect van de externe stroom te onderzoeken berekenden we het fasediagram "kritische hoek – stroom", voor verschillende afmetingen van de magnetische staven. We vonden dat de waarde van de kritische hoek toeneemt met de lengte van de staven, voor dezelfde aangelegde stroom. Om de aard van de verschillende regimes beter te begrijpen, analyseerde we de IV-curves voor verschillende hoeken α.

Onze aanpak maakt het mogelijk om zelf-consistent rekening te houden met de nucleatie van vortex-antivortex paren en hun dynamiek. De verkregen resultaten zijn belangrijk voor een effectieve manipulatie van magnetische flux in nano-gevormde hybride structuren en kunnen dus nuttig zijn voor toepassingen apparaten gebaseerd op fluxonica.

Ten tweede hebben we de vortex-antivortex dynamiek onderzocht in een hybride systeem bestaande uit een supergeleidende film met er baren op een reeks magnetische balken. Hierbij gebruikte we de tijdsafhankelijke Ginzburg-Landau vergelijkingen. Dit systeem werd onlangs experimenteel gerealiseerd in Refs. [84, 59]. In het vlak van de film, vormen de magnetische staven evenwijdige rijen die loodrecht gerangschikt zijn ten opzichte van de staven in de naburige rij. Met andere woorden, ze zijn gerangschikt in een "zigzag" configuratie.

De opvallende eigenschap van deze zigzag configuratie is dat door het veranderen van de magnetisatie van de staven door middel van een magnetisch veld in het vlak, de configuratie van het magnetisch veld kan worden omgeschakeld van "parallel" naar "anti-parallel" , dat wil zeggen, wanneer de toppen van de naburige staven in de rijen zijn gemagnetiseerd hetzij in dezelfde of in tegengestelde richting. Deze verondering van de magnetische-veld configuratie heeft een dramatisch effect op de dynamiek van de vortex-antivortex beweging in het systeem en het mechanisme van de fluxoverdracht. We simuleerde het systeem met dipolen die gezicht zjn uit het vlak (dwz, voor smalle balken) en in het vlak (voor bredere balken). De resultaten zijn in overeenstemming met elkaar en leiden tot dezelfde conclusies. De parallelle configuratie wordt gekenmerkt door een dicht en ondiep potentieele profiel dat gunstig is van het flux-stroom regime met lage kritische stroom. In tegenstelling de anti-parallelle configuratie met een relatief diepe en minder dichte potentiaalprofiel resulteert in het flux pinning regime met een hoge kritische stroom. Hoewel dit belangrijke resultaat gemakkelijk te begrijpen is, en onze resultaten overeen komen met de recente experimentele waarnemingen van Refs. [84, 59], is het mechanise achter de fluxtransfer en de gedetailleerde vortex-antivortex dynamiek nogal ingewikkeld. Zoals we hebben aangetoond, wordt het proces van vortex-antivortex-generatie dat plaats heeft onder de uiteinden van de staven (of in de nabijheid van de staven) en hun vernietiging, sterk beïnvloed door de systeem parameters zoals de magnetisatie van de balken, de afstand tussen de staven in het vlak van de supergeleider en de afstand tussen de staven en de supergeleider. Door gebruik te maken van onze berekeningen en danksij het begrijpen van de verschillende onderliggende mechanismen van fluxtransfer, kan men de prestatie van het apparaat verhogen, m.a.w. een vergroting van de verhoud-

ing van de kritische stroom voor de twee verschillende magnetisaties: parallel en antiparallel, $j_c^{\mathrm{AP}}/j_c^{\mathrm{P}}$.

Ten derde door gebruik te maken van de tijdsafhankelijke Ginzburg-Landau vergelijkingen, onderzochten we de dynamica van vortices gedreven doorheen een "diamant kanaal", dat wil zeggen een kanaal gevormd door supergeleidend materiaal gekenmerkt door de kritische temperatuur T_2 en de coherentielengte ξ_2 in de vorm van diamantachtige cellen die ingevoegd zijn in een supergeleider met T_1 en ξ_1. We analyseerden de voorwaarden wanneer de vortices warden gegenereerd in het kanaal of erbuiten. Afhankelijk hiervan, verschilt de dynamica van de aangedreven vortices: De aanwezigheid van interstitiële vortices resulteert in het verdwijnen van het flux-pinnings regime en wodt de IV-curve glad.

Het meest interessante is dus de situatie wanneer de vortices alleen aanwezig zijn in het kanaal. In dit geval, fungeert het diamant kanaal als een "zachte pinning" apparaat. Anders dan in een lineaire reeks van individuele pinning centra, overlappen de pinning potentialen die gecreëerd worden door de ruitvormige vakken en resulteren ze in een periodiek gemoduleerde pinnings kanaal. Hierdoor kan de flux gestuurd worden en tegelijk kunnen de dynamische eigenschappen zoals de overgang van flux-pinning narr flux-vloei regime worden gecontroleerd. dit kan gerealiseerd worden door ofwel de materiaalparameters (dat wil zeggen de verhouding van de coherentie lengte binnen en buiten het kanaal, ξ_2/ξ_1) of de geometrie van het kanaal (de mate van overlapping van de compartimenten waarin de kanaalbreedte minimum, w, en de specifieke vorm van de diamant cellen) te veranderen. We vonden dat de kritische stroom j_c van dit apparaat zich manifesteert in opvallende commensurabiliteits structuren die ook werden waargenomen in recente experimenten [107].

Aldus hebben we aangetoond dat een "diamant kanaal" veelbelovend is voor gebruik in apparaten waarbij men de magnetische flux beweging wil controleren.

Bibliography

[1] H. Kamerlingh Onnes, Leiden Comm. **122b**, 124 (1911).

[2] W. Meissner and R. Ochsenfeld, Naturwiss. **21**, 787 (1933).

[3] F. London and H. London, Proc. Roy. Soc. **A149**, 71 (1935).

[4] F. London, *Superfluids* (John Wiley & Sons, Inc., New York, 1950).

[5] R. Doll and M. Näbauer, Phys. Rev. Lett. **7**, 51 (1961).

[6] V. L. Ginzburg and L. D. Landau, Zh. Eksp. Teor. Fiz. **20**, 1064 (1950).

[7] J. Bardeen, L. N. Cooper, and J. R. Schrieffer, Phys. Rev. **108**, 1175 (1957).

[8] L.P. Gor'kov, ZhETF **36(6)**, 1918-1923 (1959). [L.P. Gor'kov, Sov. Phys. JETP **9**, 1364-1367 (1959)].

[9] A. A. Abrikosov, Sov. Phys. JETP **5**, 1174 (1957).

[10] B. D. Josephson, Phys. Lett. **1**, 251 (1962).

[11] J. G. Bednorz and K. A. Muller, Z. Phys. B **64**, 189 (1986).

[12] US Department of Energy report, *Basic Research Needs for Superconductivity.* (2006).

[13] M. Wang et al., arXiv:1303.7339 (2013)

[14] Y. Kamihara, T. Watanabe, M. Hirano, and H. Hosono, J. Am. Chem. Soc. **130**, 3296 (2008).

[15] V. V. Schmidt, *The Physics of Superconductors* (Springer, 1997).

[16] M. Tinkham, *Introduction to Superconductivity* (New York: McGraw-Hill, 1996).

[17] M. V. Milošević, *PhD Thesis* (Antwerpen, 2004).

[18] M. R. Connolly, M. V. Milošević, S. J. Bending, and T. Tamegai, Phys. Rev. B **78**, 132501 (2008).

[19] C. Jooss, J. Albrecht, H. Kuhn, S. Leonhardt, and H. Kronmuller, Rep. Prog. Phys. **65**, 651 (2002).

[20] T. Tamegai, M. Matsui, M. Yasugaki, Y. Tokunaga, and M. Tokunaga, NATO Science Series B: Physics, Vol. 142, p. 95. (2004).

[21] P. J. Curran, J. R. Clem, S. J. Bending, Y. Tsuchiya, and T. Tamegai, Phys. Rev. B **82**, 134501 (2010).

[22] J. R. Hull, Supercond. Sci. Technol. **13**, R1 (2000).

[23] F. N. Werfel, U. Floegel-Delor, R. Rothfeld, T. Riedel, B. Goebel, D. Wippich and P. Schirrmeister, Supercond. Sci. Technol. **25**, 014007 (2012).

[24] J. Wang et al., Physica C **378–381**, 809 (2002).

[25] www.gizchina.com/2010/08/05/china-plans-1000-kmh-maglev-trains/

[26] Q. P. Herr, A. Y. Herr, O. T. Oberg, and A. G. Ioannidis, J. Appl. Phys. **109**, 103903 (2011).

[27] W. D. Gropp, H. G. Kaper, G. K. Leaf, D. M. Levine, M. Palumbo, and V. M. Vinokur, Comput. Phys. **123**, 254266 (1996).

[28] J. D. Jackson, Classical Electrodynamics (Wiley, New York, 1975).

[29] Q. Du, Applicable analysis **53**, p.1-17 (1993).

[30] R. Kato, Y. Enomoto, and S. Maekawa, Phys. Rev. B **44**, 6916 (1991).

R. Kato, Y. Enomoto, and S. Maekawa, Phys. Rev. B **47**, 8016 (1992).

[31] R. Prozorov, E. B. Sonin, E. Sheriff, A. Shaulov, and Y. Yeshurun, Phys. Rev. B **57**, 13845 (1998).

[32] *Numerical Recipes*, (Cambridge Press, 2007).

[33] A. V. Kapra, V. R. Misko, D. Y. Vodolazov, and F. M. Peeters, Supercond. Sci. Technol. **24**, 024014 (2011).

[34] P. G. de Gennes, *Superconducting of Metals and Alloys* (New York, Benjamin, 1966)

[35] M. Baert, V. V. Metlushko, R. Jonckheere, V. V. Moshchalkov, and Y. Bruynseraede, Phys. Rev. Lett. **74**, 3269 (1995).

[36] V. V. Moshchalkov, M. Baert, V. V. Metlushko, E. Rosseel, M. J. Van Bael, K. Temst, R. Jonckheere, and Y. Bruynseraede, Phys. Rev. B **54**, 7385 (1996).

[37] A. Bezryadin and B. Pannetier, J. Low Temp. Phys. **102**, 73 (1996).

A. Bezryadin, Y. N. Ovchinnikov, and B. Pannetier, Phys. Rev. B **53**, 8553 (1996).

[38] A. M. Castellanos, R. Wördenweber, G. Ockenfuss, A. v. d. Hart, and K. Keck, Appl. Phys. Lett. **71**, 962 (1997).

[39] R. Wördenweber, P. Dymashevski, and V. R. Misko, Phys. Rev. B **69**, 184504 (2004).

[40] J. Eisenmenger, Z-P. Li, W. A. A. Macedo, and I. K. Schuller, Phys. Rev. Lett. **94**, 057203 (2005).

[41] J. E. Villegas, S. Savel'ev, F. Nori, E. M. Gonzalez, J. V. Anguita, R. García, and J. L. Vicent, Science **302**, 1188 (2003).

[42] L. Van Look, B. Y. Zhu, R. Jonckheere, B. R. Zhao, Z. X. Zhao, and V. V. Moshchalkov, Phys. Rev. B **66**, 214511 (2002).

[43] A. V. Silhanek, S. Raedts, M. Lange, and V. V. Moshchalkov, Phys. Rev. B **67**, 064502 (2003).

[44] B. Pannetier, S. Rodts, J. L. Genicon, Y. Otani, and J. P. Nozières, Macroscopic Quantum Phenomena and Coherence in Superconducting Networks (Singapore: World Scientific) chapter (Nucleation of Superconductivity in a Thin Film in a Spatially Modulated Magnetic Field) pp 17-24 (1995).

[45] Y. Otani, B. Pannetier, J. P. Nozières, and D. Givord, J. Magn. Magn. Mater. **126**, 622-5 (1993).

[46] O. Geoffroy, D. Givord, Y. Otani, B. Pannetier, and F. Ossart, J. Magn. Magn. Mater. **121**, 223-6 (1993).

[47] J. I. Martin, M. Vélez, J. Nogués, and I. K. Schuller, Phys. Rev. Lett. **79**, 1929 (1997).

[48] M. J. Van Bael, K. Temst, V. V. Moshchalkov, and Y. Bruynseraede, Phys. Rev. B **59**, 14674 (1999).

[49] M. V. Milošević, S. V. Yampolskii, and F. M. Peeters, Phys. Rev. B **66**, 174519 (2002).

[50] M. M. Doria, Physica C **404**, 145-52 (2004).

[51] M. V. Milošević and F. M. Peeters, Phys. Rev. Lett. **93**, 267006 (2004).

[52] M. V. Milošević and F. M. Peeters, Physica C **404**, 246-50 (2004).

[53] M. V. Milošević and F. M. Peeters, Phys. Rev. Lett. **94**, 227001 (2005).

[54] M. V. Milošević and F. M. Peeters, Europhys. Lett. **70**, 670-6 (2005).

[55] G. R. Berdiyorov, M. V. Milošević, and F. M. Peeters, Phys. Rev. B **80**, 214509 (2009).

[56] I. F. Lyuksyutov and V. I. Pokrovsky, Phys. Rev. Lett. **81**, 2344 (1998).

[57] L. S. Lima and C. de Souza Silva, Phys. Rev. B **80**, 054514 (2009).

[58] V. N. Gladilin, J. Tempere, J. T. Devreese, W. Gillijns, and V. V. Moshchalkov, Phys. Rev. B **80**, 054503 (2009).

[59] A. V. Silhanek, J. Van de Vondel, A. Leo, G W. Ataklti, W. Gillijns, and V. V. Moshchalkov, Supercond. Sci. Technol. **22**, 034002 (2009).

[60] A. Weber and L. Kramer, J. Low Temp. Phys. **84**, 289 (1991).

[61] L. Kramer and R. J. Watts-Tobin, Phys. Rev. Lett. **40**, 1041 (1978).

[62] B. I. Ivlev and N. B. Kopnin, Usp. Fiz. Nauk **142**, 435-471 (1984).

B. I. Ivlev and N. B. Kopnin, Sov. Phys. Usp. **27**, 206 (1984).

[63] D. Y. Vodolazov, F. M. Peeters, I. V. Grigorieva, and A. K. Geim, Phys. Rev. B **72**, 024537 (2005).

[64] D. Y. Vodolazov, B. J. Baelus, and F. M. Peeters, Physica C **404**, 400 (2004).

[65] Note that in absence of external magnetic field these regimes, i.e., "field-cooled" and "zero-field-cooled" regimes, refer to the field created by the magnetic bar.

[66] A. A. Abrikosov, *Fundamentals of the Theory of Metals* (Amsterdam, Elsevier, 1986).

[67] A. V. Kapra, V. R. Misko, and F. M. Peeters, Supercond. Sci. Technol. **26**, 025011 (2013).

[68] V. V. Moshchalkov and J. Fritzsche, *Nanostructured Superconductors* (Singapore: World Scientific, 2011)

[69] R. K. Rakshit, R. C. Budhani, T. Bhuvana, V. N. Kulkarni, and G. U. Kulkarni, Phys. Rev. B **77**, 052509 (2008).

[70] V. V. Moshchalkov, M. Baert, V. V. Metlushko, E. Rosseel, M. J. Van Bael, K. Temst, Y. Bruynseraede, and R. Jonckheere, Phys. Rev. B **57**, 3615 (1998).

[71] L. Goren and E. Altman, Phys. Rev. B **84**, 094508 (2011).

[72] G. Carneiro, Phys. Rev. B **69**, 214504 (2004).

[73] Y. Jaccard, J I. Martín, M.-C. Cyrille, M. Vélez, J. L. Vicent, and I. K. Schuller, Phys. Rev. B **58**, 8232 (1998).

[74] M. J. Van Bael, J. Bekaert, K. Temst, L. Van Look, V. V. Moshchalkov, Y. Bruynseraede, G. D. Howells, A. N. Grigorenko, S. J. Bending, and G. Borghs, Phys. Rev. Lett. **86**, 155 (2001).

[75] J. E. Villegas, K. D. Smith, L. Huang, Y. Zhu, R. Morales, and I. K. Schuller, Phys. Rev. B **77**, 134510 (2008).

[76] Y. Togawa, K. Harada, T. Akashi, H. Kasai, T. Matsuda, F. Nori, A. Maeda, and A. Tonomura, Phys. Rev. Lett. **95**, 087002 (2005).

[77] J. F. Wambaugh, C. Reichhardt, C. J. Olson, F. Marchesoni, and F. Nori, Phys. Rev. Lett. **83**, 5106 (1999).

[78] J. Mannhart, Supercond. Sci. Technol. **9**, 49 (1996).

[79] I. Sochnikov, I. Božović, A. Shaulov, and Y. Yeshurun, Phys. Rev. B **84**, 094530 (2011).

[80] D. Perez de Lara, F. J. Castaño, B. G. Ng, H. S. Korner, R. K. Dumas, E. M. Gonzalez, K. Liu, C. A. Ross, I. K. Schuller, and J. L. Vicent, Phys. Rev. B **80** 224510 (2009).

[81] Q. H. Chen, C. Carballeira, and V. V. Moshchalkov, Phys. Rev. B **79**, 104520 (2009).

[82] M. Menghini, R. B. G. Kramer, A. V. Silhanek, J. Sautner, V. Metlushko, K. De Keyser, J. Fritzsche, N. Verellen, and V. V. Moshchalkov, Phys. Rev. B **79**, 144501 (2009).

[83] A. V. Silhanek, V. N. Gladilin, J. Van de Vondel, B. Raes, G. W. Ataklti, W. Gillijns, J. Tempere, J. T. Devreese, V. V. Moshchalkov, Supercond. Sci. Technol. **24**, 024007 (2011).

[84] J. Van de Vondel, A. V. Silhanek, B. Raes, W. Gillijns, R. B. G. Kramer, V. V. Moshchalkov, J. Sautner, and V. Metlushko, Appl. Phys. Lett. **95**, 032501 (2009).

[85] A. Yu. Aladyshkin, A. V. Silhanek, W. Gillijns and V. V. Moshchalkov, Supercond. Sci. Technol. **22**, 053001 (2009).

[86] J. Pearl, Appl. Phys. Lett. **5**, 4 (1964).

[87] J. Sosnowski, M. Rabara, K. Demachi, and K. Miya, Supercond. Sci. Technol. **13**, 558 (2000).

[88] A. V. Kapra, D. Y. Vodolazov, and V. R. Misko, *Submitted to* Supercond. Sci. Technol. (2013).

[89] C. P. Bean, Phys. Rev. Lett. **8**, 250 (1962).

[90] P. Selders and R. Wördenweber, Appl. Phys. Lett. **76**, 3277 (2000).

[91] V. Misko, S. Savel'ev, and F. Nori, Phys. Rev. Lett. **95**, 177007 (2005).

[92] V.R. Misko, S. Savel'ev, and F. Nori, Phys. Rev. B **74**, 024522 (2006).

[93] R. B. G. Kramer, A. V. Silhanek, J. Van de Vondel, B. Raes, and V. V. Moshchalkov, Phys. Rev. Lett. **103**, 067007 (2009).

[94] M. Kemmler, C. Gürlich, A. Sterck, H. Pöhler, M. Neuhaus, M. Siegel, R. Kleiner, and D. Koelle, Phys. Rev. Lett. **97**, 147003 (2006).

[95] V. R. Misko, D. Bothner, M. Kemmler, R. Kleiner, D. Koelle, F.M. Peeters, and F. Nori, Phys. Rev. B **82**, 184512 (2010).

[96] A. V. Silhanek, W. Gillijns, V.V. Moshchalkov, B.Y. Zhu, J. Moonens, and L.H.A. Leunissen, Appl. Phys. Lett. **89**, 152507 (2006).

[97] C. J. Olson Reichhardt and C. Reichhardt, Phys. Rev. B **81**, 224516 (2010).

[98] N. S. Lin, T. W. Heitmann, K. Yu, B. L. T. Plourde, and V. R. Misko, Phys. Rev. B **84**, 144511 (2011).

[99] J. Van de Vondel, C. C. de Souza Silva, B. Y. Zhu, M. Morelle, and V. V. Moshchalkov, Phys. Rev. Lett. **94**, 057003 (2005).

[100] A. O. Sboychakov, S. Savel'ev, A. L. Rakhmanov, and F. Nori, Phys. Rev. Lett. **104**, 190602 (2010).

[101] I. Derenyi, Appl. Phys. A **75**, 217 (2002).

[102] S. Savel'ev, V. Misko, F. Marchesoni, and F. Nori, Phys. Rev. B **71**, 214303 (2005).

[103] S. Savel'ev, V. Misko, F. Marchesoni, F. Nori, A. V. Silhanek, J. Van de Vondel, V. V. Moshchalkov, A. Leo, V. Metlushko, B. Ilic, V. R. Misko, and F. M. Peeters, Appl. Phys. Lett. **92**, 176101 (2008).

[104] J. Cuppens, G. W. Ataklti, V. V. Moshchalkov, A. V. Silhanek, J. Van de Vondel, C. C. de Souza Silva, R. M. da Silva, and J. Albino Aguiar, Phys. Rev. B **84**, 184507 (2011).

[105] N. Kokubo, T. G. Sorop, R. Besseling, and P. H. Kes, Phys. Rev. B **73**, 224514 (2006).

[106] B. L. T. Plourde, D.J. Van Harlingen, D. Y. Vodolazov, R. Besseling, M. B. S. Hesselberth and P. H. Kes, Phys. Rev. B **64**, 014503 (2001).

[107] K. Yu, M. B. S. Hesselberth, P. H. Kes, and B. L. T. Plourde, Phys. Rev. B **81**, 184503 (2010).

[108] C. Reichhardt and F. Nori, Phys. Rev. Lett. **82**, 414 (1999).

[109] A. V. Silhanek, L. Van Look, S. Raedts, R. Jonckheere, and V. V. Moshchalkov, Phys. Rev. B **68**, 214504 (2003).

[110] J.I. Vestgården, V.V. Yurchenko, R. Wördenweber, and T.H. Johansen, Phys. Rev. B **85**, 014516 (2012).

[111] V. A. Schweigert, F. M. Peeters, and P. S. Deo, Phys. Rev. Lett. **81**, 2783-2786 (1998).

[112] A. K. Geim, S. V. Dubonos, I. V. Grigorieva, K. S. Novoselov, F. M. Peeters, and V. A. Schweigert, Nature (London) **407**, 55 (2000).

[113] I. V. Grigorieva, W. Escoffier, J. Richardson, L. Y. Vinnikov, S. Dubonos, and V. Oboznov, Phys. Rev. Lett. **96**, 077005 (2006).

[114] I. V. Grigorieva, W. Escoffier, V. R. Misko, B. J. Baelus, F. M. Peeters, L. Y. Vinnikov, and S. V. Dubonos, Phys. Rev. Lett. **99**, 147003 (2007).

[115] L. F. Chibotaru, A. Ceulemans, V. Bruyndoncx, and V. V. Moshchalkov, Nature (London) **408**, 833 (2000).

[116] V. R. Misko, V. M. Fomin, J. T. Devreese, and V. V. Moshchalkov, Phys. Rev. Lett. **90**, 147003 (2003).

[117] D. A. Dikin, V. Chandrasekhar, V. R. Misko, V. M. Fomin, and J. T. Devreese, The European Physical Journal B **34** 231-235 (2003).

Curriculum Vitae

Andrey Kapra
Born on 22*nd* July 1986
in Tiraspol, Moldavia

Contact Information

Departement Fysica

Universiteit Antwerpen (CGB)

Groenenborgerlaan 171

B-2020 Antwerpen

Belgium

Andrey.Kapra@ua.ac.be

Skills

Programming: C++, Fortran 77/95 (MPI, OpenMP, accent on the Module Programming and less on OOP), MATLAB
OS: GNU Linux (Debian, Ubuntu), Windows (XP, Vista)
Text editing: Vim, LaTeX, MS Office (Office, Excell, Powerpoint)
Other: Corel Draw, Origin, LabView
Languages: Russian (native), English (fluent)

Education

2003-2008 — M.Sc. Physics, Pridnestrovsky State University (Department of Physics and Mathematics), Tiraspol, Moldova

2008-2013 — PhD Physics, University of Antwerpen (Department of Physics), Antwerpen, Belgium

List of publications

1 A. V. Kapra, V. R. Misko, D. Y. Vodolazov, and F. M. Peeters, *The guidance of vortex-antivortex pairs by in-plane magnetic dipoles in a superconducting finite-size film*, Supercond. Sci. Technol. **24**, 024014 (2011)

2 A. V. Kapra, V. R. Misko, and F. M. Peeters, *Controlling magnetic flux motion by arrays of zigzag-arranged magnetic bars*, Supercond. Sci. Technol. **26**, 025011 (2013)

3 A. V. Kapra, D. Y. Vodolazov, and V. R. Misko, *Vortex transport in a diamond-cell channel*, *Submitted to* Supercond. Sci. Technol. (2013).